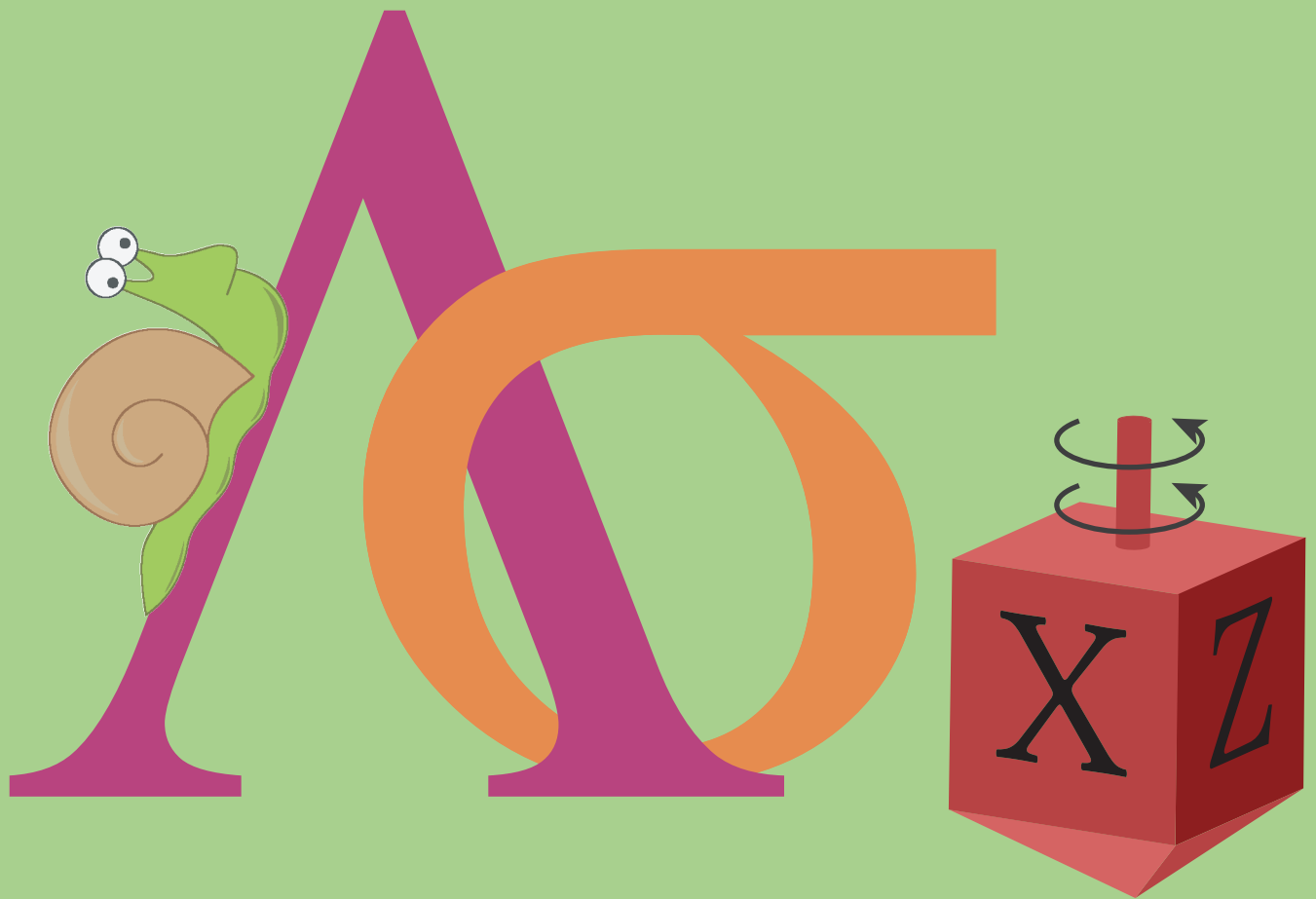


Engineering Synthetic Quantum Operations



Uri Vool

Abstract

Engineering Synthetic Quantum Operations

Uri Vool

2017

Coherent quantum effects are the hallmark of atomic systems. The field of circuit quantum electrodynamics (cQED) also allows for the control of coherent quantum systems. However, these quantum states do not correspond to atomic degrees of freedom, but to the quantized behavior of the electromagnetic field in a macroscopic superconducting circuit. These “artificial atoms” simulate many of the effects in atomic systems, with the added benefits of tunability and fast control and measurement. This thesis explores the different artificial atoms and quantum operations accessible to us using superconducting circuits, and the techniques we can use to create more interesting and complex atoms. One experiment focuses on selection rules in superconducting circuits. Using non-linear coupling, we are able to break the selection rules of a fluxonium artificial atom and drive forbidden transitions. We use this technique to construct a Λ system from the fluxonium coupled to a resonator at the fluxonium sweet spot. Another experiment focuses on the new artificial atoms and operations accessible by adding continuous external drives to the circuit. By taking the Jaynes-Cummings (JC) Hamiltonian of a qubit coupled to a cavity and adding two continuous tones, we are able to simulate an effective JC Hamiltonian in the transverse (σ_x) basis. The energies and interaction terms are completely governed by the drives, and the system can be tuned to any interaction regime *in situ*. This scheme also allows us to cool the qubit to the eigenstates of the transverse basis, and perform a continuous quantum non-demolition (QND) measurement of the transverse component of a qubit.

Engineering Synthetic Quantum Operations

A Dissertation
Presented to the Faculty of the Graduate School
of
Yale University
in Candidacy for the Degree of
Doctor of Philosophy

by
Uri Vool

Dissertation Director: Michel H. Devoret

December 2017

© 2017 by Uri Vool
All rights reserved.
Cover art by Jacob Z. Blumoff and Uri Vool

Contents

Contents	iii
List of Figures	v
List of Symbols	vii
Acknowledgments	xiii
1 Introduction and overview	1
1.1 “Natural” quantum systems	3
1.1.1 Two-level system	4
1.1.2 Λ system	5
1.1.3 Harmonic oscillator	7
1.2 Superconducting quantum systems	8
1.3 Open superconducting quantum systems	10
1.4 Thesis overview	12
2 From a circuit to an atom	14
2.1 An electromagnetic circuit	15
2.1.1 Circuit degrees of freedom	15
2.1.2 Hamiltonian of a circuit	19
2.2 Quantization	21
2.2.1 When is a circuit quantum?	21
2.2.2 Quantizing a circuit	22
2.3 Non-linear circuit elements	25
2.3.1 The Josephson junction	25
2.3.2 Combining linear and non-linear elements	27
2.4 Common artificial atoms	32
2.4.1 Cooper-pair box	32
2.4.2 Transmon	34
2.4.3 Flux qubit	34
2.4.4 Fluxonium	36

3	Circuit quantum electrodynamics	38
3.1	Photon or spin?	39
3.2	Qubit coupled to a cavity	42
3.3	Adding drives and dissipation	44
3.3.1	Input-output formalism	44
3.3.2	Stiff-pump approximation	46
3.3.3	Effective qubit drive	47
3.3.4	cavity-induced decay	48
3.3.5	Cavity-induced dephasing	50
4	Experimental methods	53
4.1	Sample preparation	54
4.1.1	Sample fabrication	54
4.1.2	Sample holder	57
4.2	Readout	60
4.2.1	Measuring the outgoing field	60
4.2.2	Measurement in transmission and reflection	61
4.2.3	Weak and strong measurement	65
5	Controlling the radiation selection rules of superconducting circuits	68
5.1	Allowed and forbidden transitions	69
5.2	SNAIL	74
5.3	SNAIL-fluxonium	79
5.3.1	Theoretical model	79
5.3.2	The device	82
5.3.3	Spectroscopy of forbidden transitions	86
5.3.4	Raman cooling	88
5.3.5	The SNAIL-fluxonium as a Λ -system	92
6	Monitoring a qubit along σ_x	96
6.1	Theoretical analysis	97
6.1.1	Resonant σ_x JC Hamiltonian	100
6.1.2	Dispersive σ_x JC Hamiltonian	100
6.2	Cooling to $ g\rangle - e\rangle$	102
6.3	Measuring σ_x	106
6.3.1	Experimental setup	106
6.3.2	Histograms vs. Rabi frequency	107
6.3.3	Measurement characterization	112
6.3.4	Quantum jumps	115
7	Conclusions and perspectives	118
7.1	Integrating the SNAIL	119
7.2	Raman-controlled qubit	121
7.3	Quantum-jump magnetometry	122
7.4	Autonomous quantum error correction	124
	Bibliography	128

List of Figures

Introduction and overview	1
1.1 Quantum system examples	3
1.2 The Bloch sphere	4
1.3 The Josephson junction	9
From a circuit to an atom	14
2.1 Definitions for electric circuits	15
2.2 Breaking an element to its linear and non-linear components	28
2.3 Foster forms of a linear circuit	29
2.4 Common superconducting artificial atoms	32
2.5 Fluxonium wave-functions for different external flux	36
Circuit quantum electrodynamics	38
3.1 Qubit coupled to a cavity	39
Experimental methods	53
4.1 SEM image of a bridge-free junction	55
4.2 Sample holders in the 3D architecture - a cavity and a waveguide	57
4.3 Readout in reflection and transmission	62
Controlling the radiation selection rules of superconducting circuits	68
5.1 Selection rules for superconducting circuits	72
5.2 SNAIL sketch and potential	75
5.3 Future uses of the SNAIL	77
5.4 Diagram of fluxonium coupled to a resonator using the SNAIL	79
5.5 SEM of the SNAIL-fluxonium device	83
5.6 spectroscopy and coherence of the SNAIL-fluxonium device	85
5.7 $ g, 0\rangle \leftrightarrow e, 1\rangle$ spectroscopy vs. flux	87
5.8 Cooling the fluxonium using Λ transitions	89
5.9 Rabi oscillations of the fluxonium qubit through the Λ -system	93

Monitoring a qubit along σ_x	96
6.1 Frequency landscape for σ_x measurement	98
6.2 Infinite Ramsey fringes while cooling to $ -\rangle$	102
6.3 Cooling to $ -\rangle$ in spectral density description	104
6.4 Schematic of the σ_x measurement experiment setup	107
6.5 Histogram of I, Q measurements while varying the Rabi frequency	108
6.6 Quantifying agreement with theory in σ_x measurement	110
6.7 I, Q Histograms of σ_x measurements of different states	113
6.8 σ_x measurements after preparation on Bloch sphere planes	114
6.9 Quantum jumps between the σ_x eigenstates	116
Conclusions and perspectives	118
7.1 Control relay implemented using SNAIL-fluxonium	126

List of symbols

Constants

h	Planck's constant
\hbar	Reduced Planck's constant ($= h/2\pi$)
k_B	Boltzmann constant
e	Electron charge
Φ_0	Magnetic flux quantum ($= h/2e$)
ϕ_0	Reduced flux quantum ($= \Phi_0/2\pi$)
R_Q	Resistance quantum ($= \hbar/(2e)^2$)

Electromagnetism

\vec{E}	Electric field
\vec{B}	Magnetic field
ϵ_0	electric permittivity of free space
μ_0	magnetic permeability of free space

Electric circuits

v_b	Voltage across branch b
Φ_b	Branch flux of branch b
i_b	Current through branch b
Q_b	Branch charge on branch b
ϕ_n	Node flux of node n
q_n	Conjugate charge of the node flux ϕ_n
Φ_{ext}^l	External flux threaded through loop l
Q_{ext}^n	Charge accumulated on node n

Z_0	Characteristic impedance of an LC oscillator ($= \sqrt{L/C}$)
ϕ_{ZPF}	Zero point fluctuations of the flux ($= \sqrt{\hbar Z_0/2}$)
q_{ZPF}	Zero point fluctuations of the charge ($= \sqrt{\hbar/2Z_0}$)
φ_{ZPF}	Zero point fluctuations of the superconducting phase ($= \phi_{\text{ZPF}}/\phi_0$)
N_{ZPF}	Zero point fluctuations of the Cooper-pair number ($= q_{\text{ZPF}}/2e$)

Superconducting circuits

φ	Superconducting phase operator across an element
N	Cooper pair number operator, conjugate to φ
Δ	Superconducting gap
E_J	Josephson tunneling energy
L_J	Josephson inductance ($= \phi_0^2/E_J$)
E_C	Capacitive energy for linear capacitance C ($= e^2/2C$)
E_L	Inductive energy for linear inductance L ($= \phi_0^2/L$)

Quantum mechanical operators and states

a, a^\dagger	Annihilation and creation operators for a harmonic oscillator
n	Photon number (energy) operator for a harmonic oscillator ($= a^\dagger a$)
σ_-, σ_+	Lowering and raising operators for a spin 1/2 system
σ_z	Pauli z operator, energy operator for spin 1/2 system ($= 2\sigma_+ \sigma_- - 1$)
σ_x	Pauli x operator, drive amplitude operator for spin 1/2 system ($= \sigma_- + \sigma_+$)
σ_x^-, σ_x^+	Lowering and raising operators in the σ_x basis ($\sigma_z = \sigma_x^- + \sigma_x^+$)
$ 0\rangle, 1\rangle, 2\rangle, \dots$	Eigenstates of a linear bosonic system (indexed by photon number)
$ g\rangle, e\rangle, f\rangle, \dots$	Eigenstates of a non-linear system
$ -\rangle, +\rangle$	Eigenstates of σ_x . $ \pm\rangle = (g\rangle \pm e\rangle)/\sqrt{2}$
$ g, 0\rangle, e, 1\rangle, \dots$	Joint eigenstates of a resonator-qubit system.

circuit QED

ω_c	Resonance frequency of the harmonic oscillator (cavity mode)
ω_q	Resonance frequency of the two-level atom (qubit)
ϵ	Cavity drive amplitude in frequency units

ω_d	Cavity drive frequency
Δ_c	The detuning of the cavity drive from the cavity resonance ($= \omega_c - \omega_d$)
Ω_R	Qubit drive amplitude in frequency units, commonly known as the Rabi frequency
ω_{qd}	qubit drive frequency
Δ_q	The detuning of the qubit drive from the qubit resonance ($= \omega_q - \omega_{qd}$)
g	Effective dipole interaction strength in frequency units
χ	Dispersive shift between the qubit and cavity

Input-output formalism

\mathbf{a}_{in}	Incoming field transmitted from the bath to the system. Has units of $1/\sqrt{s}$
\mathbf{a}_{out}	Outgoing field from the system to the bath. Has units of $1/\sqrt{s}$

Decay coefficients

κ	Energy decay rate of a harmonic oscillator
Q	Quality factor of a harmonic oscillator with frequency ω ($= \omega/\kappa$)
κ_{in}	Decay rate of a cavity into its input pin
κ_{out}	Decay rate of a cavity into its output or readout pin
κ_{sp}	Decay rate of a cavity due to spurious internal loss mechanisms
Γ_1	Energy decay rate of a qubit
T_1	Energy decay time of a qubit ($= 1/\Gamma_1$)
$\Gamma_{\uparrow}, \Gamma_{\downarrow}$	The cooling and heating rates of a qubit, respectively ($\Gamma_{\uparrow} + \Gamma_{\downarrow} = \Gamma_1$)
Γ_{φ}	Dephasing rate of a qubit
T_{φ}	Dephasing time of a qubit ($= 1/\Gamma_{\varphi}$)
Γ_2	Decoherence rate of a qubit ($= \Gamma_1/2 + \Gamma_{\varphi}$)
T_2	Decoherence time of a qubit ($= 1/\Gamma_2$)
Γ_{-}, Γ_{+}	The rates for the transitions $ +\rangle \rightarrow -\rangle$ and $ -\rangle \rightarrow +\rangle$, respectively ($\Gamma_{-} + \Gamma_{+} = \Gamma_2$)
T_{2R}	Decoherence time measured in a Ramsey experiment
T_{2e}	Decoherence time measured in an echo experiment
Γ_R	Decay rate of resonant Rabi oscillations of a qubit ($= 3\Gamma_1/4 + \Gamma_{\varphi}/2$)
T_R	Decay time of resonant Rabi oscillations of a qubit ($= 1/\Gamma_R$)

SNAIL

φ	Superconducting phase across the SNAIL small junction
$\tilde{\varphi}$	Superconducting phase across the SNAIL, centered around the potential minimum
$\Phi_{\text{ext}}^{\text{S}}$	External flux through the SNAIL loop
E_{J}	Josephson energy of the larger SNAIL junction
α	Ratio between the area (and hence Josephson energy) of the smaller and larger SNAIL junctions
n	Number of larger junction in the SNAIL
c_m	m -th order coefficient of the SNAIL
L_{S}	Linear inductance of the SNAIL

SNAIL fluxonium

φ_r	Superconducting phase across the antenna resonator capacitor
φ_q	Superconducting phase across the fluxonium small junction
L_q	Array inductance of the fluxonium
L_r	Unshared inductance of the antenna resonator
Φ_{ext}^f	External flux through the fluxonium loop
N	Number of SNAILs in the SNAIL array coupling the fluxonium and the antenna resonator
φ_{S}	Superconducting phase across the SNAIL array
$L_{\text{S}}^{\text{tot}}$	Total inductance of the coupling SNAIL array
c_m^{tot}	Total m -th order coefficient of the coupling SNAIL array
P_{th}^g	Probability to be in the fluxonium $ g\rangle$ state in thermal equilibrium
P_{red}^g	Probability to be in the fluxonium $ g\rangle$ state after red cooling tone
P_{blue}^e	Probability to be in the fluxonium $ e\rangle$ state after blue cooling tone
ω_r	Resonator resonance frequency
ω_q	Fluxonium $ g\rangle \leftrightarrow e\rangle$ resonance frequency
g_3	Third-order non-linear drive amplitude in frequency units
ϵ	Resonator drive amplitude in frequency units
ω_d	Resonator drive frequency
Δ_r	The detuning of the resonator drive from the resonator frequency ($= \omega_r - \omega_d$)

ω_{nl}	Non-linear drive frequency
Δ	Additional detuning of the non-linear drive from its transition frequency ($= \omega_d + \omega_q - \omega_{nl}$)
α_r	Coherent state amplitude in the resonator due to the non-linear drive

A qubit along σ_x

ω_{sb}	Frequency of the sideband drive on the cavity mode
ω_{qd}	Frequency of the drive on the qubit mode
ϵ_{sb}	Amplitude of the cavity sideband drive
Ω_R	Qubit drive amplitude in frequency units, commonly known as the Rabi frequency
\bar{a}	Coherent state amplitude in the cavity due to cavity sideband drive
\bar{n}_{sb}	Cavity photon number due to cavity sideband drive ($= \bar{a}^* \bar{a}$)
g_{eff}	Effective dipole interaction strength between the displaced cavity and the σ_x qubit ($= \frac{\chi \bar{a}}{2}$)
ζ	Dispersive shift between the displaced cavity and the σ_x qubit

Acronyms

AC	Alternating Current. Refers to processes at frequency $\omega > 0$
BBQ	Black Box Quantization
BCS	Bardeen-Cooper-Schrieffer
CPB	Cooper-Pair Box
CPT	Coherent Population Trapping
cQED	Circuit Quantum ElectroDynamics
DC	Direct Current. Refers to processes at frequency $\omega = 0$
DOF	Degree Of Freedom
EBPG	Electron Beam Pattern Generator
HEMT	High-Electron-Mobility Transistor
IF	Intermediate Frequency
JC	Jaynes-Cummings
JPC	Josephson Parametric Converter
JRM	Josephson Ring Modulator
OFHC	Oxygen-Free High-Conductivity

NMR	Nuclear Magnetic Resonance
NMP	N-Methyl-2-Pyrrolidone
PMMA	Poly(Methyl MethAcrylate)
QND	Quantum Non-Demolition
RF	Radio Frequency
RWA	Rotating Wave Approximation
SLUG	Superconducting Low-inductance Undulatory Galvanometer
SNAIL	Superconducting Non-linear Asymmetric Inductive eLement
SQUID	Superconducting QUantum Interference Device
SEM	Scanning Electron Microscope
STIRAP	STImulated Raman Adiabatic Passage
TE	Transverse Electric mode
TLS	Two-Level System
ZPF	Zero-Point Fluctuations

Acknowledgments

This thesis presents a personal and biased take on the field of artificial atoms and quantum electromagnetic circuits. However, the results presented here were not gathered and analyzed in isolation, but precisely the opposite. Every idea presented in this thesis is a result of countless discussions with the many teachers, colleagues, friends, and students I had the pleasure to interact with during my time at Yale. While it is impossible to give proper credit to all these influences, in this section I briefly acknowledge and thank the people who contributed to this thesis and to my work and life at Yale.

The most important influence is of course that of my adviser, Michel Devoret. Throughout my time at Yale I was fortunate to have many discussions with Michel, an experience which is difficult to describe if one has not experienced it themselves. Usually I came with a specific question, but the discussion was certainly not limited to it and often had a much wider scope. We spent much time on theoretical understanding, and Michel has repeatedly taught me that there are many layers of important subtlety and nuance in the most basic concepts of quantum mechanics and electromagnetism. At the same time, Michel paid careful attention to every small part of our experimental work, and we talked for hours about the physics of bracket thermalization or the clustering of evaporated aluminum. A careful reader will notice Michel's influence in every idea presented in this thesis. Of course, the discussions were not limited to our work, and I also learned much about black holes, heat engines, bicycles, serif fonts, the proper choice of colors, and many other topics. Michel's patience, extreme curiosity and passion for virtually any topic, and his enthusiasm and tirelessness have made my PhD a wonderful experience and strongly influenced my approach to science. I would also like to thank Michel for the opportunity of serving as the

teaching assistant for his classes on Mesoscopic physics and quantum noise. I am certain that I was, by far, the person learning the most in the class, and felt I was learning even more in my second round of teaching the classes.

I would also like to thank my thesis committee members: Steve Girvin, Leonid Glazman, and Rob Schoelkopf. They taught me much about physics and have made important contributions to the work presented here, as well as significantly improving the manuscript itself. Prior to my experimental work with Michel, I was doing theoretical work under the supervision of Steve. Much of that theoretical work is presented in this thesis. Perhaps more importantly, during that (short) time and throughout my PhD Steve taught me important and subtle concepts in quantum mechanics, quantum optics, and the physics of open quantum systems. I have used and contemplated these concepts on a daily basis during my time at Yale, and will certainly continue to do so in the future. Steve is also one of the nicest people I have ever encountered, and his relaxed and positive outlook on every challenge we faced was always encouraging and inspiring. Leonid is both a wonderful teacher of physics, and a source of seemingly endless knowledge. He provided many insightful ideas and understanding to our research, and I greatly appreciated his direct approach and extreme sensitivity to inaccurate statements. While Rob and I have not collaborated as closely, in every one of our discussions Rob raised new ideas and ways to approach the problem which I never considered, and I often regretted not approaching him sooner. I also thank my external reader, Hugues Pothier from CEA Saclay, for his critical reading of the thesis and his insightful comments.

Other Professors at Yale also helped me greatly during my PhD. On the theoretical side, Mazyar Mirrahimi and Liang Jiang were both extremely helpful and accommodating, both with the many specific and often annoying questions I had, as well as generally expanding my theoretical knowledge. I also thank Dan Prober for his kindness and support throughout my time at Yale, and for organizing all the events. Special thanks to Luigi Frunzio, who not only maintained the fabrication facility and helped me with all aspects of the fabrication process, but also greatly contributed to the lab morale with his joyful booming voice and constant beaming smile.

Throughout my time at Yale I worked closely with several post-docs, each with their unique

style and approach to science, and I have been greatly influenced by all of them. Ioan Pop started supervising me when I was not quite sure how to use an Allen wrench, and painstakingly taught me all aspects of experimental physics. I enjoyed his calm and meticulous approach to teaching and to research, and appreciated his original ideas and his preference for research topics which are off the beaten path. Angela Kou and I collaborated closely during most of my PhD, and throughout this time she was incredibly good at every task we encountered, and made them all look easy. I was also motivated by her dissatisfaction with imperfect scientific results, which perfectly countered my own approach. Angela also shared my interest in a wide range of scientific topics, and we had as many discussions about abstract and loosely-related ideas as we had about our own research, which significantly broadened my horizons and improved my understanding of physics. Shyam Shankar is an expert on virtually every aspect of research in superconducting circuits, and is involved in a variety of projects within our lab. Shyam and I collaborated closely on the transverse (σ_x) qubit project, but he also contributed to every other project I worked on, and taught me much about the field in our more general discussions. With all his knowledge and great responsibilities in lab, Shyam mostly inspired me with the patient and humble manner in which he approached every task and discussion. I would also like to thank Zaki Leghtas, who was my collaborator when we were both still theorists, and then throughout his time at Yale. As another theorist-turned-experimentalist, I felt we had an easier time understanding each other and sharing ideas, and Zaki taught me a great deal about theoretical (and at the end even experimental) physics.

Many other students and post-docs contributed significantly to the results and ideas described in the thesis, through our joint work as well as through countless discussions, and I would like to thank them all. This includes (in alphabetical order): Baleegh Abdo, Chris Axline, Jacob Blumoff, Richard Brierley, Luke Burkhart, Teresa Brecht, Gianluigi Catelani, Philippe Campagne-Ibarcq, Kevin Chou, Yiwen Chu, Claudia De Grandi, Gijs De Lange, Nick Frattini, Yvonne Gao, Alex Grimm, Michael Hatridge, Max Hays, Reinier Heeres, Eric Holland, Brian Lester, Yehan Liu, Zlatko Minev, Shantanu Mundhada, Kater Murch, Anirudh Narla, Nissim Ofek, Andrei Petrenko, Wolfgang Pfaff, Matt Reagor, Phil Reinhold, Serge Rosenblum, Kyle Serniak, Matti Silveri, Volodymir Sivak, Katrina Sliwa, Clarke Smith, Steven Touzard, Chen Wang, Zhixin Wang, Evan Zalys-Geller, and

Dong Zhou.

I also wanted to thank the people who made my life in New Haven great outside of the lab, but virtually all of them have already been mentioned above. Special second mention to Jacob and Teresa for our many adventures over the years, to my awesome roommate Anirudh, to Angela, Wolfie, Alex, Yiwen, and Luke for all the awesome climbing and other fun events, and to everyone else for contributing to a truly wonderful 6 years.

Finally, I would like to thank my mother, Ana, and my wife, Lizzie, for their overwhelming support throughout the years. This thesis is dedicated to them.

Chapter 1

Introduction and overview

Coherent quantum effects can now be observed and controlled at the level of a single particle or the equivalent in several physical systems, as opposed to the early eras of quantum measurements during which only ensembles were studied. In most such systems, the energy states and transitions arise from the degrees of freedom of atomic systems. The internal degrees of freedom of the electrons, the nuclei, and the interactions between them give rise to a rich energy level structure. Many interesting isolated quantum state manifolds are buried in the level structure of the various atomic systems, each with its own useful properties. Notable examples are Rydberg atoms [Saffman *et al.*, 2010], trapped ions [Leibfried *et al.*, 2003] and nitrogen-vacancy centers [Jelezko *et al.*, 2004, Childress *et al.*, 2006]¹. These have led to great advances in the fields of quantum sensing [Maze *et al.*, 2008], quantum communication [Duan *et al.*, 2001, Pfaff *et al.*, 2014] and quantum computation [Jaksch *et al.*, 2000, Cirac and Zoller, 1995, Monroe *et al.*, 1995, Weber *et al.*, 2010].

The field of superconducting circuits [Clarke and Wilhelm, 2008, Devoret and Schoelkopf, 2013] also enables the control of coherent quantum systems. These systems, however, do not correspond to atomic degrees of freedom but rather to the behavior of macroscopic electromagnetic fields in components such as capacitors, inductors, and Josephson junctions. By changing the parameters

¹The implementation of a quantum system using electron spins in quantum dots [Loss and DiVincenzo, 1998, Nowack *et al.*, 2007, Hanson *et al.*, 2007] is also an important example. The encoded states in this implementation are electron spin states, but they can be controlled by an electrostatic potential. Thus quantum dots are not quite an example of an atomic implementation of a quantum system, but a hybrid between an atomic system and an engineered artificial atom.

of these components and the patterns in which we combine them, we are able to synthesize a variety of “artificial atoms”. In a sense, instead of studying a given system and exploring its quantum mechanical properties, the field of superconducting circuits takes a potentially interesting theoretical quantum system and builds a physical implementation of it.

The great advantage of these synthetic quantum systems is that we are able to engineer them. While the energy transitions in e.g. trapped ions are fixed by the hyperfine interaction between electrons and nuclei, the energy transitions in a superconducting circuit can be designed to match desired parameters by changing a capacitance or inductance, or even tuned *in situ* with an applied current or voltage. The coupling between different quantum systems can also be similarly engineered, allowing for strong interactions which are a requirement for performing coherent operations on a larger system.

This thesis explores the different artificial atoms and quantum operations accessible to us using superconducting circuits, and the techniques we can use to create more interesting and complex atoms. We discuss several important quantum systems, and how their properties can be implemented as a circuit. Especially, we discuss the notion of selection rules in our artificial atom, which govern when certain transitions are allowed or forbidden, and how we can manipulate these rules to create more interesting atoms.

Another central notion of the thesis is that of driven quantum systems. By applying an external drive on our circuit, we are able to create another effective artificial atom with distinct features. This second level of synthesis can dramatically increase the variety of artificial atoms we make. This is a field of interest in small coherent quantum systems [Mollow, 1969, Xu *et al.*, 2007, Baur *et al.*, 2009, London *et al.*, 2013, Laucht *et al.*, 2017], and recently also for many-body quantum systems [Kitagawa *et al.*, 2010, Lindner *et al.*, 2011]. Here we show a proof-of-concept example of a driven two-level atom coupled to a harmonic oscillator. Already in this well-studied system, the addition of drives gives rise to novel quantum operations as we vary drive parameters. The combination of different drive parameters and the ability to physically engineer circuit parameters gives us many knobs to turn, allowing us to implement an increasing variety of quantum systems and quantum operations.

1.1 “Natural” quantum systems

A coherent quantum system, which is isolated from its environment, is often described by its Hamiltonian H . Knowing H and the initial state of the system should in principal allow us to determine the state of the system at any give time, following Schrödinger’s equation. The eigenstates of the Hamiltonian, the time-independent states of the system, are a very useful to describe the dynamics of the system. Fig. 1.1a shows an example of a generic quantum system (or atom), with its lowest eigenstates: $|g\rangle$, $|e\rangle$, $|f\rangle$, and $|h\rangle$.

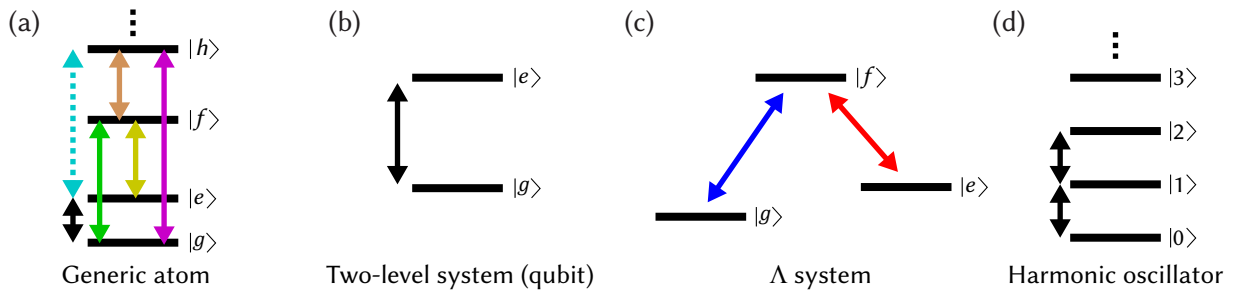


Figure 1.1: (a) A generic atom can be described in terms of its energy eigenstates. Here the lowest eigenstates $|g\rangle$, $|e\rangle$, $|f\rangle$, and $|h\rangle$ are shown. Transitions between the eigenstates are shown as straight arrows with the color corresponding to the frequency or energy difference between the states. The dashed arrow corresponds to a transition forbidden by a selection rule. (b) A two-level system consists of two eigenstates: the ground state $|g\rangle$ and the excited state $|e\rangle$. The system can be manipulated by applying a drive at the frequency corresponding to the difference between the energy levels. (c) A Λ system is a three-level system in which the lowest two states $|g\rangle$ and $|e\rangle$ are usually similar in energy in contrast to the higher third state $|f\rangle$. The direct transition between $|g\rangle$ and $|e\rangle$ is forbidden and all transitions are made through the $|f\rangle$ state. (d) A harmonic oscillator is a linear quantum system. The transition energy between nearest eigenstates is the same for all levels, and corresponds to the resonance frequency of the oscillator. Transitions are only allowed between neighboring states.

The energy transitions between the eigenstates are shown via colored arrows. By applying an external perturbation to the Hamiltonian, we are able to drive transitions between eigenstates of the system. The most common perturbation, and the only one treated in this thesis, is an electromagnetic field interacting with the atom. This is a vast domain with rich physics (see Allen and Eberly [1975] for a detailed review), but the most basic effect is that if two eigenstates have an energy difference E , a photon of the same energy can cause an excitation between them. Thus,

using an electromagnetic field oscillating at frequency E/\hbar , we can induce excitations between the corresponding eigenstates.

The dashed line corresponds to a forbidden transition, in which the electromagnetic field cannot couple the two energy levels regardless of the power applied. The rules governing which transitions are forbidden, commonly known as selection rules, are often related to a symmetry of the quantum system. For example, if the energy eigenstates of an atom are also eigenstates of spin, transitions between states of opposite spin are forbidden.

1.1.1 Two-level system

The most basic atom is a two-level system (see. Fig. 1.1b), which only has two levels $|g\rangle$ and $|e\rangle$ separated by the energy $\hbar\omega_{ge}$. In the context of quantum information, a two-level system is commonly known as a quantum bit, or qubit. It is analogous to the classical bit of information, but, due to its quantum nature, it can be in an arbitrary superposition $\alpha|g\rangle + \beta|e\rangle$ where α and β are complex numbers such that $\alpha^2 + \beta^2 = 1$.

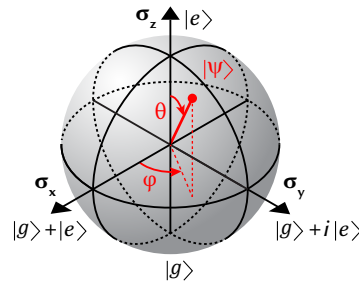


Figure 1.2: The Bloch sphere is a representation of a two-level system in the Pauli operator basis. Every pure state $|\psi\rangle$ is represented as a point on the surface of the sphere. The energy eigenstates $|g\rangle$ and $|e\rangle$ are at the two poles and their equal superpositions are on the equator. The state can be represented as a superposition of $|g\rangle$ and $|e\rangle$ using spherical coordinates: $|\psi\rangle = \cos\frac{\theta}{2}|g\rangle + e^{i\varphi}\sin\frac{\theta}{2}|e\rangle$. Mixed states, in which we do not have full information on the state of the system, are represented as points inside the Bloch sphere.

The states of a two-level system and quantum operations performed on it are best described using the formalism of Pauli operators. The space which spans all states of a two-level system in the Pauli operator basis is known as the Bloch sphere (see Fig. 1.2). While originally used to describe the behavior of spins under a magnetic field in nuclear magnetic resonance (NMR)[Slichter, 1990],

it is very useful for all two-level systems regardless of their implementation. The three axes of the sphere correspond to the expectation values of the three Pauli operators: $a_x = \langle \sigma_x \rangle$, σ_y , and σ_z . The density matrix which describes a two-level system can be directly inferred from these values:

$$\rho = \frac{\mathbf{1} + a_x \sigma_x + a_y \sigma_y + a_z \sigma_z}{2}. \quad (1.1)$$

The points on the surface of the Bloch sphere correspond to pure states, where the system is not entangled with its environment and can be fully described independently. Any such state $|\psi\rangle$ can be represented by two angles θ and φ (see Fig. 1.2) by the relation:

$$|\psi\rangle = \cos \frac{\theta}{2} |g\rangle + e^{i\varphi} \sin \frac{\theta}{2} |e\rangle. \quad (1.2)$$

Mixed states correspond to points within the Bloch sphere. In these states, the probabilities to be in any two orthogonal states still sum to one ($\text{Tr} \rho = 1$), but the information on their relative phase is incomplete as the system is not isolated ($\text{Tr} \rho^2 < 1$).

The factor $\frac{1}{2}$ in the angle representing the state in Eq. 1.2 shows us that the Bloch sphere is a skewed representation of the Hilbert space. The orthogonal states $|g\rangle$ and $|e\rangle$ are actually anti-parallel on the sphere.

Note that in Fig. 1.2 we associate the state $|e\rangle$ with the point $a_z = 1$ on the Bloch sphere. This is a convention we use throughout the thesis, and within it the Hamiltonian can be written as $\mathbf{H} = \frac{\omega_{ge}}{2} \sigma_z$. Here we see the usefulness of the Bloch sphere representation, as the Pauli operators generate rotations on it. Our Hamiltonian leads to the unitary evolution $\mathbf{U} = e^{-i\mathbf{H}t/\hbar}$ which is simply a rotation around the σ_z axis on the Bloch sphere. This is the accumulation of phase between eigenstates of different energies. Similarly, a Rabi drive $\frac{\Omega_R}{2} \sigma_x$ corresponds to a rotation around the σ_x axis, in which the state oscillates between $|g\rangle$ and $|e\rangle$ as a function of time.

1.1.2 Λ system

A Λ system (see Fig. 1.1c) is a three-level system made up of the states $|g\rangle$, $|e\rangle$, and $|f\rangle$. The lowest two energy levels $|g\rangle$ and $|e\rangle$ are usually similar in energy, while the third level $|f\rangle$ is of

substantially higher energy. The direct $|g\rangle \leftrightarrow |e\rangle$ transition is either very weak or forbidden by a selection rule, and the transitions $|g\rangle \leftrightarrow |f\rangle$ and $|e\rangle \leftrightarrow |f\rangle$ are allowed.

The two lowest states are assumed to be “metastable” - isolated from the environment and thus long-lived, while the higher level is easily accessible and thus lossy. This level structure allows for many interesting effects that are not possible in a two-level system.

An example of such an operation is the spontaneous Raman transition, where a drive on the $|g\rangle \leftrightarrow |f\rangle$ transition with the decay of the $|f\rangle$ state prepares the system in the state $|e\rangle$. This can be very useful for preparation of a system in a given state. Stimulated Raman transition is another effect, where both transitions driven simultaneously lead to an operation between the $|g\rangle$ and $|e\rangle$ states. To avoid populating the lossy intermediate $|f\rangle$ state, the transitions are driven off-resonance - at an incorrect frequency. However, the detunings of both drives from their corresponding resonant frequencies are taken to be equal, and thus a second order process, which is a coherent process involving only $|g\rangle$ and $|e\rangle$, becomes the dominant effect [Steck, 2007].

For manipulation of quantum information, such effects are very useful as they allow the qubit spanned by $|g\rangle$ and $|e\rangle$ to be long-lived and isolated, while still enabling fast state preparation, coherent operations, and measurement by using the $|f\rangle$ state. These systems are commonly used in atomic system implementation of qubits. For example, in trapped ions, state preparation and coherent oscillations between the two qubit states are performed through a higher excited state [Wineland *et al.*, 1998].

Other interesting effects rely on the existence of a “dark state” in the system. Since we are able to drive transitions between both $|g\rangle$ and $|e\rangle$ to the $|f\rangle$ state simultaneously, for a particular superposition of $|g\rangle$ and $|e\rangle$ these transitions cancel out and the system stays in its state despite the drives. This effect can be used for coherent population trapping (CPT) [Arimondo and Orriols, 1976, Gray *et al.*, 1978], where the drives, together with the decay of the $|f\rangle$ state, are used to stabilize the “dark state” of the system, which can be an arbitrary superposition of $|g\rangle$ and $|e\rangle$ by changing the amplitude and phase of the drives.

A very similar trick can be used to coherently transfer population from $|g\rangle$ to $|e\rangle$. This process is known as stimulated Raman adiabatic passage (STIRAP) [Bergmann *et al.*, 1998, Vitanov *et al.*,

2017]. By changing the drive parameters, we change the dark state of the system from $|g\rangle$ to $|e\rangle$. If the initial state of the system is $|g\rangle$ and the process is done adiabatically, the state of the system follows the imposed dark state and thus the final state of the system is $|e\rangle$. Remarkably, this process can be performed with high coherence even if the $|f\rangle$ state is very lossy, as the system is never in that state - only in its dark state.

1.1.3 Harmonic oscillator

The quantum harmonic oscillator is a basic quantum system which is at the heart of many physical effects. Most notably, it describes the quantum behavior of electromagnetic fields and mechanical vibrations. As the analog of the classical harmonic oscillator, we can write the Hamiltonian for the system as:

$$\mathbf{H} = \frac{\mathbf{p}^2}{2m} + \frac{m\omega_0^2 \mathbf{x}^2}{2}, \quad (1.3)$$

where \mathbf{x} and \mathbf{p} are the position and momentum operators of the oscillator with the commutation relation $[\mathbf{x}, \mathbf{p}] = i\hbar$. m is the mass of the oscillator and ω_0 is its characteristic frequency. For mechanical vibrations, the actual position and momentum of the motion can be treated, and for electromagnetic fields the electric and magnetic field can play the role of position and momentum (see Chapter 2 for more details).

The well-known solution to this Hamiltonian relies on the definition of the annihilation operator $\mathbf{a} = \sqrt{\frac{m\omega_0}{2\hbar}} \left(\mathbf{x} + \frac{i}{m\omega_0} \mathbf{p} \right)$. Thus the Hamiltonian can simply be written as:

$$\mathbf{H} = \hbar\omega_0 \left(\mathbf{a}^\dagger \mathbf{a} + 1/2 \right), \quad (1.4)$$

with the commutation relation $[\mathbf{a}, \mathbf{a}^\dagger] = 1$. The eigenstates of this Hamiltonian are eigenstates of the number operator $\mathbf{n} = \mathbf{a}^\dagger \mathbf{a}$ and can be labeled $|n\rangle$, $n \in \mathcal{N}$. The transition energy between any neighboring states is identical and given by $\hbar\omega_0$. The number n , which corresponds to the excitation number, is known as the number of photons in an electromagnetic oscillator, or the number of phonons in a mechanical oscillator.

The operator \mathbf{a} is called the annihilation operator as it annihilates one photon from the state

of the system: $\mathbf{a}|n\rangle = \sqrt{n}|n-1\rangle$. Its conjugate operator, \mathbf{a}^\dagger , is the creation operator as it creates a photon in the system. From our definition $\mathbf{x} = \sqrt{\frac{\hbar}{2m\omega_0}} (\mathbf{a} + \mathbf{a}^\dagger)$. Thus, a linear drive which interacts with the oscillator, for example an electric field interacting with a dipole, leads to a Hamiltonian term of the form $\epsilon (\mathbf{a} + \mathbf{a}^\dagger)$ (up to a phase), where ϵ is the drive amplitude (see Chapter 3 for more details).

Transitions in the harmonic oscillator are thus only allowed between nearest-neighbor states, as they are the only states coupled by the $\mathbf{a} + \mathbf{a}^\dagger$ interaction. All other transitions are forbidden. The symmetry corresponding to this selection rule is that the harmonic oscillator energy eigenstates are also eigenstates of the photon number operator.

As its equations of motions are linear, the harmonic oscillator is often called a linear oscillator. In fact, it is 'the' linear system - any system with linear equations of motion is equivalent to a harmonic oscillator. The addition of non-linear terms changes the eigenstates and energies of the system and leads to a more complicated structure, in which the states are not equally spaced in energy. For a weakly non-linear system, the operators of the harmonic oscillator still serve as a very convenient basis.

The two-level system can be thought of as the dual of the harmonic oscillator - a system so non-linear that we can neglect all higher excited states. The joined atom of a two-level system linearly coupled to a harmonic oscillator with a similar frequency is known as the Jaynes-Cummings (JC) Hamiltonian [Jaynes and Cummings, 1963, Haroche and Raimond, 2006], and is central to many atomic implementations of coherent quantum systems, as well as superconducting artificial atoms.

1.2 Superconducting quantum systems

Superconducting circuits are made up of electromagnetic circuit elements, such as inductors and capacitors. Thus, the most natural quantum system for such circuits is the harmonic oscillator. This system can be implemented as a patterned superconducting planar circuit or as the stationary wave mode of a cavity. With sufficiently high coherence ($\omega \gg \kappa$ where ω is the cavity frequency and κ is its decay rate) and low temperature ($\hbar\omega \gg k_B T$), this system shows quantum effects and

behaves as a quantum harmonic oscillator.

While the harmonic oscillator is an interesting quantum system, it can only implement a limited range of effects and does not allow full quantum control [Weedbrook *et al.*, 2012]. Adding non-linearity to the system significantly increases the range of operations we can perform, and potentially allows us to create an arbitrary unitary evolution of the quantum system.

The Josephson junction is the main source of non-linearity used for superconducting artificial atoms. It consists of two superconductors sandwiched by a thin oxide layer (see Fig. 1.3a). This element allows for the tunneling of Cooper pairs across it. As the tunneling is discrete in units of charge, the conjugate flux across the junction must be periodic. This periodic form makes the Josephson junction behave as a non-linear inductor (see Chapter 2 for more details).

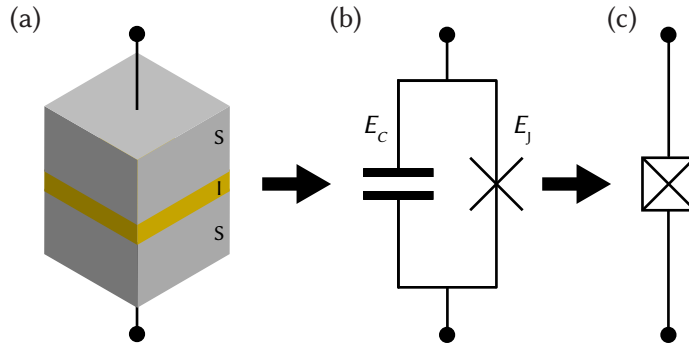


Figure 1.3: (a) A Josephson junction consists of two superconductors (S) sandwiching a thin insulating layer (I). (b) The Josephson junction is described in circuit form as a capacitor with capacitive energy E_C in parallel with the tunneling element (shaped like an x) with Josephson energy E_J . The tunneling of Cooper pairs across the junction can be understood as a non-linear inductance. This element is the source of non-linearity used in all superconducting quantum circuits. (c) The sketch of the combined capacitor and tunneling element.

The Josephson tunneling can be expressed in the form $-E_J \cos \varphi$ where E_J is the tunneling energy and φ is the superconducting phase across the junction. Thus the Josephson element can be expressed as a non-linear inductor by expanding the \cos term:

$$-E_J \cos \varphi = \frac{E_J}{2} \varphi^2 - \frac{E_J}{24} \varphi^4 + \dots, \quad (1.5)$$

where the first term is the linear part and the following terms contribute to the non-linearity. The

Josephson tunneling element always appears in parallel with a capacitive term (see Fig. 1.3b). This capacitance C is often described in terms of its capacitive energy for a single electron $E_C = e^2/2C$. Thus the capacitor and non-linear inductor of the Josephson junction already correspond to a non-linear quantum oscillator.

To make different circuits, we pattern different structures of capacitors, inductors and Josephson junctions. For example, we can shunt the Josephson junction with an additional shunt capacitor $C_s \gg C$, and thus reduce its capacitive energy. This circuit, known as the transmon [Koch *et al.*, 2007], is a weakly non-linear oscillator which is currently the most common implementation of a superconducting qubit. A more detailed description, as well as a variety of superconducting circuits, are presented in Chapter 2.

The two lowest energy levels of the circuit are commonly taken to be the qubit states. Due to the non-linearity, the energy difference between levels is not equal and thus this transition can be addressed individually. Note that this transition energy, and the coupling between multiple such qubits, are completely given by the parameters of the circuit. This ability to engineer our atoms to the desired behavior is a significant advantage of superconducting artificial atoms.

Our ability to engineer circuits, however, is not absolute. As our toolbox of circuit elements is limited, we are bounded to particular atom structures. In Chapter 5 we discuss the limitation of selection rules in our atoms, and introduce a new circuit element which can lift this limitation. The addition of tools into our toolbox is necessary to expand the abilities of superconducting circuits, and may eventually allow us to simulate an arbitrary Hamiltonian.

1.3 Open superconducting quantum systems

So far we have discussed the degrees of freedom of an isolated circuit, in which we can combine different circuit elements to produce a variety of Hamiltonians. Our system, however, is never completely isolated. There is always some parasitic coupling to the external environment, and decreasing the sensitivity of our system to different loss mechanisms is a central effort in the field of superconducting qubits.

But even the ideal circuit is not isolated. To perform our operations and measurements, we need to interact strongly with the circuit. And so, there is a delicate balance in which the system should be completely isolated from the environment, but also strongly coupled to our controlled environment when we interact with it. Designing systems which are closer and closer to this perfect balance is perhaps the main focus of the field of experimental quantum information.

Our controlled interaction with the system can be separated into two parts: the drive, in which we apply an oscillating electromagnetic field to the system, and the dissipation, in which we extract energy and information out of the system². Commonly, the drive is used to perform gates by sending pulsed tones at the system, and the dissipation is used to measure the system. However, the combination of the two can be used in a variety of ways to implement novel quantum operations, and create effective artificial atoms. A combination of continuous drives with a controlled dissipation were used to autonomously prepare artificial atoms in a desired state [Geerlings *et al.*, 2013, Murch *et al.*, 2012, Shankar *et al.*, 2013, Leghtas *et al.*, 2013] and even stabilize a degenerate manifold of states [Leghtas *et al.*, 2015] - which allows us to encode artificial atoms in the states of a cavity [Mirrahimi *et al.*, 2014].

These schemes are based on constant “pump” drives, tuned to specific frequencies which, when combined with the non-linearity of the Josephson junction, can make high-order effects resonant and therefore significant. However, drives that do not correspond to specific transitions can not be neglected, and can actually lead to significant effects as well. In Chapter 6 we discuss a proof-of-concept example, in which, by applying two drive tones, we obtain an effective artificial atom with parameters determined by the drive amplitudes and frequencies. With the drives on a resonant transition, this protocol leads to the cooling of the qubit to a transverse eigenstate, but off-resonance this protocol can be used to continuously measure the state of the qubit in the transverse basis - the first such measurement in any implementation of a quantum system [Vool *et al.*, 2016].

The observation of such significant effects by only applying two drive tones to the JC Hamil-

²These two are actually fundamentally related by the fluctuation-dissipation theorem [Callen and Welton, 1951, Steck, 2007, Vool and Devoret, 2017], as the fluctuations of the drive (even the vacuum drive when none is applied) lead to an inherent dissipation and vice versa.

tonian, perhaps the most well-studied system in our field, hints at the potential in open superconducting systems. The space of quantum operations available to us with the ability to tune drive parameters, dissipation and the non-linearity of the circuit itself seems vast, and we have only begun studying its possibilities.

1.4 Thesis overview

This thesis discusses the encoding of artificial atoms in superconducting system, and explores the possibility to synthesize a larger variety of superconducting artificial atoms and quantum operations.

Building on the introduction in Chapter 1, Chapter 2 gives the theoretical framework for writing the Hamiltonian of an electric circuit and quantizing it. It also discusses the effects of adding non-linear elements to the circuit, and how to combine linear and non-linear circuit elements within this framework. It ends with a brief description of the common superconducting artificial atoms.

Chapter 3 describes the framework of circuit quantum electrodynamics (cQED). It begins with a discussion of using the harmonic oscillator basis vs. the spin $1/2$ basis to describe a general non-linear system, and how both should be seen as imperfect treatments with their advantages and disadvantages. Then we discuss the physics of the JC Hamiltonian for a two-level atom coupled to a harmonic oscillator. This allows us to describe the control and measurement of our system within the framework of cQED [Blais *et al.*, 2004], and also serve as an important theoretical basis for the experiment described in Chapter 6. We briefly discuss the master equation treatment of drives and dissipation in this context, and particularly describe the physics of measurement-induced dephasing, in which photons in the harmonic oscillator lead to loss of coherence in the qubit.

Chapter 4 reviews some experimental techniques for the experiments described in the thesis. We begin by discussing the fabrication of our Josephson junctions, as well as the sample holders used to house them. We also review the dispersive readout technique, the common readout technique in superconducting circuits which was used in all experiments in this thesis, with a discussion

on readout in transmission vs. reflection.

Chapter 5 discusses the experimental work to break selection rules in the fluxonium. We begin with a review of selection rules in superconducting circuits. Then we discuss the novel three-wave-mixing device nicknamed the Josephson Non-linear Asymmetric Inductive eLement (SNAIL), and its potential use for non-linear coupling and amplification [Frattoni *et al.*, 2017]. Finally, we describe how to integrate the SNAIL into the fluxonium qubit, and show that we are able to drive forbidden transitions in the new SNAIL-fluxonium system. We use this ability to construct an effective Λ -system from the fluxonium artificial atom.

Chapter 6 discusses the experimental work to continuously measure the qubit in the transverse (σ_x) basis. We begin with a theoretical treatment of the dispersive JC Hamiltonian with two additional drives, and the transformation to an effective frame in which this Hamiltonian becomes the undriven Rabi Hamiltonian between a qubit in the σ_x basis and a displaced harmonic oscillator. We discuss the resonant and dispersive limits of this model, and show how they can lead to transverse cooling and measurement respectively. The next section discusses the experiment to cool a qubit to the eigenstates of σ_x using this framework. The last section presents the implementation of a continuous, quantum non demolition (QND), measurement of σ_x , and an observation of quantum jumps in the transverse basis.

The final chapter concludes the thesis with final thoughts and offers perspectives on the ideas presented.

This thesis does not discuss all the projects studied during my PhD. The main project not discussed is the measurement of quasiparticle dynamics in superconducting circuits using the fluxonium artificial atom, and it can be viewed in Ref. Vool *et al.* [2014].

Chapter 2

From a circuit to an atom

Superconducting circuits are commonly described as a network of elements such as capacitors, inductors and Josephson junctions. However, they represent coherent quantum systems which should be treated using the formalism of atomic physics and quantum optics [Devoret, 1997, Blais *et al.*, 2004, You and Nori, 2011]. The character of the effective artificial atom encoded within the circuit is often not apparent, and requires rigorous treatment to decode. The situation is simpler for linear systems, as we can reduce the analysis to determining the resonance frequencies and characteristic impedances of the effective modes of the system. For strongly non-linear systems, however, the system cannot be easily decoupled and the dependence of the eigenstates on the value of a particular circuit element can be quite complex.

This chapter provides a brief description of the physics of quantum electromagnetic circuits, and a tutorial on deriving atom parameters from circuit parameters. We begin with the treatment of linear circuits, and show how an arbitrary linear circuit can be expressed as a collection of quantum harmonic oscillators. We then study the Josephson junction - the source of non-linearity in our circuits. We integrate the Josephson junction into our circuit and discuss how to treat non-linear circuits in the harmonic oscillator basis and how to combine linear and non-linear elements. We conclude by presenting several common superconducting artificial atoms.

2.1 An electromagnetic circuit

In this section, we describe how to find the degrees of freedom (DOF) of a circuit and write its Hamiltonian. This section follows the recent review paper in Ref. Vool and Devoret [2017], which is itself based on the Les Houches Summer School lecture notes given in Ref. Devoret [1997]. The review contains a more detailed discussion, with an emphasis on the treatment of open quantum circuits.

2.1.1 Circuit degrees of freedom

An electric circuit is a representation of the electric and magnetic field as a network of discrete elements connected by nodes. Each such element is considered as a “branch” of the circuit (see Fig. 2.1a).

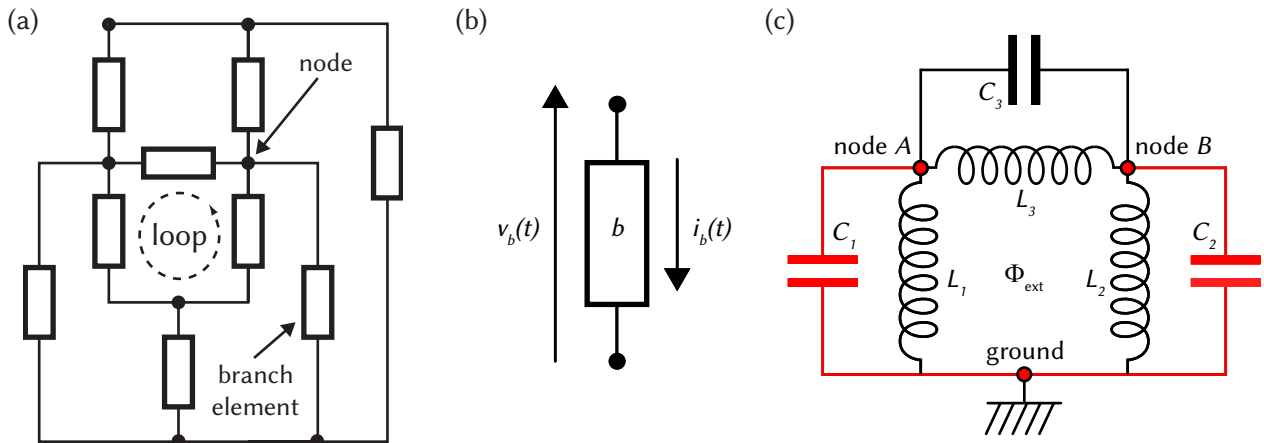


Figure 2.1: (a) A sketch of a general circuit which shows dipole element branches connected by nodes and forming loops. (b) Sign convention for the voltage and current associated with an arbitrary branch b of an electrical circuit. (c) Example circuit with a spanning tree selection. The spanning tree goes from the ground node to nodes a and b following the red path.

The element of each branch b at time t is characterized by two variables: the voltage $v_b(t)$ across the element and the current $i_b(t)$ flowing through it (see Fig. 2.1b). For each branch b we choose an orientation, which determines the sign of the voltage and current values.

The voltage and the current are defined from the underlying electromagnetic fields by

$$v_b(t) = \int_{\text{beginning of } b}^{\text{end of } b} \vec{E}(\vec{r}, t) \cdot d\vec{\ell} \quad (2.1)$$

$$i_b(t) = \frac{1}{\mu_0} \oint_{\text{around } b} \vec{B}(\vec{r}, t) \cdot d\vec{s} \quad (2.2)$$

In Eq. 2.2 the magnetic field is integrated along a closed loop in vacuum encircling the element. Note that the voltage and current orientations were chosen to be opposite. This is an intentional choice so that the energy absorbed by the element can be conveniently defined as $\mathcal{E}_b(t) = \int_{-\infty}^t v_b(t') i_b(t') dt'$.

We consider our elements to be lumped, and thus the voltage and current should not depend on the path taken during the integration. To insure this, we assume the paths are well outside the wire of inductors for the line integral of electric field (so that the magnetic field is zero along the path) and well outside the dielectric of capacitors for the loop integral of magnetic field (so the electric field is zero along the loop).

We can now integrate the current and voltage in time to obtain the flux and charge of each branch:

$$\Phi_b(t) = \int_{-\infty}^t v_b(t') dt' \quad (2.3)$$

$$Q_b(t) = \int_{-\infty}^t i_b(t') dt' \quad (2.4)$$

These quantities allow us to write the Kirchoff relations while accounting for external flux and charge biases, which are necessary for the Hamiltonian formulation of a circuit:

$$\sum_{\text{all } b \text{ around } l} \Phi_b = \Phi_{\text{ext}}^l \quad (2.5)$$

$$\sum_{\text{all } b \text{ arriving at } n} Q_b = Q_{\text{ext}}^n \quad (2.6)$$

where l is a loop of branches with external flux Φ_{ext}^l threaded through it, and n is a node which

connects several branches with a charge Q_{ext}^n on it. From these relations we see that not every branch flux, for example, is an independent DOF of the circuit.

Before proceeding to find the independent DOF and write its corresponding Hamiltonian, let us simplify the discussion by defining two specific types of elements which are used in virtually any treatment of electric circuits:

A dispersive element b for which the voltage $v_b(t)$ is only a function of the charge $Q_b(t)$ and not directly of the time t or any other variable, is said to be a capacitive element.

$$v_b(t) = f(Q_b(t)) \quad (2.7)$$

Its capacitance, which is only a function of the charge, is given by:

$$C(Q_b) = \left[\frac{df}{dQ_b} \right]^{-1} \quad (2.8)$$

A linear capacitance is independent of Q_b ($C(Q_b) = C$), and so we can simplify the relation to be $v_b(t) = (Q_b(t))/C$. Its energy is then given by $\mathcal{E}_b(t) = \frac{1}{2C}(Q_b(t))^2$. As $\dot{\Phi}_b = v_b$ we can also write $\mathcal{E}_b(t) = \frac{C}{2}(\dot{\Phi}_b(t))^2$

Similarly, a dispersive element b for which the current $i_b(t)$ is only a function of the flux $\Phi_b(t)$ and not directly of the time t or any other variable, is said to be an inductive element.

$$i_b(t) = g(\Phi_b(t)) \quad (2.9)$$

Its inductance, which is only a function of the flux, is given by:

$$L(\Phi_b) = \left[\frac{dg}{d\Phi_b} \right]^{-1} \quad (2.10)$$

A linear inductance is independent of Φ_b ($L(\Phi_b) = L$), and so $i_b(t) = (\Phi_b(t))/L$. Its energy is then given by $\mathcal{E}_b(t) = \frac{1}{2L}(\Phi_b(t))^2$.

In this section, we limit ourselves to linear circuits, made of a combination of linear inductances

and capacitances. The integration of non-linear elements into the circuit is treated in Section 2.3.

To find independent DOF for our circuit, we would like to incorporate the Kirchhoff relations into our variable definition. There are two methods which can be used for this, and they correspond to choosing flux or charge as the “position” variable of our circuit. Here, we follow the method of nodes, in which we assign a flux to every node in the circuit. The other method, the method of loops, assigns a charge to every loop in the circuit. While these methods are equivalent at this point, the Josephson non-linearity introduced in the following chapters is inductive, making the method of nodes a natural choice.

This initial step in the method of nodes is to define a ground node. This is the node of zero flux from which we define all others. Now we can construct a spanning tree (see Fig. 2.1c) which goes from the ground node to every other node, following a particular path. The flux ϕ_n associated with node n is given by the sum of branch fluxes for all the branches in the path P_n connecting the ground node to node n : $\phi_n = \sum_{b \in P_n} \Phi_b$. Thus all branch fluxes are related to the node fluxes by:

$$\Phi_{b \in T} = \phi_n - \phi_{n'} \quad (2.11)$$

$$\Phi_{b \in \bar{T}} = \phi_n - \phi_{n'} + \Phi_{\text{ext}}^l \quad (2.12)$$

where T is the set of branches which are part of the spanning tree, and \bar{T} is the complement of that set. If a branch is not part of the spanning tree, it necessarily forms a loop l with spanning tree branches, and Φ_{ext}^l is the flux threaded through that loop.

We can now express the energy of each element in the circuit as a function of the node fluxes ϕ_n . All inductive element energies can be summed to the potential energy $\mathcal{E}_{\text{pot}}(\phi_1, \phi_2, \dots)$, and all capacitive energies can be summed to the kinetic energy $\mathcal{E}_{\text{kin}}(\dot{\phi}_1, \dot{\phi}_2, \dots)$.

Note that there are different choices for spanning trees which result in different expressions for the energy, but eventually lead to the same equations of motion. However, some choices are better than others as they simplify the solution of these equations. As a general rule, it is a good idea to define the tree through capacitive elements as the conjugate variable (defined in following

section) then easily relates to the charge across the capacitor.

2.1.2 Hamiltonian of a circuit

We can now obtain the Lagrangian by subtracting the potential energy from the kinetic energy:

$$\mathcal{L} = \mathcal{E}_{\text{kin}} - \mathcal{E}_{\text{pot}} \quad (2.13)$$

The corresponding Lagrangian for the circuit of Fig. 2.1c is:

$$\begin{aligned} \mathcal{L}(\phi_A, \dot{\phi}_A, \phi_B, \dot{\phi}_B) &= \frac{C_1 \dot{\phi}_A^2}{2} + \frac{C_2 \dot{\phi}_B^2}{2} + \frac{C_3 (\dot{\phi}_A - \dot{\phi}_B)^2}{2} \\ &\quad - \left[\frac{\phi_A^2}{2L_1} + \frac{\phi_B^2}{2L_2} + \frac{(\phi_A - \phi_B + \Phi_{\text{ext}})^2}{2L_3} \right], \end{aligned} \quad (2.14)$$

where the DOF ϕ_A and ϕ_B are the fluxes of the nodes A and B .

The equations of motion for the circuit are given by the Euler-Lagrange equations:

$$\frac{d}{dt} \frac{\partial \mathcal{L}}{\partial \dot{\phi}_n} - \frac{\partial \mathcal{L}}{\partial \phi_n} = 0 \quad (2.15)$$

and we can define charge conjugate to the node flux:

$$q_n = \frac{\partial \mathcal{L}}{\partial \dot{\phi}_n} \quad (2.16)$$

Note that not every node flux necessarily corresponds to a DOF of the circuit, as the Lagrangian can depend on only ϕ_n or only $\dot{\phi}_n$. These nodes, which we call *passive* nodes, connect only inductors or only capacitors. See the review paper [Vool and Devoret, 2017] for a more detailed treatment of *active* and *passive* nodes in order to define a circuit where all variables are true DOF.

This is not strictly necessary, as the equations of motion reveal the behavior of the circuit. For a *passive* node n which connects only capacitors, the Euler-Lagrange equation simplifies to $\dot{q}_n = 0$ and so q_n is just a constant charge, the sum of the charges on the capacitors connected to the node. For an inductive *passive* node, the Euler-Lagrange equation show a dependence between

the different node fluxes, so that $\phi_n = f(\phi_1, \dots, \phi_{n-1}, \phi_{n+1}, \dots)$, and thus the DOF can be eliminated.

Our next step is to write the Hamiltonian, which requires expressing \mathcal{E}_{kin} as a function of the conjugate charges $\{q_n\}$. This requires inverting Eq. 2.16, which can be written in matrix form as the capacitance matrix $\vec{q} = [\mathbf{C}] \vec{\phi}$ relating the vector of all node flux derivatives to their corresponding node charges.

For the Fig. 2.1c, this relation can be expressed as:

$$\begin{pmatrix} q_A \\ q_B \end{pmatrix} = \begin{bmatrix} C_1 + C_3 & -C_3 \\ -C_3 & C_2 + C_3 \end{bmatrix} \begin{pmatrix} \dot{\phi}_A \\ \dot{\phi}_B \end{pmatrix} \quad (2.17)$$

After inverting the matrix and expressing the Lagrangian as a function of $\{\phi_n\}$ and $\{q_n\}$, we can obtain our Hamiltonian from the Lagrangian using the Legendre transformation:

$$\mathcal{H} = \sum_n \dot{\phi}_n q_n - \mathcal{L} \quad (2.18)$$

If \mathcal{E}_{kin} is a quadratic function of $\{q_n\}$, we can also describe the Hamiltonian in a simpler form:

$$\mathcal{H} = \mathcal{E}_{\text{kin}} + \mathcal{E}_{\text{pot}}, \quad (2.19)$$

where the Hamiltonian is equal to the total energy of the system. Note that this does not work for general circuits with non-quadratic kinetic energy.

The equations of motion are given in the form of Hamilton's equations:

$$\dot{\phi}_n = \frac{\partial \mathcal{H}}{\partial q_n} \quad (2.20)$$

$$\dot{q}_n = -\frac{\partial \mathcal{H}}{\partial \phi_n} \quad (2.21)$$

For the circuit in Fig. 2.1c, the Hamiltonian can be written as:

$$\begin{aligned} \mathcal{H}(\phi_A, q_A, \phi_B, q_B) = & \frac{1}{C_1 C_2 + C_1 C_3 + C_2 C_3} \left[\frac{(C_2 + C_3) q_A^2}{2} \right. \\ & \left. + \frac{(C_1 + C_3) q_B^2}{2} + C_3 q_A q_B \right] \\ & + \left[\frac{\phi_A^2}{2L_1} + \frac{\phi_B^2}{2L_2} + \frac{(\phi_A - \phi_B + \Phi_{\text{ext}})^2}{2L_3} \right] \end{aligned} \quad (2.22)$$

Note that the external flux Φ_{ext} in this case leads to an offset in the flux coordinates of the form $(\phi_A - \phi_B) \frac{\Phi_{\text{ext}}}{L_3}$ (which physically corresponds to a DC current). Also, the DOF are coupled to each other due to terms such as $\frac{C_3}{C_1 C_2 + C_1 C_3 + C_2 C_3} q_A q_B$ or $\frac{1}{L_3} \phi_A \phi_B$. For linear circuits, all these terms can be eliminated by a proper linear coordinate transformation: $\phi_1 = \alpha_1 \phi_A + \beta_1 \phi_B + \phi_1^{\text{offset}}$, $\phi_2 = \alpha_2 \phi_A + \beta_2 \phi_B + \phi_2^{\text{offset}}$.

In general, all linear circuits with N DOF can be brought to their diagonal form: $H = \sum_{i=1}^N \frac{\phi_i^2}{2L_i} + \frac{q_i^2}{2C_i}$. These are N independent harmonic oscillators, each with its own characteristic resonance frequency $\omega_i = 1/\sqrt{L_i C_i}$. They are sometimes called the resonant modes of the electric circuit. Understanding any linear circuit thus reduces to understanding the behavior of a linear oscillator.

Things are much more complicated for non-linear oscillators. Offset fluxes in a non-linear circuit can significantly alter its dynamics, and are thus used in many superconducting circuits (see Section 2.4). Also, non-linear circuits can not generally be decoupled. The full system, where the different DOF all affect each other, is often necessary to properly understand the behavior of each non-linear mode.

2.2 Quantization

2.2.1 When is a circuit quantum?

Nominally, every electromagnetic circuit can be treated with the formalism of quantum mechanics. However, quantum effects are not very prominent in most circuits. There are two main reasons for this suppression of quantum effects: The electro-magnetic energy stored in the circuit is large

compared to the energy quantum $\hbar\omega$ for a mode of frequency ω , masking the quantized nature of the excitations, and quantum correlations are washed out due to interactions with external DOF.

The first problem is experimentally solved by cooling the circuit down to a sub-Kelvin temperature T , for which $k_B T \ll \hbar\omega$. The mode is then in its ground state, in which quantum fluctuations become apparent.

The second problem is solved by the use of a superconductors. A detailed discussion of the broad field of superconductivity can be found in refs. Tinkham [2004], Bruus and Flensberg [2004], De Gennes [1999], and here we only briefly discuss the role of superconductivity in isolated quantum circuits.

In the BCS mean-field theory of superconductivity, the number of electrons in the ground state is not a conserved quantity, but their parity is. The electrons are created and annihilated in pairs, known as Cooper pairs, of opposite momentum and spin. This interaction leads to an energy gap Δ protecting the ground state. To allow an unpaired quasiparticle into the superconductor, it must have an energy of at least Δ . For a photon to affect the superconductor, it needs to break a Cooper pair, and thus needs to have an energy of at least 2Δ . Thus, for circuits made of superconductors, modes for which $\hbar\omega \ll 2\Delta$ can not interact with the superconductor quasiparticle DOF. These modes are thus decoupled from their environment and behave as isolated quantum systems.

Note that insulators and semiconductors are also gapped, but of course electric circuits cannot be made out of them. Their gap prevents current or charge accumulation below the gap energy. The superconductor allows charge accumulation and current - as long as these involve only pairs of electrons. The combination of the electromagnetic excitations, similar to a metal, and the gapped structure, similar to an insulator, is the unique property which allows for the creation of artificial atoms out of superconducting circuits.

2.2.2 Quantizing a circuit

The transition to quantum DOF is straightforward in the framework of the Hamiltonian description developed in the preceding section. The classical variables and the Hamiltonian are replaced by

their corresponding operators¹:

$$\begin{aligned}\phi &\rightarrow \boldsymbol{\phi} \\ q &\rightarrow \boldsymbol{q} \\ \mathcal{H} &\rightarrow \boldsymbol{H}\end{aligned}\tag{2.23}$$

The different node fluxes ϕ_n correspond to the position operators of different bosonic modes, and thus all commute. However, pairs of operators corresponding to conjugate variables do not commute. In the node variable framework, the commutator of every node flux ϕ_n and its conjugate node charge q_n is:

$$[\phi_n, q_n] = i\hbar\tag{2.24}$$

This relation stems from the quantization of the electromagnetic field and corresponds to the fundamental commutator for conjugate variables. Of course, Eq. 2.24 is valid only if the electric state of node n is a true DOF of the circuit, meaning that neither ϕ_n, q_n or their derivatives are constants of motion. More generally, this is the canonical quantization [Dirac, 1967] which relates the classical Poisson bracket and its corresponding commutator:

$$\{A, B\}_{PB} \rightarrow \frac{1}{i\hbar} [\boldsymbol{A}, \boldsymbol{B}]\tag{2.25}$$

As we have shown above, the treatment of an arbitrary quantum linear circuit reduces to the treatment of an LC oscillator. Our Hamiltonian thus corresponds to:

$$\boldsymbol{H} = \frac{\boldsymbol{q}^2}{2C} + \frac{\boldsymbol{\phi}^2}{2L},\tag{2.26}$$

and it is completely analogous to Eq. 1.3 which we reviewed in Chapter 1.

¹Throughout the thesis, we label quantum operators in bold.

We can define the creation and annihilation operators in an identical manner:

$$\phi = \phi_{\text{ZPF}} (\mathbf{a} + \mathbf{a}^\dagger) \quad (2.27)$$

$$\mathbf{q} = \frac{1}{i} q_{\text{ZPF}} (\mathbf{a} - \mathbf{a}^\dagger) \quad (2.28)$$

where ϕ_{ZPF} and q_{ZPF} are the zero-point fluctuations (ZPF) of the flux and charge operators respectively. These are the fluctuations of the flux and charge of the ground state of the harmonic oscillator. They correspond to an uncertainty in flux or charge, as the ground state is not an eigenstate of these operators.

The fluctuations are given by:

$$\begin{aligned} \phi_{\text{ZPF}} &= \sqrt{\frac{\hbar Z_0}{2}} \\ q_{\text{ZPF}} &= \sqrt{\frac{\hbar}{2Z_0}} \end{aligned} \quad (2.29)$$

where, $Z_0 = \sqrt{\frac{L}{C}}$ is the characteristic impedance of the oscillator. Thus, increasing the characteristic impedance enhances flux fluctuations and reduces charge fluctuations - which is equivalent to the Heisenberg uncertainty principle. This intuition can be useful when discussing the sensitivity of artificial atoms to specific loss mechanisms such as charge noise or flux noise.

It is sometimes convenient to define normalized conjugate operators $\mathbf{N} = \mathbf{q}/2e$ and $\varphi = \phi/\phi_0$ where e is the electron charge and ϕ_0 is the reduced magnetic flux quantum. These unitless operators obey the commutation relation $[\phi, \mathbf{N}] = i$. Correspondingly, we will define the normalized ZPF $N_{\text{ZPF}} = q_{\text{ZPF}}/2e$ and $\varphi_{\text{ZPF}} = \phi_{\text{ZPF}}/\phi_0$

While we have only shown the quantization of a linear circuit, this quantization framework is also useful for non-linear circuits. A non-linear circuit can also be expressed in the linear operator basis with no approximation. However, it is important to remember that for such a circuit the linear operators are just a convenient basis, and do not easily correspond to operations on the eigenstates of the non-linear Hamiltonian.

2.3 Non-linear circuit elements

As we have seen above, the physics of linear quantum circuits is not very rich. It can be reduced to the treatment of a single quantum harmonic oscillator, and thus it clearly cannot simulate a large variety of atoms, and is of limited usefulness as a quantum information resource [Weedbrook *et al.*, 2012]. The addition of even a small non-linearity, however, completely changes the situation and allows for universal control of the quantum state [Lloyd, 1992]. In atomic systems, the non-linearity is obtained by the properties of the atoms themselves. In the field of quantum optics [Walls and Milburn, 2008], it is obtained by the use of non-linear media.

Non-linear physics with superconducting circuits is based on the Josephson junction [Josephson, 1962]. It is the cornerstone of most superconducting artificial atoms, and the only source of non-linearity discussed in this thesis.

Until recently, it has also been the only source. However, recent advances have led to the implementation of new non-linear elements in superconducting circuits. Notable examples are nanomechanical oscillators [Chan *et al.*, 2011, Teufel *et al.*, 2011], and atomic-point contacts [Brethau *et al.*, 2013, Janvier *et al.*, 2015]. Superconducting nanowires [Krogstrup *et al.*, 2015], which have recently been used as Josephson junctions in quantum circuits Larsen *et al.* [2015], can also lead to a promising novel non-linear element.

2.3.1 The Josephson junction

The Josephson junction (see Fig. 1.3) is made up of a tunneling element in parallel with a capacitor. To write a Hamiltonian description of the junction, let us consider the superconducting electrodes of the junction, with Cooper-pair numbers N_1 and N_2 . As the system is isolated, the sum $N_1 + N_2$ is constant, but the difference $N = N_1 - N_2$ is a DOF corresponding to the number of Cooper pairs tunneling through the junction.

We should treat the difference variable as a quantum operator $\hat{N} = \sum_N N |N\rangle \langle N|$ where $|N\rangle$ is a state of the system with N Cooper pairs having passed through the junction. The charge across the capacitor is directly related to \hat{N} , which is simply charge in Cooper-pair units: $Q =$

$2eN$. Thus we can write the Hamiltonian term for the capacitor (our kinetic energy equivalent) as:

$$\mathbf{H}_C = \frac{4e^2 N^2}{2C} = 4E_C N^2 \quad (2.30)$$

where $E_C = \frac{e^2}{2C}$ is the capacitive energy for the junction capacitance C .

The Josephson tunneling term can also be expressed in this basis as:

$$\mathbf{H}_J = -\frac{E_J}{2} \sum_{N=-\infty}^{N=-\infty} (|N\rangle\langle N+1| + |N+1\rangle\langle N|), \quad (2.31)$$

where E_J is the Josephson tunneling energy.

The operator \mathbf{H}_J is clearly not diagonal in N , but it appears to be diagonal in the conjugate operator. We can define the conjugate basis:

$$|\theta\rangle = \sum_{N=-\infty}^{N=-\infty} e^{iN\theta} |N\rangle \quad (2.32)$$

$$|N\rangle = \frac{1}{2\pi} \int_0^{2\pi} d\theta e^{-iN\theta} |\theta\rangle \quad (2.33)$$

In the $|\theta\rangle$ basis, the tunneling Hamiltonian takes the form:

$$\mathbf{H}_J = -\frac{E_J}{4\pi} \int_0^{2\pi} d\theta (e^{i\theta} + e^{-i\theta}) |\theta\rangle\langle\theta|, \quad (2.34)$$

and so it is diagonal. The $e^{i\theta}$ and $e^{-i\theta}$ terms correspond to Cooper-pair tunnelings in both directions, which in this basis impart opposite phases.

We can define the operator $\cos \theta = \frac{1}{2\pi} \int_0^{2\pi} d\theta \cos \theta |\theta\rangle\langle\theta|$, and now the Josephson tunneling potential takes the familiar form:

$$\mathbf{H}_J = -E_J \cos \theta \quad (2.35)$$

As θ is conjugate to the normalized charge operator N , it would be convenient to identify it with the normalized flux operator ϕ/ϕ_0 . However, θ is periodic and defined on the unit circle, or equivalently the charge operator N is discrete in units of Cooper pairs. Thus, these operators

appear significantly different and not reconcilable with their harmonic oscillator counterparts.

This periodic symmetry is easily lifted by introducing a large inductor shunting the junction. We can then define the reduced flux across the junction and inductor to be $\varphi = \phi/\phi_0$ (we assume no external flux in the loop formed by the junction and inductor). The potential of the linear inductor is then $\frac{E_L\varphi^2}{2}$ where $E_L = \phi_0^2/L$ is the inductive energy. This potential is not periodic, and thus breaks the symmetry. The inductance can be very large ($E_L \ll E_J$) and so the Josephson term completely dominates the behavior of the system². This inductance can be understood as a physical stray inductance that shunts the junction or as a theoretical construct, but in any case this addition allows us to treat the Josephson junction within the harmonic oscillator formalism.

Now we see the reason for using the operators φ and N , which are renormalizations to the flux and charge operators defined for linear circuits. The operator φ can also be understood as the superconducting phase difference between the two superconductors connected by the junction. The Hamiltonian for the Josephson junction can now be written as:

$$\mathbf{H} = 4E_C(N)^2 - E_J \cos \varphi, \quad (2.36)$$

and the term $-E_J \cos \varphi$ behaves as a non-linear inductor. We can expand the cosine, as in Eq. 1.5, to obtain the linear and non-linear parts of the inductance.

2.3.2 Combining linear and non-linear elements

Now that we have obtained a quantum expression for the Josephson junction, we are set to write the Hamiltonian for an arbitrary non-linear superconducting circuit.

This can be done in a straightforward way by following the procedure in the beginning of this Chapter. However, for larger circuits this can be quite involved, as the circuit is not longer reducible to its independent modes. Also, one should be careful when making approximations which reduce

²A very important caveat to this statement is the dependence of the system on DC offset charge N_g . With no inductor, this offset charge contributes significantly to the energy levels (see Section 2.4.1). However, an arbitrarily large inductor has zero impedance at DC and thus completely shunts the static charge. In the limit $L \rightarrow \infty$, the AC response of the shunted junction approaches that of the unshunted junction but the true DC response is inconsistent. However, as true DC behavior corresponds to infinite times, it is not experimentally accessible. This inconsistently is addressed in detail in Ref. Koch *et al.* [2009].

the number of DOF in a circuit, as these can lead us to assume an incorrect symmetry and thus obtain an incorrect Hamiltonian.

However, as the entire non-linearity is focused in several elements, we can make use of the reducibility of linear circuits to simplify the calculation significantly. This procedure is known as black box quantization (BBQ) and is presented in Ref. Nigg *et al.* [2012]. It is especially important within the cQED framework, where a non-linearity interacts with several linear modes. In this Section we only treat the case in which the circuit has a single non-linear element. This treatment can be extended to multiple non-linearities, but in that case the analysis is more subtle and complicated [Solgun and DiVincenzo, 2015, Solgun *et al.*, 2014].

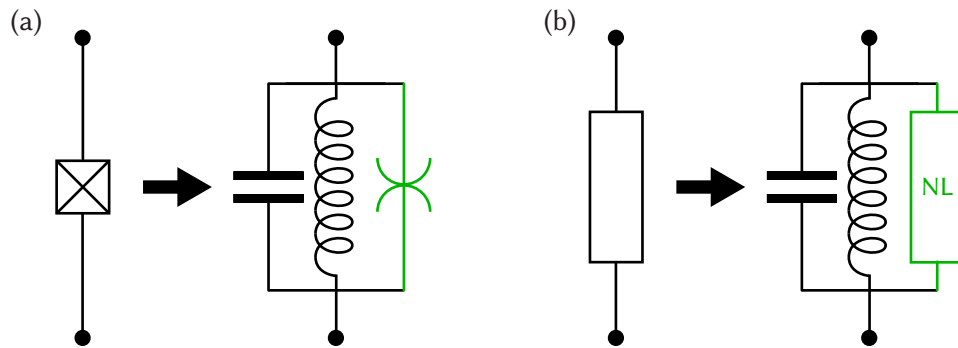


Figure 2.2: (a) The Josephson junction has a non-linear inductance which corresponds to the potential energy $-E_J \cos(\varphi)$. It is often useful to separate it into a linear inductor and capacitor, in parallel with a non-linear “spider” element (green) which is a purely non-linear inductive element with potential energy $-E_J \cos(\varphi) + E_J \varphi^2/2$ (b) This method can be generalized to any lumped element, which we break into its linear part and its purely non-linear part (green). In the case of a non-linear inductance, the potential corresponding to the non-linear element only has terms of the order φ^3 and higher.

We start our treatment by separating the Josephson junction into its linear and non-linear components. As the Josephson capacitance is in parallel with the tunneling element, and we use φ as our position coordinate, it is convenient to express the Josephson junction as a capacitor, linear inductor and non-linear inductor, all in parallel. Fig. 2.2a shows this separation, and the non-linear inductor (green) is represented as a spider element [Manucharyan *et al.*, 2007]. Its

potential energy term can be expressed as:

$$U(\varphi) = -E_J \cos \varphi + E_J \varphi^2 / 2, \quad (2.37)$$

and it is indeed a purely non-linear term. This treatment can be applied in general for any inductive non-linear element. Fig. 2.2b shows the separation of a general circuit element to its linear components and its purely non-linear component (green). This is useful for treating the new non-linear element described in Chapter 5.

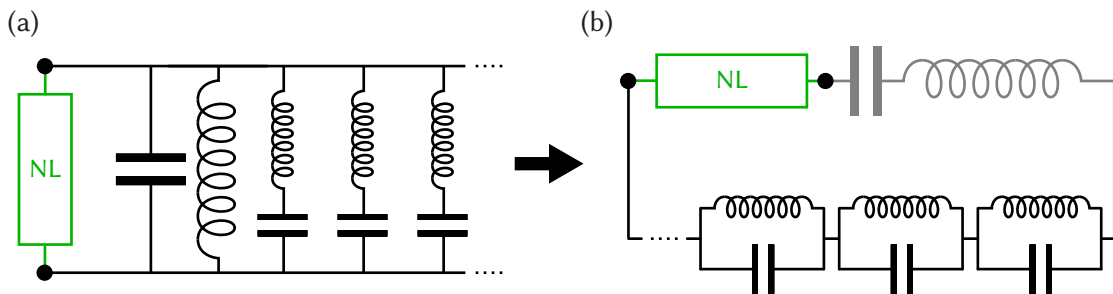


Figure 2.3: If we can isolate the non-linearity into a single element (green), the generic linear circuit attached to it can be diagonalized into a Foster form. (a) and (b) show the parallel and series Foster forms respectively. (a) The current (charge) through the non-linear element is equal to the sum of currents through the normalized harmonic oscillators. (b) The voltage (flux) across the non-linear element is equal to the sum of voltages across the normalized harmonic oscillators.

Any circuit with a single non-linear element can thus be described as a non-linear element in parallel with a linear circuit. The behavior of the linear circuit is completely given by its resonant modes. Thus, we can transform any linear circuit into a combination of independent oscillators. This expansion of an arbitrary impedance into a set of oscillators is sometimes known as the Foster form [Foster, 1924] of a circuit³.

Fig. 2.3 shows our circuit, in which a non-linear element is coupled to a general linear circuit. The circuit is expanded in the parallel (Fig. 2.3a) and series (b) Foster forms respectively. These forms are equivalent representations of the linear circuit. Though as a whole they represent the same circuit, the translation between any inductor and capacitor of one form to the other is

³We use this terminology as it is common and for lack of a better one. The technique of expanding a complex function into its poles, and its use for electromagnetic circuits, likely predates Foster's work.

generally complicated.

Notice that the parallel Foster circuit contains the resonant circuit modes as independent LC oscillators in parallel, and also an additional pure inductor and pure capacitor. Similarly, the series Foster circuit contains a pure inductor and capacitor in series. These elements correspond to the behavior of the circuit at frequencies $\omega = 0$ and $\omega = \infty$.

Though the two circuits are in principle completely equivalent, we break the equivalence between them with our definition of the non-linearity. Our non-linear element was defined as having a linear inductor and capacitor in parallel (see Fig. 2.2), and for a Josephson junction we know precisely what their values are. Thus, in the parallel form of the Foster circuit in Fig. 2.3a, the non-linear element is guaranteed to have a non-zero pure capacitor C_p and a finite pure inductor L_p in parallel. Note that the existence of a finite L_p imposes that the circuit impedance $Y[\omega]$ obeys $Y[\omega \rightarrow 0] \rightarrow \infty$, as it contains a term of the form $\frac{1}{-i\omega L_p}$. Thus, in the equivalent series circuit in Fig. 2.2b, the impedance must obey $Z[\omega \rightarrow 0] \rightarrow 0$. This imposes that the pure series capacitor C_s is infinite, as its impedance is of the form $\frac{1}{i\omega C_s}$. Thus we can remove the series capacitor from the circuit (capacitor is grayed out in Fig. 2.2b). Similarly, the existence of a non-zero parallel capacitor C_p in the parallel circuit imposes $Z[\omega \rightarrow \infty] \rightarrow 0$ and thus the pure series inductor must obey $L_s = 0$ and can be removed from the circuit (inductor is grayed out in Fig. 2.2b).

We have thus established that in the series Foster form, the non-linear element is in parallel with a set of M independent series harmonic oscillators. For each independent oscillator k , we can define the corresponding annihilation operator \mathbf{a}_k and the reduced flux across the oscillator is simply given by $\varphi_k = \frac{\phi_{ZFF}^k}{\phi_0} (\mathbf{a}_k + \mathbf{a}_k^\dagger)$ as we saw in Section 2.2.2. The reduced flux across the non-linear element φ can thus be expressed as $\varphi = \sum_{k=1}^M \varphi_k$ from Kirchhoff's rule.

If we define the potential energy of the non-linear inductive element as $U_{NL}(\varphi)$ (for the Josephson non-linearity, it is given by Eq. 2.37) and the Hamiltonian for the linear circuit as $H_0(\varphi_1, \varphi_2, \dots, \varphi_M)$, we can express the Hamiltonian of the full non-linear circuit:

$$\mathbf{H} = \mathbf{H}_0(\varphi_1, \varphi_2, \dots, \varphi_M) + U_{NL}(\varphi_1 + \varphi_2 + \dots + \varphi_M) \quad (2.38)$$

The non-linear term in Eq. 2.38 is responsible for the non-linear corrections to each of the modes, as well as non-linear couplings between them. For example, the lowest order terms in the Josephson non-linearity include a term of the form:

$$- \frac{E_J (\phi_{ZPF}^1)^4}{4\phi_0^4} \mathbf{a}_1^\dagger \mathbf{a}_1^\dagger \mathbf{a}_1 \mathbf{a}_1, \quad (2.39)$$

which is a fourth-order Kerr non-linearity for linear mode 1. They also include a term of the form:

$$- \frac{E_J (\phi_{ZPF}^1 \phi_{ZPF}^2)^2}{4\phi_0^4} \mathbf{a}_1^\dagger \mathbf{a}_1 \mathbf{a}_2^\dagger \mathbf{a}_2, \quad (2.40)$$

which is a cross-Kerr coupling between the linear modes 1 and 2 (In Chapter 3, this type of dispersive coupling is labeled χ). A coupling of this form can not be removed by a change of coordinates as in the linear case, and a Hamiltonian of the form in Eq. 2.38 cannot generally be separated into M independent uncoupled non-linear modes.

It is important to remember that even though we represent the Hamiltonian in the basis of the linear modes of the circuit, these are not the energy eigenstates of the circuit. For weakly non-linear system it can be a good intuition to think of the system as a set of linear modes perturbed by a non-linearity, but we should still be careful that an operator such as \mathbf{a}_1 does not quite correspond to the annihilation operator of an eigen-mode of the circuit, but can have a more complicated effect. For a strongly non-linear system, the eigen-modes of the system are in general completely different from the linear modes, and expanding the linear modes may not be the best description of a circuit. Even the notion of eigen-modes may not carry over as coupling terms become strong as well - the non-linear circuit is sometimes best described as a complicated arrangement of inseparable eigenstates.

In all these cases, however, the method we described is a convenient way to write the Hamiltonian of the circuit and analyze its eigenstates and dynamics [Smith *et al.*, 2016], even if sometimes this can only be done numerically.

2.4 Common artificial atoms

Even though we only have three basic building blocks: a capacitor, an inductor and a Josephson junction, different values and different combinations for these elements can produce a wide selection of artificial atoms. In this Section we provide a short overview of a few common artificial atoms. These are relatively basic circuits, and are themselves often combined to produce more complicated artificial atoms. This is by no means an exhaustive list, and we focus on circuits which are relevant in later parts of the thesis.

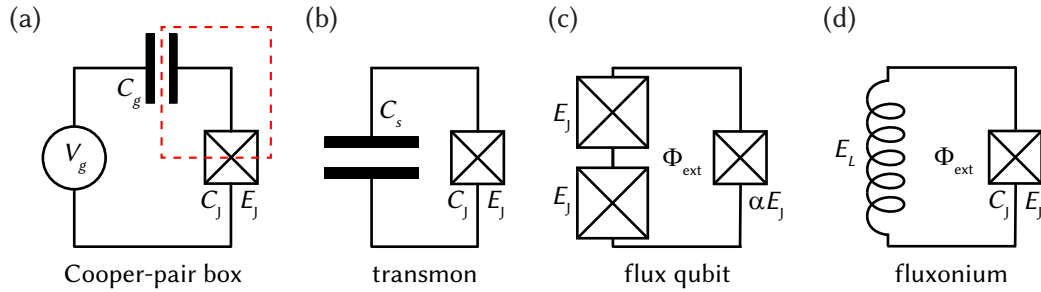


Figure 2.4: (a) The Cooper-pair box, which is made up of a Josephson junction biased by an external voltage V_g through a gate capacitor C_g . The charge on the island (marked by a dashed red line) between the junction and the gate capacitor is the DOF for this artificial atom. (b) The transmon consists of a Josephson junction shunted by a large capacitor C_s , such that $E_C \ll E_J$. The eigenstates of the transmon are similar to those of a harmonic oscillator, with a weak non-linearity provided by the junction. (c) The flux qubit consists of a small junction in parallel with two (or more) identical larger junctions. α is the ratio of their Josephson energies, and a flux Φ_{ext} is threaded through the loop between them. The flux qubit is usually operated at $\Phi_{\text{ext}}/\Phi_0 = 0.5$ where the atomic states correspond to superpositions of clock-wise and counter clock-wise currents. (d) The fluxonium consists of a Josephson junction shunted by a linear inductance L such that $L \gg L_J$. This inductance is itself implemented as an array of large Josephson junctions, and so can be seen as a limit of the flux qubit. The fluxonium is a tunable artificial atom, as its level structure depends strongly on Φ_{ext} .

2.4.1 Cooper-pair box

The Cooper-pair box (CPB) (see Fig. 2.4a) is the father of virtually all modern superconducting atoms. Coherent quantum states were first observed [Bouchiat *et al.*, 1998] and controlled [Nakamura *et al.*, 1999] in this artificial atom. It consists of a Josephson junction connected to an external voltage source V_g by a gate capacitor C_g .

We can write the Hamiltonian for this system as⁴:

$$\mathbf{H}_{CPB} = \frac{4e^2}{2(C_g + C_J)}(\mathbf{N} - N_g)^2 - E_J \cos \varphi, \quad (2.41)$$

where C_J is the capacitance of the Josephson junction and E_J is its Josephson energy. φ is the phase across the junction and \mathbf{N} is the number of Cooper pairs across the junction and the conjugate to φ . $N_g = VC_g/2e$ is an offset charge set by the voltage source. The CPB is operated in the regime $E_C \gg E_J$ where $E_C = \frac{e^2}{2(C_g + C_J)}$ and thus the quantum states of the system are approximately the eigenstates of \mathbf{N} - the discrete charge on the island (dashed red line in Fig. 2.4a) between the junction and gate capacitor.

Notice that the Hamiltonian eigenstates and their energies strongly depend on the value of N_g and at $N_g \bmod 1 = 0.5$ there are two degenerate charge states. This degeneracy is lifted by the Josephson tunneling term, and so the two states are split by E_J - similar to the Zeeman splitting of a spin due to magnetic field.

This original formalism seems to disagree with our derivation of the Josephson junction in Section 2.3.1. In the derivation we introduced a parasitic linear inductance in parallel with the junction which broke the periodicity of the flux, or the charge discreteness, and allowed us to define the normalized charge and flux as continuous operators like those of a harmonic oscillator. This inductance necessarily negates any effect of a static N_g . This can be seen by applying the unitary transformation $\mathbf{U} = e^{iN_g\varphi}$ which simply removes the static offset term from the Hamiltonian [Koch *et al.*, 2009].

This is not true for a time dependent offset, however. In that case the unitary becomes time dependent and the Hamiltonian in the new frame is:

$$\mathbf{H}_{CPB} = 4E_C\mathbf{N}^2 - E_J \cos \varphi - \hbar\dot{N}_g\varphi, \quad (2.42)$$

⁴Note that we have not treated a voltage source within our formalism. This circuit is no longer isolated and thus needs to be addressed as an open quantum system for full treatment. However, we can approximate the source to be a very large capacitor C initially charged with charge Q such that $Q/C \rightarrow V$ as $C \rightarrow \infty$. An inductance L should be added in parallel to obtain the correct behavior at zero frequency. The capacitor will discharge on the timescale \sqrt{LC} but on shorter timescales we approximate this DOF as a static voltage source.

and its eigenstates and energies are clearly affected by N_g . This Hamiltonian should allow us to treat the effects of a charge offset within the BBQ framework.

2.4.2 Transmon

The transmon qubit [Koch *et al.*, 2007] is made up of a CPB shunted by a large inductance $C_s \gg C_J$. This significantly reduces the capacitive energy of the junction so that $E_C = \frac{e^2}{2(C_J+C_s)} \ll E_J$.

The eigenstates of this Hamiltonian are very different from those of the CPB, and are actually quite similar to those of a harmonic oscillator. The large capacitance decreases the zero-point fluctuations in flux, thus allowing us to expand the potential around $\varphi = 0$:

$$\mathbf{H}_{\text{transmon}} = 4E_C \mathbf{N}^2 - E_J \cos \varphi \approx 4E_C \mathbf{N}^2 + \frac{E_J}{2} \varphi^2 - \frac{E_J}{24} \varphi^4 \quad (2.43)$$

The lowest eigenstates of the transmon have energies well within the cosine potential, and thus it can be approximated as a slightly non-linear parabolic potential. The transmon Kerr non-linearity, the first-order correction of its eigenenergies from those of a harmonic oscillator, is approximately given by E_C .

The significant advantage of reducing the capacitive energy is removing the sensitivity of the transmon frequency to charge noise. A drift in the charge offset N_g is screened by the capacitance and no longer affects the transition frequency ω_{ge} between the lowest transmon eigenstates $|g\rangle$ and $|e\rangle$. Thus the transmon can achieve higher coherence times.

2.4.3 Flux qubit

The flux qubit [Mooij *et al.*, 1999, Wal *et al.*, 2000, Chiorescu *et al.*, 2003] is derived from the original proposal by A. J. Leggett of observing macroscopic quantum-coherent oscillations between flux states of the RF-SQUID [Leggett, 1980, 1987]. Instead of the RF-SQUID, which consists of a Josephson junction shunted by a geometric inductance, the flux qubit consists of a Josephson junction shunted by an effective inductance made up of an array of several bigger Josephson junctions in series.

Here we treat a shunting array consisting of two junctions:

$$\mathbf{H}_{FQ} = 4E_C N^2 - \alpha E_J \cos \varphi - 2E_J \cos \left(\frac{\varphi - \Phi_{\text{ext}}/\phi_0}{2} \right), \quad (2.44)$$

where φ is the flux across the small junction, Φ_{ext} is the external flux through the loop, and α is the ratio of the junction sizes, which corresponds to the ratio of their Josephson energies. Note that we have neglected the capacitances of the shunting junctions and the additional DOF associated with them, and treat the shunting junctions as pure inductive elements. This is justified as the frequency of this additional mode is high, and the single DOF φ is sufficient to describe this artificial atom at low energies.

The potential of the small junction has a 2π periodicity in flux, while that of the big junction has a 4π periodicity. The competition between these two terms as a function of Φ_{ext} determines the nature of the flux qubit eigenstates. For most Φ_{ext} values, the flux qubit potential has a single well of the lowest energy, and the ground state $|g\rangle$ adopted by the system resides in that well. The ground state approximately corresponds to a particular current flowing through the loop. At exactly $\Phi_{\text{ext}} \bmod \Phi_0 = \Phi_0/2$, the full qubit potential has two degenerate wells, and thus there are two degenerate current states for the device. This degeneracy is lifted by the capacitive charging term, and the two eigenstates $|g\rangle$ and $|e\rangle$ correspond to the symmetric and anti-symmetric combinations of current propagating clockwise and counter-clockwise. The ground-excited transition energy ω_{ge} is a sensitive function of both Φ_{ext} and E_J .

The coherence time of the flux qubit is significantly reduced when moving even slightly away from the optimal flux point, due to the high sensitivity of the qubit to flux noise. To decrease this sensitivity, a variant of the flux qubit [You *et al.*, 2007] has been proposed in which its E_J/E_C ratio is reduced. While decreasing the sensitivity to flux noise, this qubit is now more sensitive to charge noise. To decrease this dependence, a large capacitance is added in parallel with the junction (similar to the transmon qubit), and so this qubit is often called the C-shunt flux qubit [Yan *et al.*, 2016].

2.4.4 Fluxonium

The fluxonium artificial atom [Manucharyan *et al.*, 2009] is a loop circuit made up of a small Josephson junction (with Josephson energy E_J and capacitive energy $E_C \sim E_J$) in parallel with a large linear inductor L , such that its inductive energy E_L satisfies $E_L \ll E_J$. The Hamiltonian for this circuit is:

$$H_{\text{fluxonium}} = 4E_C N^2 - E_J \cos(\varphi - \Phi_{\text{ext}}/\phi_0) + \frac{E_L}{2} \varphi^2, \quad (2.45)$$

where Φ_{ext} is the external flux through the fluxonium loop.

However, a large physical inductance L , for example a wire of finite length, is always accompanied by a parasitic capacitance C_p . This leads to a L - C_p oscillator mode in parallel with the junction, which must not shunt the junction's the phase fluctuations. We thus need to satisfy $(L/C_p)^{1/2} \gg (L_J/C)^{1/2} \sim R_Q$ where $R_Q = \hbar/(2e)^2 \approx 1\text{k}\Omega$ is the resistance quantum. Such an inductance is known as a “superinductance” [Manucharyan, 2011], and it is impossible to achieve with a geometrical inductance, as its characteristic impedance is always limited by the vacuum impedance of $377\ \Omega$ [Feynman *et al.*, 1963]. Instead, the fluxonium inductance is implemented using an array of large Josephson junctions (see Chapter 4).

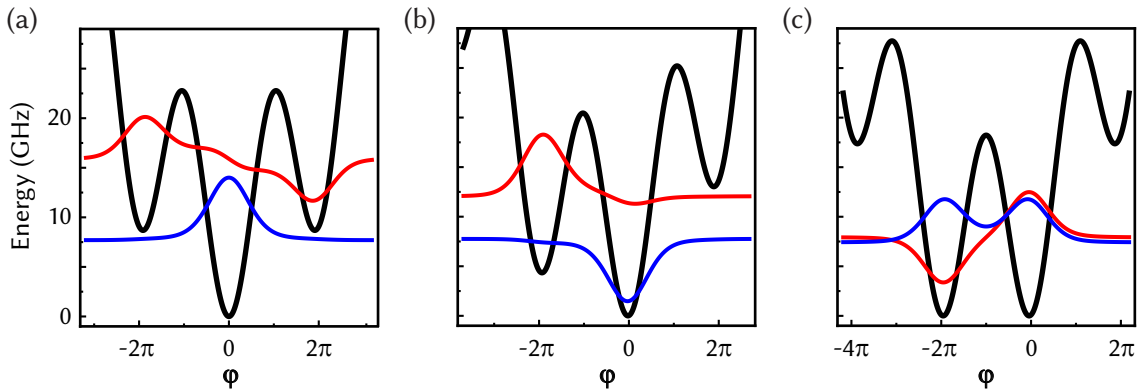


Figure 2.5: The potential (black) and wave-functions of the ground (blue) and excited (red) states of the fluxonium qubit as a function of the superconducting phase across the small junction φ . (a), (b), and (c) correspond to $\Phi_{\text{ext}}/\Phi_0 = 0, 0.25,$ and 0.5 respectively. The fluxonium parameters used for the figure are: $E_C/\hbar = 3.6\text{ GHz}$, $E_L/\hbar = 0.46\text{ GHz}$, and $E_J/\hbar = 10.2\text{ GHz}$. These parameters correspond to the fluxonium measured in Ref. Vool *et al.* [2014].

The fluxonium level structure strongly depends on the value of Φ_{ext} , and this device can be considered a different artificial atom at every flux point. Fig 2.5 shows the fluxonium potential (black) vs. the flux φ , and the wave-functions for its two lowest eigenstates $|g\rangle$ (blue) and $|e\rangle$ (red). These are plotted for $\Phi_{\text{ext}}/\Phi_0 = 0, 0.25,$ and 0.5 in Fig 2.5a, b, and c respectively.

At $\Phi_{\text{ext}} = 0$, the minimum of the parabolic term and the minimum of the cosine term coincide, and thus the low energy fluxonium states are localized around a single well in flux and its first excitations somewhat resemble plasma excitations - such as those of the transmon. At $\Phi_{\text{ext}} = \Phi_0/2$, the minimum of the parabolic term coincides with the maximum of the cosine term, and thus the fluxonium low energy states lie in two degenerate flux wells simultaneously, similar to those of the flux qubit. Also notice that the energy difference between $|g\rangle$ and $|e\rangle$ at this flux point is the lowest, and given by the tunneling rate between the two wells. This frequency is commonly $\omega_{ge} \approx 2\pi \times 500$ MHz.

Between these two external flux points, the fluxonium potential is asymmetric and its lowest energy states reside in separate flux wells. $\Phi_{\text{ext}} = 0$ and $\Phi_0/2$ are known as the “sweet spots” of the fluxonium, where its energy ω_{ge} is first-order insensitive to noise in the external flux.

Similarly to the flux qubit, the inductor suppresses the low-frequency charge noise as it shunts the two sides of the junction. However, due to its large inductance, the fluxonium energy ω_{ge} off of its sweet spots is significantly less sensitive to external flux noise compared to that of the flux qubit.

Chapter 3

Circuit quantum electrodynamics

In atomic quantum-coherent systems, manipulations of the atom are commonly performed using electromagnetic waves. However, as the interaction is weak, the quantum nature of the light itself is often neglected in the treatment of the system. The field of cavity quantum electrodynamics [Haroche and Raimond, 2006, Miller *et al.*, 2005] changed this paradigm and allowed for quantum-coherent interactions between atomic excitations and photons. The photons are the excitations of an optical cavity with low loss, and they interact via dipole coupling with an atom placed inside it (see Fig. 3.1a). The low loss in the system and the strong coupling between the atom and cavity allow for quantum manipulation of the states of the cavity, and its treatment as a coherent quantum system by itself.

Inspired by the achievements of cavity quantum electrodynamics, the field of superconducting artificial atoms adopted a similar framework. In the circuit quantum electrodynamics (cQED) [Blais *et al.*, 2004, 2007] framework, a superconducting artificial atom is coupled to a microwave resonator (see Fig. 3.1b). The resonator itself can be implemented as either a circuit resonator or a microwave cavity [Paik *et al.*, 2011]. As the artificial atom is itself a circuit, the coupling between the artificial atom and cavity can be tuned by changing the value of capacitor, and strong coupling can be easily achieved.

The cQED framework is currently the main way to manipulate and perform measurements on superconducting atoms. It is also used to control the cavity itself as an artificial atom, and encode

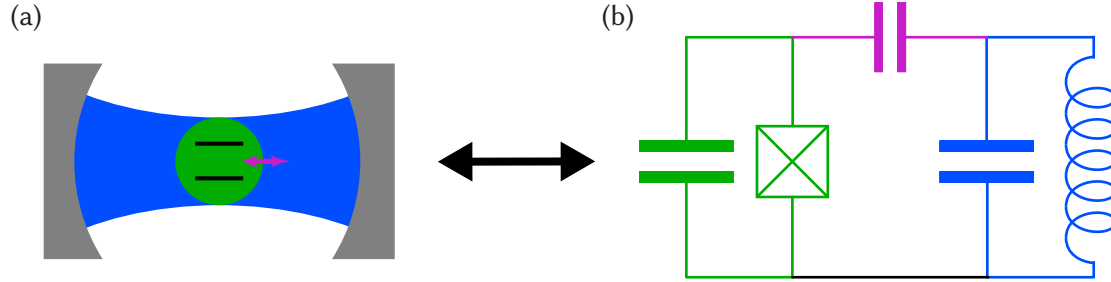


Figure 3.1: The design for a superconducting two-level atom coupled to a linear oscillator is inspired by experiments in cavity QED (left), in which a natural atom (green) interacts with the quantized light of an optical cavity (blue) as it flies through it. In circuit QED (right) the atom is replaced by a non-linear artificial atom while the optical cavity is replaced by a linear resonator. Both objects are macroscopic and coupled by a capacitor (magenta), which allows for independent control of the frequencies and coupling between both modes.

quantum information within it [Mirrahimi *et al.*, 2014].

In this Chapter, we introduce the mathematical formalism of the cQED framework with the addition of external drives and dissipation. We start with a discussion on using either the harmonic oscillator or the spin operators to describe the states of the artificial atom, and the problems with either option. We then proceed to discuss the Jaynes-Cummings (JC) formalism for an artificial atom (qubit) coupled to a cavity, with a focus on the dispersive regime. We then discuss how to add external drives and dissipation to our treatment, and the conditions under which we can approximate the driven system with a Hamiltonian. We finish with a description of an effective qubit drive due to its interaction with the cavity, and the loss of energy and information which the qubit inherits from the cavity due to this interaction.

3.1 Photon or spin?

The Hamiltonian of the artificial atom was derived in Chapter 2 as a non-linear oscillator, and it is convenient to describe it using the operators of a linear oscillator. For a single non-linear DOF, the Hamiltonian in Eq. 2.38 can be expanded in the linear creation and annihilation operators :

$$\mathbf{H}/\hbar = \omega_0 \mathbf{a}^\dagger \mathbf{a} + d_3 (\mathbf{a} + \mathbf{a}^\dagger)^3 + d_4 (\mathbf{a} + \mathbf{a}^\dagger)^4 + \dots \quad (3.1)$$

where ω_0 is the frequency of the linear circuit and d_n are the n -th order non-linear corrections. This is an accurate description of the artificial atom, but the translation between the values w_0 and d_n to the eigenstates and eigenvalues of the system is not straightforward. Note that the linear eigenstates $\{|n\rangle\}$ are not eigenstates of \mathbf{H} !

A much more convenient Hamiltonian may be derived by normal ordering the terms, such that creation operators are always to the left of annihilation operators - note that this mixes terms of different orders due to the commutation relation. We also simplify the Hamiltonian by using the rotating wave approximation (RWA), in which we transfer to the rotating frame $\mathbf{U} = e^{i\hbar\omega_0\mathbf{a}^\dagger\mathbf{a}t}$ and neglect rapidly oscillating terms. This allows us to neglect “non energy-conserving terms” such as $\mathbf{a}^\dagger\mathbf{a}^\dagger\mathbf{a}$. The new approximate Hamiltonian now takes the form:

$$\mathbf{H}_{\text{RWA}}/\hbar = \omega\mathbf{a}^\dagger\mathbf{a} + \frac{K}{2}\mathbf{a}^\dagger\mathbf{a}^\dagger\mathbf{a}\mathbf{a} + \dots \quad (3.2)$$

where ω is the new frequency of the oscillator, which includes corrections from the non-linear terms, and K is the Kerr non-linearity. This Hamiltonian is much more intuitive and provides a very useful description for the behavior of the system. The linear eigenstates are eigenstates of the approximate Hamiltonian \mathbf{H}_{RWA} , and we can utilize our intuition for linear systems to study our circuit. $\hbar\omega$ is indeed the transition energy for the $|0\rangle \leftrightarrow |1\rangle$ transition and $\hbar K$ is the correction in transition energy for the $|1\rangle \leftrightarrow |2\rangle$ transition.

However, many terms have been neglected in this step, and we need to make sure we are still accurately describing our artificial atom. Most importantly, the RWA is only allowed for weakly non-linear systems. If the non-linear coefficients are on the same order as ω_0 , the rotating terms are significant and by neglecting them we have obtained the wrong Hamiltonian. Even for weak non-linearities, the rotating terms can have significant corrections of a higher order and should be taken into account if our non-linearity is expanded to higher orders. The neglected terms can also have significant effects when drives are applied to the system, or when we are interested in the behavior of higher excited states. Higher-order RWA, which includes higher-order corrections due to the rotating terms, can improve the accuracy of the obtained Hamiltonian [Rouchon and

Mirrahimi, 2010].

Another approximation, which is especially useful for strongly non-linear systems, assumes that our non-linearity is infinite and treats our system as a two-level atom with the Hamiltonian:

$$\mathbf{H}_{\text{TLS}}/\hbar = \frac{\omega}{2}\sigma_z \quad (3.3)$$

In this description of the system, we completely neglect the effect of the higher energy states, but instead get an intuition for the behavior of the isolated two-level system formed by the two lowest eigenstates $|g\rangle$ and $|e\rangle$. It is a useful description when we only operate near the frequency ω and all other transition frequencies are significantly different.

There are some correspondences between these two descriptions. The linear energy term $\mathbf{a}^\dagger\mathbf{a}$ corresponds to the Pauli operator σ_z , and the linear amplitude or drive term $(\mathbf{a} + \mathbf{a}^\dagger)$ corresponds to $\sigma_x = (\sigma_- + \sigma_+)$. σ_+ and σ_- are the creation and annihilation operators in the spin 1/2 basis, but note their commutator: $[\sigma_-, \sigma_+] = -\sigma_z$, as opposed to $[\mathbf{a}, \mathbf{a}^\dagger] = 1$. Thus, we should not use the intuition of linear systems to discuss spins and vice versa.

Another noticeable difference is the notion of order. The term $\mathbf{a} + \mathbf{a}^\dagger$ corresponds to the electric field and is said to be first-order. The $\mathbf{a}^\dagger\mathbf{a}$ term corresponds to the energy and is thus second-order. The corresponding spin operators σ_z and σ_x are simply rotations of each other and certainly one is not of higher order than the other. Thus, in strongly non-linear systems we should be careful with the notion of order, as it is not always a good description for the system.

Neither the spin nor harmonic oscillator bases are perfect, but they both capture significant parts of the physics of artificial atoms. The choice of basis depends on the specifics of the system and the effects being studied. Throughout this thesis, we use the harmonic oscillator basis for linear systems such as a cavity mode or resonator, and the spin basis for artificial atoms such as the transmon or fluxonium. Note that the spin basis is not valid if the drives applied on the non-linear system are stronger than its Kerr non-linearity, and thus there is a bound on the applied drives within our description.

3.2 Qubit coupled to a cavity

The system we consider consists of a cavity and a qubit, coupled via dipole interaction. The Hamiltonian for the system, sometimes known as the Rabi Hamiltonian, is given by:

$$\mathbf{H}_R/\hbar = \omega_c \mathbf{a}^\dagger \mathbf{a} + \frac{\omega_q}{2} \sigma_z + g (\mathbf{a} + \mathbf{a}^\dagger) \sigma_x, \quad (3.4)$$

where ω_c is the cavity frequency, ω_q is the qubit frequency, and g is the effective interaction between the qubit and cavity. The more common form of this Hamiltonian is obtained by assuming that $\omega_c \sim \omega_q$ and applying the RWA to neglect rapidly rotating terms. The resulting Hamiltonian is known as the Jaynes-Cummings (JC) Hamiltonian [Jaynes and Cummings, 1963, Haroche and Raimond, 2006]:

$$\mathbf{H}_{JC}/\hbar = \omega_c \mathbf{a}^\dagger \mathbf{a} + \frac{\omega_q}{2} \sigma_z + g (\mathbf{a} \sigma_+ + \mathbf{a}^\dagger \sigma_-) \quad (3.5)$$

This Hamiltonian is analytically solvable, as the ground state $|g, 0\rangle$ is unperturbed by the qubit-cavity interaction, and the excited states are only coupled in pairs. The eigenstates of \mathbf{H}_{JC} are given by:

$$|n+\rangle = \cos \theta_n |e, n\rangle + \sin \theta_n |g, n+1\rangle \quad (3.6)$$

$$|n-\rangle = -\sin \theta_n |e, n\rangle + \cos \theta_n |g, n+1\rangle, \quad (3.7)$$

where $\theta_n = \frac{1}{2} \arctan \frac{2g\sqrt{n+1}}{\Delta}$ and $\Delta = \omega_q - \omega_c$ is the detuning between the cavity and qubit frequencies. θ_n defines the hybridization between the cavity-qubit states, and notice that the hybridization is larger for higher photon numbers n .

The cavity and qubit are never fully isolated from the environment and we assign decay rates κ and Γ which correspond to the cavity and qubit respectively (see the following section for a detailed treatment of dissipation in the system). In most uses, the cavity decay κ is made intentionally high so that the system can be manipulated and measured, and so $\kappa \gg \Gamma$. However, due to their interaction, the cavity can mediate qubit decay - an effect known as the Purcell effect [Purcell, 1946, Houck *et al.*, 2008].

The JC system is said to be in the strong-coupling regime when $g \gg \kappa, \Gamma$. Achieving this regime was the hallmark of cavity QED, and was made simpler by implementing the Hamiltonian in circuit QED. As the coupling term g gets larger and approaches or surpasses the cavity and qubit frequencies ω_c and ω_q , the system is said to be in the ultra-strong-coupling regime or deep-strong-coupling regime [Casanova *et al.*, 2010]. In this regime the full Rabi Hamiltonian must be treated, and the behavior of the system can no longer be isolated into the qubit and cavity dynamics.

In this thesis, we focus on two extreme cases of the Hamiltonian: the resonant case in which $\Delta = 0$, and the dispersive case in which $|\Delta| \gg |g|$.

In the resonant case where $\Delta = 0$, the states are completely hybridized such that $|n_{\pm}\rangle = |e, n\rangle \pm |g, n+1\rangle$. Due to this, the Purcell effect is maximal in this case and the qubit decay is generally dominated by the cavity (see Section 3.3.4 for more details).

In the dispersive case where $|\Delta| \gg |g|$, the qubit and cavity states are weakly hybridized. While the hybridization always increases with photon number, we can focus on the lowest excited states which can be approximately expressed as $|0+\rangle \approx |e, 0\rangle + \frac{g}{\Delta}|g, 1\rangle$ and $|0-\rangle \approx -\frac{g}{\Delta}|e, 0\rangle + |g, 1\rangle$. The interaction between the qubit and cavity is small and the Purcell effect is thus strongly suppressed.

Notice that under the RWA, we can simply ignore the interaction term as it is small and rapidly rotating at the detuning frequency. However, this is too harsh of an approximation as this term has an important second-order correction. To see this, let us apply the Schrieffer-Wolff dispersive transformation $U = e^{\frac{g}{\Delta}(a\sigma_+ - a^\dagger\sigma_-)}$ and keep terms up to first order in $\frac{g}{\Delta}$ [Schrieffer and Wolff, 1966, Blais *et al.*, 2004]. Under this transformation we obtain the Hamiltonian:

$$\mathbf{H}_{\text{disp}}/\hbar = \omega_c \mathbf{a}^\dagger \mathbf{a} + \frac{\omega_q + \chi/2}{2} \sigma_z + \frac{\chi}{2} \mathbf{a}^\dagger \mathbf{a} \sigma_z, \quad (3.8)$$

where $\chi = \frac{g^2}{\Delta}$ is known as the dispersive shift¹. In this frame, the interaction term contributes a Lamb shift to the qubit frequency. More importantly, it leads to a new term in which the cavity

¹Here we can see a good example of the problem with approximating our artificial atom as a two-level system. For the transmon, the higher levels significantly affect the dispersive shift and the correct expression is given by $\chi = \frac{g^2 K}{\Delta(\Delta - K)}$ where K is the Kerr non-linearity of the transmon [Koch *et al.*, 2007].

frequency depends on the qubit state and vice versa. Note that the new cavity and qubit eigenstates are eigenstates of the dispersive Hamiltonian, but the two systems are still not decoupled - this is due to the non-linearity in our system, and impossible for coupled harmonic oscillators.

Even in those cases where the decay of the cavity does not significantly contribute to qubit loss, it erases qubit phase information through the dispersive interaction as the qubit frequency depends on the number of photons in the cavity (see Section 3.3.4 for more details). This should not be seen as a purely negative effect, however, as it is precisely the effect that we utilize to measure the state of the qubit using the cavity (see Section 4.2).

3.3 Adding drives and dissipation

3.3.1 Input-output formalism

There are many ways to describe the physics of open quantum systems [Breuer and Petruccione, 2002]. Here, we follow the input-output formalism [Gardiner and Zoller, 2004] which extends the Heisenberg equation to include the effects of incoming or outgoing fields. We only show an outline of the derivation, for a more complete derivation see Refs. Steck [2007], Clerk *et al.* [2010], Girvin [2011]. Also see Ref. Vool and Devoret [2017] for an alternative derivation.

Let us focus only on the cavity, with its internal Hamiltonian $\mathbf{H}_{\text{cav}} = \omega_c \mathbf{a}^\dagger \mathbf{a}$. The cavity is also coupled to a dissipative bath, which we model as a continuum of modes:

$$\mathbf{H}_{\text{int}}/\hbar = \frac{1}{\sqrt{2\pi}} \int_0^\infty d\omega \sqrt{\kappa(\omega)} \left[\mathbf{a} \mathbf{b}^\dagger(\omega) + \mathbf{a}^\dagger \mathbf{b}(\omega) \right], \quad (3.9)$$

where \mathbf{b} are modes in the bath with the commutation relation $[\mathbf{b}(\omega), \mathbf{b}^\dagger(\omega')] = \delta(\omega - \omega')$. Note that since the modes $\mathbf{b}^\dagger \mathbf{b}$ correspond to a density of photons per unit bandwidth, the \mathbf{b} operators have units of $1/\sqrt{\text{Hz}}$. Also note that we have already assumed the RWA in \mathbf{H}_{int} , as we ignore terms of the form $\mathbf{a} \mathbf{b}(\omega)$.

We can write the Heisenberg equation for \mathbf{a} as:

$$\dot{\mathbf{a}} = -\frac{i}{\hbar} [\mathbf{a}, \mathbf{H}_{\text{cav}} + \mathbf{H}_{\text{int}}] = -i\omega\mathbf{a} - \frac{i}{\sqrt{2\pi}} \int_0^\infty d\omega \sqrt{\kappa(\omega)} \mathbf{b}(\omega) \quad (3.10)$$

This term depends on the time evolution of the modes \mathbf{b} , which we can obtain by solving their own Heisenberg equation and integrating in time. This integral ends up contributing two terms, one due to \mathbf{H}_{int} and the other due to the internal evolution of the modes \mathbf{b} . In general these terms are complicated integrals, but we can simplify them using the Markov approximation where the coupling is independent of frequency: $\kappa(\omega) = \kappa$. This is justified when $\kappa \ll \omega_c$ as only modes in a narrow range of frequencies around ω_c significantly interact with our system.

Under this approximation, the Heisenberg equation becomes:

$$\dot{\mathbf{a}} = -i\omega\mathbf{a} - \frac{\kappa}{2}\mathbf{a} - \sqrt{\kappa}\mathbf{a}_{\text{in}}, \quad (3.11)$$

which is known as the **quantum Langevin equation**.

The second term in Eq. 3.11 corresponds cavity dissipation, and we can see that κ is the energy decay rate of the cavity. The third term corresponds to the incoming field which impinges on the cavity from the bath. It is obtained by integrating the modes \mathbf{b} at an early time t_0 before the interaction started : $\mathbf{a}_{\text{in}} = \frac{i}{\sqrt{2\pi}} \int_0^\infty d\omega \mathbf{b}_0(\omega) e^{-i\omega(t-t_0)}$ where $\mathbf{b}_0 = \mathbf{b}|_{t=t_0}$. Note that the dissipation and drive terms always appear together and are both related to the coupling κ - this is known as the **fluctuation-dissipation theorem**. The units of \mathbf{a}_{in} are $1/\sqrt{s}$, and thus it can be interpreted as the the square-root of the photon flux incoming at the cavity.

This relation can be equivalently derived using the outgoing field \mathbf{a}_{out} :

$$\dot{\mathbf{a}} = -i\omega\mathbf{a} + \frac{\kappa}{2}\mathbf{a} - \sqrt{\kappa}\mathbf{a}_{\text{out}}, \quad (3.12)$$

where \mathbf{a}_{out} is obtained by integrating the modes \mathbf{b} at a later time after the interaction ended. From

Eqs. 3.11,3.12 we can derive the relation:

$$\mathbf{a}_{\text{out}} - \mathbf{a}_{\text{in}} = \sqrt{\kappa}\mathbf{a}, \quad (3.13)$$

which is known as the **input-output relation**. Here we have translated the dynamics of the cavity into a scattering problem, in which it is completely governed by the ingoing and outgoing fields.

3.3.2 Stiff-pump approximation

When we drive the cavity, we interact with it through the incoming field term \mathbf{a}_{in} . This term can be separated into two parts, a classical drive and quantum fluctuations around it: $\mathbf{a}_{\text{in}}(t) = \bar{a}_{\text{in}}(t) + \mathbf{a}_{\text{in}}^0(t)$. If the drive amplitude is much larger than the quantum fluctuations, we can neglect their effect and treat the drive classically. This is known as the **stiff-pump approximation**, as it assumes the pump transfers energy to the cavity without being depleted. Note that it can be done for an arbitrary drive strength on the cavity itself as the drive term is: $E(t) = \sqrt{\kappa}\bar{a}_{\text{in}}(t)$, and for every value of E we can choose an arbitrarily high \bar{a}_{in} and an arbitrarily small κ to compensate. The stiff-pump approximation can be formulated as driving infinitely hard through an infinitely weakly-coupled port.

Under this approximation, we can write Eq. 3.11 as $\dot{\mathbf{a}} = -i\omega\mathbf{a} - \frac{\kappa}{2}\mathbf{a} - E(t)$, and we see an identical equation is obtained by simply adding a term $-i\hbar E(t) (\mathbf{a} + \mathbf{a}^\dagger)$ to the Hamiltonian.

Let us assume we are driving the system with a continuous tone of frequency ω_d . We can write the driven cavity Hamiltonian as:

$$\mathbf{H}_c/\hbar = \omega_c\mathbf{a}^\dagger\mathbf{a} + 2\epsilon \cos\omega_d t (\mathbf{a} + \mathbf{a}^\dagger) \quad (3.14)$$

This is a time-dependent Hamiltonian, but as its time dependence is periodic and we assume $\omega_d \approx \omega_c$, we can transform to a time-independent Hamiltonian by moving to the frame rotating

at the drive frequency ($U = e^{i\hbar\omega_d a^\dagger a t}$) and neglecting rapidly rotating terms. We then obtain:

$$\mathbf{H}_c/\hbar = \Delta_c \mathbf{a}^\dagger \mathbf{a} + \epsilon (\mathbf{a} + \mathbf{a}^\dagger), \quad (3.15)$$

where $\Delta_c = \omega_c - \omega_d$ is the detuning of the cavity drive.

An interesting property of the driven harmonic oscillator is that it can be described as an undriven harmonic oscillator in a different frame. To see this, let us first find the steady-state of the system by writing its Langevin equation:

$$\dot{\mathbf{a}} = -i\Delta_c \mathbf{a} - \frac{\kappa}{2} \mathbf{a} - i\epsilon, \quad (3.16)$$

and setting the left-hand side to zero. We find that the steady-state value for the cavity decay operator is $\bar{a} = \frac{\epsilon}{i\kappa/2 - \Delta_c}$. The steady state of the cavity is the coherent state $|\bar{a}\rangle$, an eigenstate of the annihilation operator \mathbf{a} . Let us now express our system in terms of an operator which describes the fluctuations around this mean $\mathbf{d} = \mathbf{a} - \bar{a}$. Formally, this is done by applying the displacement transformation $U = e^{\bar{a}^* \mathbf{a} - \bar{a} \mathbf{a}^\dagger}$. In this new frame, the quantum Langevin equation is:

$$\dot{\mathbf{d}} = -i\Delta_c \mathbf{d} - \frac{\kappa}{2} \mathbf{d}, \quad (3.17)$$

the equation for an undriven oscillator. The steady state in this frame is the displaced coherent state, which is simply the ground state $|0\rangle$.

3.3.3 Effective qubit drive

We have discussed in detail how to add drives and dissipation to the cavity. Now, let us bring back the qubit term and see how it is affected. Note that generally when we drive the qubit to perform operations on it, the incoming electromagnetic field is not coupled directly to the qubit dipole but the interaction is mediated by the cavity.

We can see this by applying a drive at the cavity with a frequency ω_{qd} , which is close to the qubit frequency ω_q . Thus, we add a term $2\epsilon_q \cos(\omega_{qd}t) (\mathbf{a} + \mathbf{a}^\dagger)$ to the Hamiltonian. Under the

Schrieffer-Wolff transformation we have used to reach the Hamiltonian in Eq. 3.8, this drive term transforms into a qubit drive term $\frac{2\epsilon_q g}{\Delta} \cos(\omega_{qd}t) \sigma_x$. The effect of this drive on the cavity itself is neglected as it is far away from the cavity resonance. The amplitude of the qubit drive in frequency units is commonly known as the Rabi frequency $\Omega_R = \frac{2\epsilon_q g}{\Delta}$.

The driven qubit Hamiltonian can thus be written as:

$$\mathbf{H}_q/\hbar = \frac{\omega_q}{2} \sigma_z + \Omega_R \cos(\omega_{qd}t) \sigma_x, \quad (3.18)$$

and once again we can transform to the rotating frame of the drive ($\mathbf{U} = e^{i\frac{\omega_{qd}}{2}\sigma_z t}$) and neglect rapidly rotating terms:

$$\mathbf{H}_q/\hbar = \frac{\Delta_q}{2} \sigma_z + \frac{\Omega_R}{2} \sigma_x, \quad (3.19)$$

where $\Delta_q = \omega_q - \omega_{qd}$. Note that this already appears to be an undriven Hamiltonian. We can make this transformation explicit by defining a new basis $\tilde{\sigma}_z = \frac{\Delta_q}{\sqrt{\Delta_q^2 + \Omega_R^2}} \sigma_z + \frac{\Omega_R}{\sqrt{\Delta_q^2 + \Omega_R^2}} \sigma_x$, which is simply a rotation on the Bloch sphere (see Fig. 1.2 and Ref. Allen and Eberly [1975]). In this basis the Hamiltonian takes the simple form:

$$\mathbf{H}_q/\hbar = \frac{\sqrt{\Delta_q^2 + \Omega_R^2}}{2} \tilde{\sigma}_z, \quad (3.20)$$

which is precisely an undriven qubit.

We have thus seen that a driven cavity can be transformed into a displaced, undriven cavity whose frequency is the detuning of the drive, and a driven qubit can be transformed into an undriven qubit in a rotated basis which depends on the detuning and amplitude of the drive. These are two simple examples of the ability to create effective artificial atoms from driven quantum systems. In Chapter 6 we will see an effective artificial atom which builds on these two ideas.

3.3.4 cavity-induced decay

The qubit is itself not completely isolated and thus its energy and information can decay to the environment. This decay is both due to the intentional coupling which we use to perform operations

on the qubit, as well as spurious coupling to other decay mechanisms we do not control.

Using NMR terminology, we call the qubit energy relaxation rate Γ_1 and its corresponding time $T_1 = 1/\Gamma_1$. This is the characteristic time for the qubit to reach thermal equilibrium with its environment. As the qubit in the JC Hamiltonian (Eq. 3.5) interacts with the cavity, the cavity lifetime inherently limits the lifetime of the qubit through the Purcell effect².

This cavity-induced decay of the qubit is most pronounced in the resonant JC Hamiltonian where the qubit and cavity are maximally hybridized. In this case, the effective decay rate of the qubit depends on the coupling strength g compared to the cavity decay rate κ .

In the weak coupling regime $g \ll \kappa$, a qubit excitation $|e, 0\rangle$ slowly performs a coherent transformation to $|g, 1\rangle$, which quickly decay to $|g, 0\rangle$. Thus we can use the adiabatic approximation [Steck, 2007] in which the $|g, 1\rangle$ state is never populated, and $|e, 0\rangle$ decays directly to $|g, 0\rangle$. In this case the effective qubit decay rate is given by:

$$\Gamma_1 = 4g^2/\kappa. \quad (3.21)$$

This result can also be obtained by Fermi's golden rule by assuming the state $|g, 1\rangle$ has a density of states of width κ [Girvin, 2011].

In the strong coupling regime $g \gg \kappa$, a qubit excitation $|e, 0\rangle$ performs fast oscillations with the $|g, 1\rangle$ state, sometimes known as vacuum-Rabi oscillations. These oscillations then decay due to κ . In this case, the qubit spends half of its time as a cavity excitation, and thus the effective decay rate is $\Gamma_1 = \kappa/2$.

In the dispersive JC Hamiltonian, this effect is strongly suppressed by the frequency mismatch. As the qubit-like excitation is approximately of the form $|e, 0\rangle + \frac{g}{\Delta}|g, 1\rangle$, it has a probability $(\frac{g}{\Delta})^2$ to be a cavity excitation. Thus the effective decay rate is $\Gamma_1 = (\frac{g}{\Delta})^2 \kappa$.

²Note that here we are referring to the case of a lossy, or "readout" cavity, in which $\kappa \gg \Gamma_1$. There have recently been experiments with long-lived "memory" cavities, whose lifetime is actually limited by the qubit lifetime through the reverse Purcell effect [Reagor *et al.*, 2016].

3.3.5 Cavity-induced dephasing

In addition to energy relaxation, the qubit can be affected by a loss of the phase of the qubit state, due to a noise in its frequency. The process is caused by noise coupled to the σ_z operator of the qubit, as opposed to a T_1 process which is caused by noise coupled to σ_x and σ_y . We label the characteristic dephasing time of the qubit by T_φ and its corresponding rate by $\Gamma_\varphi = 1/T_\varphi$.

In the dispersive JC Hamiltonian (Eq. 3.8), the qubit and cavity are very weakly hybridized and so energy relaxation due to the Purcell effect is suppressed. However, as the qubit frequency depends on the number of photons in the cavity, photon noise causes qubit frequency noise, and thus dephases the qubit [Bertet *et al.*, 2005a, Schuster *et al.*, 2005]. Formally, the fluctuations of the photon number operator $\mathbf{n} = \mathbf{a}^\dagger \mathbf{a}$ couple to the σ_z qubit operator and, in the limit $\chi \ll \kappa$, we can relate the qubit dephasing to the fluctuations in the number of photons using Fermi's golden rule [Ithier *et al.*, 2005]:

$$\Gamma_\varphi = \frac{\chi^2}{2} S_{nn}(\omega = 0), \quad (3.22)$$

where S_{nn} is the power spectral density of the noise in the cavity photon number. Notice that we take the value of the spectral density at zero frequency, as this process causes transitions between states orthogonal to σ_z , such as the states $|\pm\rangle$ - the transverse eigenstates of σ_x , and they are degenerate in energy³. This is unlike T_1 processes which correspond to the spectral density at the qubit frequency ω_q .

The spectral density is derived by first calculating the correlation function $C_{nn}(t) = \langle \mathbf{n}(t) \mathbf{n}(0) \rangle - \langle \mathbf{n}(t) \rangle \langle \mathbf{n}(0) \rangle$ where the expectation is taken over the cavity equilibrium state. The spectral density is then the Fourier transform of the correlation function $S_{nn}(\omega) = \int_{-\infty}^{\infty} dt C_{nn}(t) e^{-i\omega t}$. Clearly, for the cavity ground state $|0\rangle$ the correlation function and the spectral density are zero, and thus there is no dephasing due to photon noise.

³This is true for the basic dephasing which contributes to the decoherence measured in a Ramsey experiment. Protocols such as spin-echo, CPMG, and $T_{1\rho}$ (see Ref. Slichter [1990] for more information on these NMR sequences) are sensitive to the spectral density at different frequencies corresponding to the drives applied. In these cases, it is important to distinguish between $S_{nn}(+\omega)$ which corresponds to spontaneous absorption - a process where energy ω is lost, and $S_{nn}(-\omega)$ which corresponds to spontaneous emission. These protocols thus effectively create an energy difference ω between the transverse eigenstates. This distinction is often irrelevant as the spectral density is symmetric, but it can be engineered to be asymmetric - and so the dephasing prefers one of the transverse eigenstates. This is the idea behind the experiment in Ref. Murch *et al.* [2012], see Section 6.2 for more information.

We separate our discussion into two distinct kinds of photon noise. One is spurious noise, due to a thermal distribution of photons in the cavity, and the other is noise due to a coherent cavity drive. The latter is often called measurement back-action, as it is precisely the protocol we use to measure the qubit state whose back-action is to dephase the qubit [Clerk *et al.*, 2010].

For the driven case, the equilibrium state of the cavity is the coherent state $|\alpha\rangle$ and the calculation can be simplified significantly by moving to the displaced frame $\mathbf{d} = \mathbf{a} - \alpha$. In this frame the cavity equilibrium state is $|0\rangle$ and thus many terms in the correlation function cancel. The result simplifies to:

$$C_{nn}^d(t) = \bar{n} \langle \mathbf{d}(0) \mathbf{d}^\dagger(t) \rangle = \bar{n} e^{-i\Delta_c t - \frac{\kappa}{2} t}, \quad (3.23)$$

where Δ_c is the detuning of the cavity drive from the cavity resonance, and $\bar{n} = \alpha^* \alpha$ is the mean photon-number in the cavity. The corresponding spectral density is then:

$$S_{nn}^d(\omega) = \frac{\bar{n} \kappa}{(\omega - \Delta_c)^2 + (\kappa/2)^2}, \quad (3.24)$$

and so the dephasing rate is given by:

$$\Gamma_\varphi^d = \frac{\bar{n} \chi^2 \kappa / 2}{\Delta_C^2 + (\kappa/2)^2} \quad (3.25)$$

For $\chi \approx \kappa$, we can no longer use Fermi's golden rule. However, the rate can still be obtained from a full solution of the master equation for the system [Gambetta *et al.*, 2006, 2008]. There is an additional complication as the number of photons in the cavity now depends on the qubit state, which affects the detuning of the drive from the cavity. We can thus define for each qubit state $\bar{n}_g = \frac{\epsilon^2}{(k/2)^2 + (\Delta_c - \chi/2)^2}$ and $\bar{n}_e = \frac{\epsilon^2}{(k/2)^2 + (\Delta_c + \chi/2)^2}$. If we take the average photon number $\bar{n} = \frac{\bar{n}_g + \bar{n}_e}{2}$, we can write the full expression for the dephasing term:

$$\Gamma_\varphi^d = \frac{\bar{n} \chi^2 \kappa / 2}{\Delta_C^2 + (\chi/2)^2 + (\kappa/2)^2} \quad (3.26)$$

For dephasing due to thermal population in the cavity, calculating the correlation function is a bit more involved. From Eq. 3.11 we can express $\mathbf{a}(t)$ as a function of $\mathbf{a}_{\text{in}}(t)$ and the thermal

population in the cavity n_{th} is given by $\langle \mathbf{a}_{\text{in}}^\dagger(t) \mathbf{a}_{\text{in}}(t') \rangle = n_{\text{th}} \delta(t-t')$ (see Appendix E in Ref. Clerk *et al.* [2010]). The full derivation is given in Annex A of Ref. Bertet *et al.* [2005b]. Here we quote the final result, which is:

$$C_{\mathbf{nn}}^{\text{th}}(t) = n_{\text{th}}(n_{\text{th}} + 1)e^{-\kappa t} \quad (3.27)$$

And so, in the limit $n_{\text{th}} \ll 1$, we obtain the corresponding spectral density:

$$S_{\mathbf{nn}}^{\text{th}}(\omega) = \frac{2n_{\text{th}}\kappa}{\omega^2 + \kappa^2}, \quad (3.28)$$

and the dephasing rate:

$$\Gamma_{\varphi}^{\text{th}} = \frac{n_{\text{th}}\chi^2}{\kappa} \quad (3.29)$$

For $\chi \approx \kappa$, a full solution of the master equation [Clerk and Utami, 2007, Yan *et al.*, 2016] gives a correction to this formula:

$$\Gamma_{\varphi}^{\text{th}} = \frac{n_{\text{th}}\chi^2\kappa}{\kappa^2 + \chi^2} \quad (3.30)$$

Note that the expressions for the dephasing due to coherent and thermal photons in the cavity are quite similar. The main difference between them is that in the driven case, the noise is due to an interference between the drive amplitude and its fluctuations, and thus the correlation function depends on the amplitude decay rate of the cavity $\kappa/2$, while in the thermal case there is no such interference and the correlation function simply depends on the cavity energy decay rate κ . Thus, the spectral density of the thermal fluctuations is a Lorentzian with twice the width compared to that of the coherent fluctuations. Experimentally, the source of the fluctuations can be verified by measuring the spectral density of the dephasing noise in a $T_{1\rho}$ experiment [Yan *et al.*, 2013, 2016].

In the opposite limit $\chi \gg \kappa$, the dephasing no longer depends on χ as every photon loss in the cavity completely dephases the qubit [Sears *et al.*, 2012]. The dephasing rate is then simply given by the cavity photon loss rate:

$$\Gamma_{\varphi} = \bar{n}\kappa \quad (3.31)$$

Chapter 4

Experimental methods

The theory of superconducting artificial atoms is especially exciting as it lies at the crossroads of many disciplines: superconductivity and condensed matter physics, electromagnetism and electric circuits, quantum optics and atom-light interaction, and quantum information. Until this point, the thesis has focused on the theoretical aspects and touched on some of these disciplines and how they combine. The physics of experimental superconducting artificial atoms also lies at a crossroads between many experimental techniques, and a successful experiment requires combined knowledge in a large variety of tasks.

We can list some of the main techniques in the chronological order of the experiment. Electron-beam lithography is used to prepare the superconducting Josephson circuits. Sample packaging must be done carefully to maximally isolate our system from the spurious environment, and some sample holders - such as microwave cavities - are themselves part of the experiment and treated as quantum mechanical objects. A dilution refrigerator is used to cool the samples to $\approx 20\text{mK}$, and proper thermalization of the sample is crucial. Flux-tunable samples are controlled through an external superconducting coil using a DC source. Most operations on the quantum system are performed using RF signals, and our experiments depend on the stability of RF generators and the fast control of their amplitude and phase. The artificial atoms are measured using heterodyne interferometry.

In this thesis, we only touch on a few specific experimental methods used in superconducting

artificial atoms. For details on techniques not covered here, please see other Yale theses which discuss them in depth, such as Kurtis Geerlings' thesis given in Ref. Geerlings [2013].

In this chapter, we focus on the preparation of our sample. We describe the process of making our Josephson circuits using electron-beam lithography, with a focus on fluxonium fabrication. We also describe two sample holders: the 3D cavity and the waveguide. A waveguide was used to measure the fluxonium in the experiment described in Chapter 5, and a 3D cavity was used to measure the transmon in the experiment described in Chapter 6.

We also discuss the readout - how measurements are performed on our system. We focus on dispersive readout, which allows us to continuously monitor the state of the qubit. We compare the measurement of our system by transmitting a microwave tone through our resonator or reflecting off of it, and discuss the obtained signal and the advantages of each method.

4.1 Sample preparation

4.1.1 Sample fabrication

The fabrication of transmon and fluxonium atoms in the 3D architecture requires only a single fabrication step. We use e-beam lithography to write a pattern which includes Al capacitive and inductive structures, and Al/AlO_x/Al Josephson junctions. The junctions used for the experiments in Chapters 5 and 6 were fabricated using the bridge-free fabrication technique [Lecocq *et al.*, 2011, Pop *et al.*, 2012], which was developed in Grenoble.

As its name suggests, the bridge-free fabrication technique is distinguished from the traditional Dolan bridge technique [Dolan, 1977], in which the junctions are made by double-angle evaporation across a bridge of resist. The size of the bridge then determines the size of the junction, and thus the junction sizes are limited by our ability to make resist bridge.

In bridge-free fabrication, however, the junctions are simply formed by holes in the resist, and thus can be of arbitrary size. The more complicated structures are the wires connecting to the junctions. By using a two-layer resist stack, a "spring-board" of resist is formed - where the bottom layer has an undercut and thus the top layer extends further over it. Double-angle evaporation

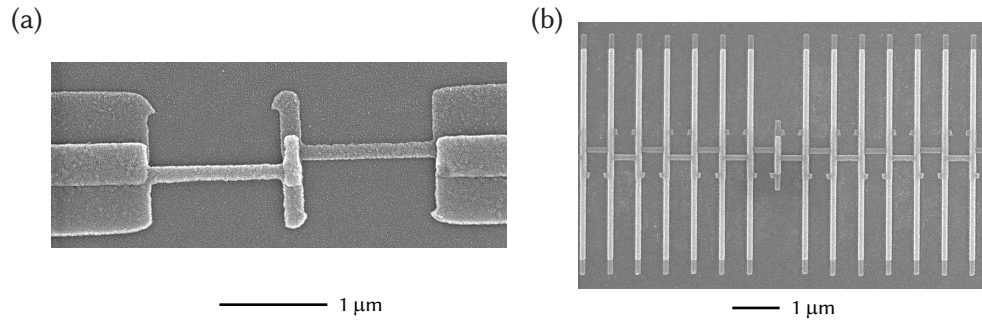


Figure 4.1: (a) An SEM image of a transmon junction fabricated using the bridge-free technique. The middle part shows a junction made up of two aluminum layers sandwiching an aluminum oxide barrier. The top layer is connected to the left transmon pad, and the bottom is connected to the right one. (b) The bridge-free technique is especially useful for making junction arrays. This SEM image shows the small junction of a fluxonium atom, connected to larger array junctions. The connections between the junctions switch between connecting the top and bottom layers.

is then used to selectively pattern the wires: metal deposited at an angle facing the undercut will reach the substrate, and metal deposited facing away from it will not. Fig. 4.1a shows an SEM image of a typical transmon junction made using bridge-free fabrication. The junction is the structure in the middle, where two layers of Al are sandwiched by AlO_x. The left lead connects the left transmon pad to the top layer of the junction, and the right lead connects only the right transmon pad to the bottom layer of the junction. The lead connecting the bottom layer of the junction to the left pad was cut by the springboard pattern of the resist, and similarly the lead connecting the top layer to the right pad was cut by an opposite springboard pattern.

The bridge-free fabrication technique is especially useful for fabricating chains of Josephson junction, and thus is used for Josephson arrays [Masluk *et al.*, 2012] and the fluxonium artificial atom [Pop *et al.*, 2014, Vool *et al.*, 2014]. Fig. 4.1b shows an SEM image of a cut from a fluxonium artificial atom. The small junction in the middle is surrounded by an array of larger junctions which form the large shunting inductance of the fluxonium. The leads connecting the junctions alternate between connecting their top layers and their bottom layers, and thus the only path in the circuit is through all the junctions. The array junctions are large and skinny - a pattern which is impossible using the Dolan bridge technique. This allows for large junctions, while minimizing the capacitance to ground.

The techniques used to make transmon and fluxonium patterns are identical, and only the pattern is different. Here we describe the process used for creating the fluxonium atoms measured in Chapter 5, but up to slight variations, this represents the recipe for all bridge-free devices made at Yale at the time of writing.

The wafer we use as a substrate is a 2 inch, 420 μm thick, double-sided polished c-plane sapphire. The substrate is cleaned in heated NMP (90 $^{\circ}\text{C}$) for 10 minutes, sonicated in NMP and rinsed with acetone and methanol. Microchem EL-13 copolymer resist is spun onto the wafer at 2000 RPM for 100 seconds and then baked at 200 $^{\circ}\text{C}$ for 5 minutes. Then a second resist layer of Microchem A-4 PMMA resist is spun onto the wafer at 2000 RPM for 100 seconds and then baked at 200 $^{\circ}\text{C}$ for 15 minutes. The wafer is then coated in a ≈ 10 nm gold layer to prevent charge accumulation in the substrate during the e-beam write.

The pattern is written on the device using a Vistec electron beam pattern generator (EBPG) 5000+ with a 100 kV electron beam. After the write, the gold is removed from the substrate using a potassium iodine gold etch. The double-layer resist is developed by manually wiggling the device in a 3:1 IPA:water mixture at 6 $^{\circ}\text{C}$ for 2 minutes. The resist patterns can at this point be observed using an optical microscope.

Aluminium is deposited on the device using the Plassys UMS300 UHV multi-chamber evaporation system. In the load-lock chamber, the sample is cleaned using an argon/oxygen plasma for 1 minute¹. The sample is then transferred to the deposition chamber, and an initial titanium sweep is performed to clean the chamber (none is deposited on the device). The first layer of 20 nm aluminium is deposited onto the substrate, and it is moved to the oxidation chamber. The first layer is oxidized in a 15% oxygen, 85% argon mixture, for varying pressures and times depending on the device (for the fluxonium samples, we used 100 Torr for 14 minutes). A second layer of 30 nm aluminium is then deposited, followed by a capping oxidation layer to protect the device.

Finally, the resist and excess aluminum are removed in lift-off by soaking the device in 70 $^{\circ}\text{C}$

¹See Ref. Pop *et al.* [2012] for the importance of cleaning in high pressure to prevent junction aging. Pop *et al.* use a reactive ion etcher to achieve a pressure of 3×10^{-1} mbar of oxygen and clean for 15 seconds (see reference 10 in their paper). We use the cleaning process in the UMS300 and with maximal flow of oxygen and argon reach only 3×10^{-3} mbar. The cleaning time of 1 minute was chosen as it removes 30 nm of resist out of a total of 200 nm in the A-4 layer. This recipe reduced the aging of Josephson junctions to about 5 – 10%, compared to the 20% or more which was observed with the older recipe: cleaning at a total pressure of 4×10^{-4} mbar for 2 minutes.

NMP for 2 hours, and sonicating for 1 minute.

4.1.2 Sample holder

The 3D architecture for superconducting circuits is currently the standard architecture used at Yale as well as in other groups. Unlike the traditional 2D architecture, where the entire circuit is printed on a chip and connected using wirebonds, in the 3D architecture the chip is suspended inside a 3D metallic box and all interaction with it is done through electromagnetic fields. The significant advantage of this architecture is that a larger fraction of the electromagnetic field of the modes in our system is in vacuum, the lowest loss material, and thus the system is more isolated from its environment, and coherence times are higher [Paik *et al.*, 2011].

The designs of devices in the 3D architecture are continuously developing and improving [Axline *et al.*, 2016, Blumoff *et al.*, 2016, Reagor *et al.*, 2016, Brecht *et al.*, 2017], but in this thesis we focus on two simple examples: the rectangular cavity and the waveguide.

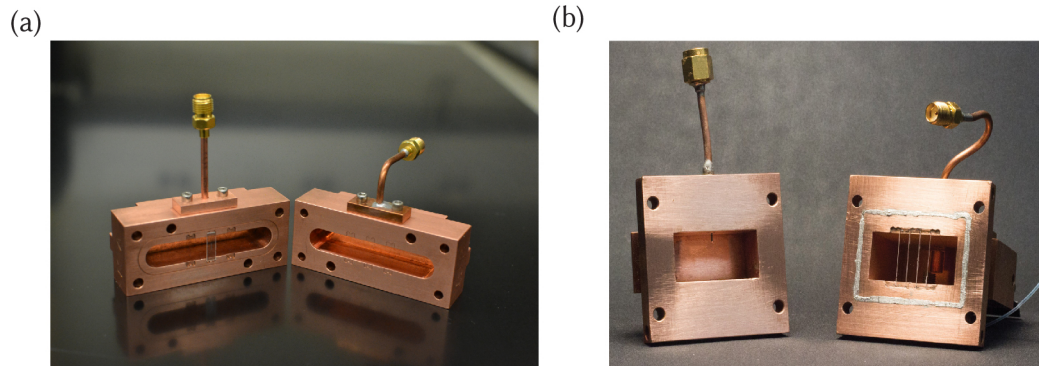


Figure 4.2: (a) A copper cavity acts both as a sample holder and a harmonic oscillator coupled to the non-linear qubit. The chip of the sample is placed in one of the slots. There are two connectors leading into the cavity, which allow for measurement in transmission. One is a weakly coupled input port and the other is a strongly coupled output port which sets the quality factor of the cavity. Any control of the qubit is mediated through the cavity. (b) A waveguide allows for independent readout of several samples. In this design the readout mode is an antenna patterned on each chip and inductively coupled to the qubit. One pin (on the right) is designed to be impedance matched and readout is performed in reflection. A second, weakly coupled, pin (left) allows us to drive transitions which are far below the waveguide cutoff, such as the fluxonium at half a flux quantum.

In the rectangular cavity (see Fig. 4.2a), the electromagnetic field lives in the region of va-

cuum inside it, with the metal walls imposing the boundary conditions. The fundamental mode supported by the cavity is the TE_{101} mode, a transverse electric mode in which the electric field everywhere is pointing in the y direction, and its field structure is constant in the y -direction, while tracing half an oscillation in the x and z -directions. In Fig. 4.2a, the y -direction is the vertical direction, where the rectangular box length is shortest. The frequency of the mode can be easily obtained from the dimensions of the cavity [Pozar, 2011]. The frequency can be adjusted *in situ* to a certain extent by adjusting the length of a screw which enters the cavity, and thus changing the cavity mode from the rectangular ideal.

The cavity has several slots in which we insert our sapphire chips. Once the sapphire chips are in place, we fasten them to the cavity walls using indium wires, and close the two sides of the cavity using indium wires as well. Note that there are no wires leading out from the circuit on the chip, and they interact with the cavity mode via dipole coupling.

Fig. 4.2a shows two coaxial cables connecting to the cavity. Their pins are inserted into the cavity, and the length of the pin in the cavity determines the coupling κ between the cavity and the traveling wave in the cable (see Section 3.3). The two pins usually correspond to an input and an output pin, such that $\kappa_{\text{in}} \ll \kappa_{\text{out}}$. The weakly coupled input pin is used to drive the cavity, and the output pin is used for measurement - the electromagnetic field leaves the cavity through this pin into the measurement chain. This two-pin setup allows us to measure the cavity in transmission, while a single output pin is sufficient for reflection measurement (see the following section).

The cavity also has an inherent decay rate due to its spurious internal environment, which we label κ_{sp} . For a good measurement of the system, we require all the electric field leaving the cavity to reach our measurement setup, and thus $\kappa_{\text{out}} \gg \kappa_{\text{sp}}$. Usually, the output pin is chosen so that $Q_{\text{out}} = \omega_c / \kappa_{\text{out}} \approx 2000$ or $\kappa_{\text{out}} \approx 4$ MHz, allowing for fast readout. This places a strong bound on the internal quality factor of the cavity.

The commonly used rectangular cavities are made out of high purity (4N) aluminum or oxygen-free high-conductivity (OFHC) copper. Aluminum cavities are superconducting, and thus can reach internal quality factors in the millions (and much higher with non-rectangular designs [Reagor *et al.*, 2013]). Copper cavities, on the other hand, are limited to roughly $Q_{\text{sp}} \approx 10^4$. However,

copper cavities have the advantage of being easier to thermalize, and more importantly they allow magnetic field to enter. Thus, all experiments with magnetically tunable circuits, such as the SQUID transmon or the fluxonium, require the use of a copper cavity.

The waveguide, shown in Fig. 4.2b, is physically very similar to the cavity as it is also a rectangular box, but conceptually quite different. The main difference comes from the coupler, shown connecting to the right piece of the waveguide in Fig. 4.2b. Unlike the weakly-coupled pin used for the cavity, the coaxial cable is coupled to the waveguide using an impedance-matched adapter. Thus, the waveguide can be viewed as an extension of the coaxial cable - with the traveling wave through the cable being converted to a traveling wave through the waveguide.

The waveguide in Fig. 4.2b is a WR-102 waveguide made out of OFHC copper. The waveguide works best between its first and second fundamental modes, which can be tuned using a screw similar to the cavity, but are around 6 – 8 GHz. Below the first mode, the transmission through the waveguide is exponentially suppressed, while above the second mode the situation is more complicated as multiple modes can propagate.

As the waveguide plays the role of a transmission line and not a resonator, we use it to measure a 2D resonator patterned on the sapphire chip. This technique is especially useful for the fluxonium qubit, which has a small dipole moment and is thus coupled to its electromagnetic environment through an antenna that shares part of its inductance with the fluxonium [Pop *et al.*, 2014]. The waveguide allows us to use the antenna as a readout resonator for the fluxonium, while still benefiting from the low-loss environment of the 3D architecture. The signal coming from the resonator is measured in reflection through the impedance-matched port. A second, weakly-coupled port, shown on the left in Fig. 4.2b, is placed closer to the sample itself. It is used to directly drive the fluxonium $|g\rangle \leftrightarrow |e\rangle$ transition, which is far below the exponential cutoff of the waveguide.

The waveguide also allows for multiplexed readout within the 3D architecture, as multiple artificial atoms and resonators can be placed in the waveguide and measured simultaneously. Ref. Kou *et al.* [2017] shows the first simultaneous single-shot continuous measurement of two qubits, using two fluxonia in a waveguide.

4.2 Readout

In Chapter 3 we have seen that a driven resonator stabilizes to the coherent state $|\alpha\rangle$ with $\alpha = \frac{\epsilon}{i\kappa/2 - \Delta_c}$, where ϵ is the drive amplitude, κ is the cavity decay rate and Δ_c is the detuning between the cavity drive and resonance frequency. Thus, if we send a coherent drive into the cavity and then wait for the state of the cavity to leak out into the output port, the amplitude and phase of the outgoing field contains information about cavity properties.

However, in the case of the dispersive JC Hamiltonian (Eq. 3.8), the frequency of the cavity depends on the state of the qubit: $\omega_c + \frac{\chi}{2}\sigma_z$. Thus, an applied cavity drive creates a coherent state in the cavity which depends on the state of the qubit. The drive, together with the dispersive coupling, entangles the states of the qubit and the cavity. By measuring the coherent state coming out of the cavity, we can thus measure the state of the qubit. This type of measurement is known as **dispersive readout**, and it is the most common readout within the cQED framework.

4.2.1 Measuring the outgoing field

Before we discuss how qubit information is encoded in the outgoing field of the cavity, let us examine the measurement of the cavity field itself, which is done using heterodyne interferometry. The outgoing field exits the cavity at the drive frequency ω_d . It is down-converted to an intermediate frequency (IF), and sent to a digitizer². An additional reference tone at the IF frequency is also sent to the digitizer. By combining our digitized signal with the reference signal in and out-of-phase, we obtain the real and imaginary components of the outgoing field. These components are sometimes called the in-phase (I) and quadrature (Q) components.

In Section 3.3.1, we described the outgoing field \mathbf{a}_{out} in units of $1/\sqrt{s}$. The outgoing photon number operator $\mathbf{a}_{\text{out}}^\dagger \mathbf{a}_{\text{out}}$ is thus in units of $1/s$, as it corresponds to the photon flux coming out of the cavity. To obtain a measurement of the outgoing field, we measure it for a time T . The total

²In the experiments described in this thesis, readout digitization and manipulation, as well as generation of RF control sequences, were done using an Innovative Integration field-programmable gate array (FPGA) setup with in-house logic. See the theses by Yehan Liu [Liu, 2016] and Andrei Petrenko [Petrenko, 2016] for more information.

photon number in the measurement is³:

$$n_{\text{meas}} = \langle \mathbf{a}_{\text{out}}^\dagger \mathbf{a}_{\text{out}} \rangle T \quad (4.1)$$

This is a useful quantity to define the units for I and Q . We describe them in units of $\sqrt{\text{photon}}$ [Vool *et al.*, 2014]. Up to an arbitrary choice of the phase of the reference IF tone, we can relate these field components to the outgoing field by:

$$\begin{aligned} I &= \text{Re} \langle \mathbf{a}_{\text{out}} \rangle \sqrt{t} \\ Q &= \text{Im} \langle \mathbf{a}_{\text{out}} \rangle \sqrt{t} \end{aligned} \quad (4.2)$$

To calibrate the field components in these units experimentally, we first calibrate the photon number in the cavity [Vijay *et al.*, 2012] and then convert this photon number to the photon number n_{meas} in the integrated outgoing wave-packet. This conversion is different for transmission and reflection, and is described in the following section. Once we have obtained n_{meas} , we can just calibrate the field components by $I^2 + Q^2 = n_{\text{meas}}$.

4.2.2 Measurement in transmission and reflection

We separate our discussion into two measurement types: measurement in transmission, where a drive tone through the weakly-coupled input port is transmitted through the cavity to the output port, and measurement in reflection, where a drive tone is reflected off of the cavity through the output port.

Though it requires two pins, transmission measurement is often seen as the simpler case. In transmission measurement, the drive on the cavity is performed through a weakly coupled input port with coupling $\kappa_{\text{in}} \ll \kappa_{\text{out}}$. Other than providing the coherent population in the cavity, this port can be completely neglected. As no drive is applied at the output port, the input-output

³Note that in this case we assume a continuous drive and thus a continuous outgoing field which we measure for a time T . More commonly, the measurement is a pulse with envelope $\epsilon(t)$. Thus, to obtain all the information, the integration needs to be weighed by the pulse amplitude as a function of time. In this case, we represent the measurement in units of the total photon number in the pulse wave-packet.

relation for it (see Eq. 3.13) can be simplified to $\mathbf{a}_{\text{out}} = \sqrt{\kappa}\mathbf{a}$, where we identified $\kappa = \kappa_{\text{out}}$ as it is the dominant decay channel. The electromagnetic field coming out of the cavity is thus identical to the electromagnetic field in the cavity, up to a constant.

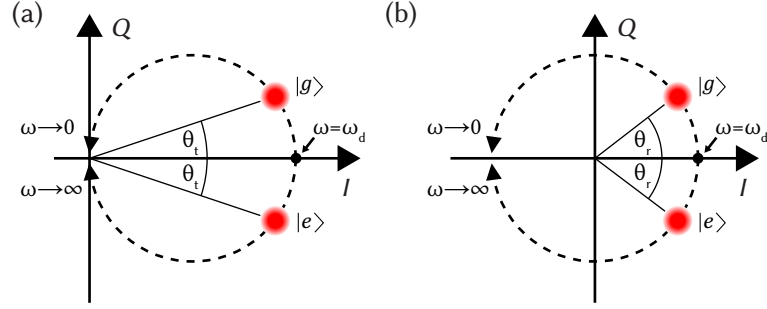


Figure 4.3: The response of a harmonic oscillator with resonance frequency ω to a continuous tone at frequency ω_d . It is represented in the two quadratures I and Q of the electromagnetic field, and the dashed line shows the average response for different resonant frequencies ω . The two red circles mark the $|g\rangle$ and $|e\rangle$ states of the qubit, corresponding to the frequencies $\omega = \omega_d - \chi/2$ and $\omega_d + \chi/2$ respectively. (a) Transmission measurement in which the information is encoded in both the amplitude and the phase of the outgoing signal. (b) Reflection measurement in which the amplitude is always unity (the incoming signal must be fully reflected) and the information on the measured system is only encoded in the phase. Note that for a given number of photons in the cavity, the SNR is identical in both measurement schemes as the separation between the $|g\rangle$ and $|e\rangle$ states is identical. However, notice that there are more photons leaving the system in a transmission measurement with a given SNR and thus reflection measurement is more efficient when comparing outgoing photons.

Depending on the state of the qubit, the amplitude of the coherent state in the cavity is $\alpha_g = \frac{\epsilon}{i\kappa/2 - \Delta_c + \chi/2}$ or $\alpha_e = \frac{\epsilon}{i\kappa/2 - \Delta_c - \chi/2}$. For the case $\Delta_c = 0$, where the drive frequency is in-between the two resonances corresponding to the two qubit states, the measured field components I and Q of the outgoing field are sketched in Fig. 4.3a. This I - Q plane is analogous to the phase space, but notice these are integrated outgoing fields and not system DOF. The points corresponding to the qubit being in $|g\rangle$ and $|e\rangle$ are marked in red. The dashed line corresponds to the I and Q values for the response of a cavity with varying resonance frequency ω but with identical drive amplitude ϵ and frequency ω_d , and an identical decay rate κ . We can see the response goes to zero as $\omega \rightarrow 0$ and $\omega \rightarrow \infty$, and that this response traces a perfect circle in phase space. The angle θ_t quantifies how effective our measurement is at differentiating the two qubit states. It shows how much of the outgoing amplitude we can utilize to distinguish between them.

For a transmission measurement, the I and Q values are simply equal to the real and imaginary parts of the coherent state amplitude in the cavity, with the added constant $\sqrt{\kappa T}$ (see Eq. 4.2). Thus we can calculate the expected field components. Remember that the orientation of the I - Q plane is related to the arbitrary phase of the reference signal, compared to the phase of the input drive. In Fig. 4.3, we chose a convenient frame which can be expressed as $\epsilon \rightarrow i\epsilon$. Note that this is only done to make the figure clearer, and any other phase provides an equally good description of the measurement. Using this frame, we can write:

$$\begin{aligned}
 I_g^t &= \sqrt{\kappa T} \operatorname{Re} \frac{i\epsilon}{i\kappa/2 + \chi/2} = \sqrt{\kappa T} \frac{2\epsilon\kappa}{\kappa^2 + \chi^2} \\
 Q_g^t &= \sqrt{\kappa T} \operatorname{Im} \frac{i\epsilon}{i\kappa/2 + \chi/2} = \sqrt{\kappa T} \frac{2\epsilon\chi}{\kappa^2 + \chi^2} \\
 I_e^t &= \sqrt{\kappa T} \operatorname{Re} \frac{i\epsilon}{i\kappa/2 - \chi/2} = \sqrt{\kappa T} \frac{2\epsilon\kappa}{\kappa^2 + \chi^2} \\
 Q_e^t &= \sqrt{\kappa T} \operatorname{Im} \frac{i\epsilon}{i\kappa/2 - \chi/2} = \sqrt{\kappa T} \frac{-2\epsilon\chi}{\kappa^2 + \chi^2},
 \end{aligned} \tag{4.3}$$

where $I_{g/e}^t$ correspond to the I values for the qubit being in $|g\rangle$ and $|e\rangle$ respectively, and the same for $Q_{g/e}^t$. The two states of the cavity have the same I value and opposite Q values, as plotted in Fig. 4.3a. We can also see that:

$$\theta_t = \arctan \frac{\chi}{\kappa} \tag{4.4}$$

In a reflection measurement, the drive is applied through the output port, and the input-output relation also includes an input field: $\mathbf{a}_{\text{out}} = \sqrt{\kappa}\mathbf{a} + \mathbf{a}_{\text{in}}$. In the stiff-pump approximation, this additional term can be seen as a displacement \bar{a}_{in} of the output field compared to the field in the cavity. Physically, this corresponds to the sum of the signal coming from the cavity, and the signal reflecting directly from the cavity entrance, both adding to the outgoing field.

From the definition of the incoming field \bar{a}_{in} and the amplitude ϵ under the stiff-pump approximation in Section 3.3.2, we can see that $\bar{a}_{\text{in}} = \frac{i\epsilon}{\sqrt{\kappa}}$. Thus the amplitude of the outgoing field is:

$$\langle \mathbf{a}_{\text{out}} \rangle = \sqrt{\kappa} \langle \mathbf{a} \rangle + \bar{a}_{\text{in}} = \frac{\sqrt{\kappa}\epsilon}{i\kappa/2 - \Delta_c} + \frac{i\epsilon}{\sqrt{\kappa}} = \frac{\epsilon}{\sqrt{\kappa}} \frac{\Delta_c + i\kappa/2}{-i\Delta_c - \kappa/2} \tag{4.5}$$

Notice that the amplitude of the outgoing field is independent of the detuning. This is not surprising, as there is only one port and energy cannot be lost elsewhere - and so must be reflected back. The information on the detuning is encoded entirely in the phase. Fig. 4.3b shows a sketch of the I - Q plane for a reflection measurement with $\Delta_c = 0$. Notice that the measured signal is just a displacement of the transmission measurement in Fig. 4.3a, and that for a given cavity frequency ω , the response is always of equal amplitude (dashed line). Now it is obvious why the transmission response as a function of ω is a perfect circle, as it is simply a displacement of the reflection response, which must be a circle around the origin.

The I and Q values can now be expressed for the reflection measurement (once again we choose the convenient rotation $\epsilon \rightarrow i\epsilon$):

$$\begin{aligned}
 I_g^r &= \sqrt{T} \operatorname{Re} \frac{-i\chi/2 - \kappa/2}{i\chi/2 - \kappa/2} = \sqrt{T} \frac{\kappa^2 - \chi^2}{\kappa^2 + \chi^2} \\
 Q_g^r &= \sqrt{T} \operatorname{Im} \frac{-i\chi/2 - \kappa/2}{i\chi/2 - \kappa/2} = \sqrt{T} \frac{2\chi\kappa}{\kappa^2 + \chi^2} \\
 I_e^r &= \sqrt{T} \operatorname{Re} \frac{i\chi/2 - \kappa/2}{-i\chi/2 - \kappa/2} = \sqrt{T} \frac{\kappa^2 - \chi^2}{\kappa^2 + \chi^2} \\
 Q_e^r &= \sqrt{T} \operatorname{Im} \frac{i\chi/2 - \kappa/2}{-i\chi/2 - \kappa/2} = \sqrt{T} \frac{-2\chi\kappa}{\kappa^2 + \chi^2}
 \end{aligned} \tag{4.6}$$

Note that the distance in phase space between the states $|g\rangle$ and $|e\rangle$ is identical in both measurement techniques, and thus you could say they are equally good at distinguishing the qubit states. This is not quite correct, as notice that while the measurement sketches in Fig. 4.3a and b have the same separation between the states, the amplitude of the outgoing field is smaller in the reflection measurement. This is also expressed by the fact that $\theta_r = 2\theta_t$. A good way to resolve this issue is to separate the discussion into energy in the cavity and outgoing energy. The two sketches are made so that they have equal population in the cavity, and thus, per **photon in the cavity**, they contain the same information. However, in reflection measurement the cavity signal mixes with the reflected signal \bar{a}_{in} and is partially canceled. Thus, per **photon in the outgoing field**, the reflection measurement contains more information. This can be very useful if our measurement chain saturates above a certain threshold. Thus, while the reflection measurement is less intuitive

(peaks in amplitude are easier to understand than a change in the phase), it always contains more information. Or as Michel Devoret put it when he introduced me to the topic: “transmission is for amateurs, and reflection is for professionals”.

4.2.3 Weak and strong measurement

Note that in Fig. 4.3, we represent the states of the qubit as blobs of a certain area, rather than dots. This area represents the inherent uncertainty in the values of I and Q , as the traveling coherent state is not an eigenstate of the field components. If we were to histogram many measurements of the outgoing field for a given coherent state, they would not all have the same I and Q values but have a Gaussian spread around the mean value we discussed previously. In our units of $\sqrt{\text{photon}}$, the standard deviation for this ideal measurement is exactly $\sigma_0 = \frac{1}{2}$ for each quadrature (this is directly related to the $\hbar/2$ value in the Heisenberg uncertainty principle). Of course, our measurement is never ideal, and so this standard deviation is greater. Generally we can express the standard deviation in our units as⁴ $\sigma = \frac{1}{2\sqrt{\eta}}$ when η is our measurement efficiency [Hatridge *et al.*, 2013]. We can then define the measurement strength, or the signal-to-noise ratio for a single measurement as:

$$\frac{Q_g - Q_e}{2\sigma} = 2\sqrt{n_{\text{meas}}\eta} \sin \theta, \quad (4.7)$$

where θ is either θ_r or θ_t . We define a measurement to be weak if $\frac{Q_g - Q_e}{2\sigma} \ll 1$, and strong if $\frac{Q_g - Q_e}{2\sigma} \gg 1$.

Dispersive readout has the important advantage of being a quantum non-demolition (QND) measurement [Braginsky *et al.*, 1980]. This means that the measured operator σ_z commutes with the Hamiltonian in Eq. 3.8, and thus the eigenstates can be repeatedly measured without being destroyed. Superpositions such as $|g\rangle + |e\rangle$ are projected towards one of the eigenstates, and thus phase information is lost (this is precisely the measurement-induced dephasing which was discussed in Section 3.3.5). This measurement back-action dephases the qubit more with increasing

⁴Often in our experiments, we use a Josephson Parametric Converter (JPC) to amplify our readout. As it is a phase-preserving amplifier, it adds an additional half a photon of noise to our measurement, which we do not count towards our measurement inefficiency. Thus, in this case, we represent the standard deviation as $\sigma = \frac{1}{\sqrt{2\eta}}$. For more details, see part 2 of the supplementary material in Ref. Hatridge *et al.* [2013].

measurement strength. A full description of the back-action of the dispersive readout for varying measurement strengths is given in Ref. Hatridge *et al.* [2013].

In a strong measurement, the state of the qubit is completely projected to one of its eigenstates. From our derivation it would seem that you can reach this regime by simply increasing the measurement time T , but this time is limited by the coherence time of the effect we are interested in measuring. Reaching this regime for measurement times well below the qubit coherence time was made possible by the use of quantum-limited amplifiers [Castellanos-Beltran *et al.*, 2008, Bergeal *et al.*, 2010, Hatridge *et al.*, 2011]. This is a very large and important field within superconducting quantum circuits, and it is not covered in this thesis. See the theses by Rajamani Vijay [Vijay, 2008], Flavius Schackert [Schackert, 2013] and Katrina Sliwa [Sliwa, 2016] for more details.

In a strong QND measurement we expect to initially project the qubit onto one of its eigenstates, and the following repeated measurements should return the same eigenstate. This does not seem like a very interesting measurement in this case, but decay processes affect the qubit and sometimes cause it to jump between eigenstates⁵. This effect is known as **quantum jumps** [Nagourney *et al.*, 1986, Sauter *et al.*, 1986, Bergquist *et al.*, 1986, Vijay *et al.*, 2011]. This can be seen as the real-time measurement that is averaged to produce a qubit lifetime (T_1) measurement of the qubit. We can extract the qubit T_1 from the mean time between jumps, but we also have access to the qubit temperature from the ratio of times it spends in each of the states $|g\rangle$ and $|e\rangle$, and the average jump rate between them. Furthermore, the jumps give us access to the behavior of qubit decay in real-time, and thus allow us to study the dynamics of the processes which underlie qubit decay [Vool *et al.*, 2014].

⁵Note that this process is related to the quantum Zeno effect [Misra and Sudarshan, 1977, Gambetta *et al.*, 2008], in which a measurement of the qubit is competing with a coherent process between its states, such as a Rabi drive. The behavior of the system then depends on the relative strength of the interaction and measurement rate. For a strong interaction, we are unable to measure the state of the qubit as it quickly oscillates between the eigenstates. For a strong measurement, the qubit is constantly projected and the coherent process is “Zenoed out” and does not contribute other than to cause occasional quantum jumps. This would suggest that the decay rate in our case acts like a very weak coherent process, but then we expect to see the rate of jumps decrease as the measurement gets stronger. We have never been able to cancel the effect of dissipation this way, and the jump rate is usually constant with measurement rate (It sometimes increases for stronger measurements due to an effect we nicknamed “ T_1 vs. \bar{n} ” [Boissonneault *et al.*, 2009, Slichter *et al.*, 2012]). A better model for the behavior of jumps is statistical. Most of the time the system is not interacting with the environment and nothing competes with the measurement. Sometimes, on a timescale given by T_1 , the system interacts with an external DOF much faster than the measurement rate, and as a result we measure quantum jumps due to a process we cannot control. Another way to describe this is to treat the environment as a high-bandwidth coherent system, which cannot be Zenoed out until the measurement rate exceeds its bandwidth

In Chapter 6 we present a novel method to observe the quantum jumps of an effective qubit. These quantum jumps allow us to study the real-time dynamics of qubit decoherence (T_2), as opposed to qubit decay (T_1).

Chapter 5

Controlling the radiation selection rules of superconducting circuits

Selection rules in atomic systems are the rules governing which transitions of the atom are accessible by a certain external drive, and which are forbidden. They are a central hallmark of atomic physics, and one of the main reasons for the variety of quantum systems that can be embodied using the various atoms. The states of an atomic system can have various symmetries, such as spin, angular momentum, rotational, and vibrational symmetries etc. Each symmetry limits the transitions between levels, and hence imposes selection rules .

Selection rules play a crucial role in the physics of atomic coherent quantum systems. Energy states which are connected by a forbidden transition tend to have long coherence times between them, as the environment is also forbidden from interacting with the transition. These are then useful to encode quantum information, while all manipulation and measurement are done through the allowed transitions. These techniques are actively used in qubits based on ion-traps [Leibfried *et al.*, 2003], and are especially important to the field of atomic clocks [Ludlow *et al.*, 2015].

For superconducting artificial atoms, the symmetries limiting their transitions are currently much simpler than those of atomic systems, due to their dependence on a relatively small number of DOF. Further study of our selection rules and how they can be manipulated is crucial for engineering a larger variety of superconducting atoms. The ability to engineer selection rules will

potentially allow us to realize all the quantum systems accessible using atomic implementations, and more.

In this Chapter, we discuss the selection rules for superconducting artificial atoms, and how they can be manipulated to create a larger variety of effective quantum systems. We begin with a description of the allowed and forbidden transition for the different superconducting systems, and the parity symmetry which governs them. We then present a new coupling element, known as the SNAIL, which allows us to break the selection rule, while still maintaining the symmetry of the artificial atom. We use this element to drive forbidden transitions in the fluxonium qubit, and implement a Λ -system at the fluxonium sweet spot. We present the ability to control our Λ -system through Raman processes, implement cooling via spontaneous Raman scattering, and coherent oscillations via stimulated Raman transitions.

5.1 Allowed and forbidden transitions

Consider our two energy eigenstates $|a\rangle$ and $|b\rangle$ in a Hilbert space \mathcal{H} , and a transition operator μ of our Hilbert space \mathcal{H} , which couples to an environment operator. A selection rule prevents the transitions between $|a\rangle$ and $|b\rangle$ if:

$$\langle a|\mu|b\rangle = 0 \tag{5.1}$$

This selection rule is usually associated with a certain symmetry of the Hamiltonian. The most common selection rules are associated with angular momentum. If the states $|a\rangle$ and $|b\rangle$ are eigenstates of the total angular momentum, the conservation of angular momentum imposes selection rules on the transition, depending on the operator μ . For example, if μ corresponds to an excitation due to a single photon (with spin 1), a transition between a state of angular momentum $J = 0$ to another state of $J = 0$ is forbidden. This is the cause of the forbidden transition between 1S_0 and 3P_0 in group 13 singly-charged ions, a long lived transition which is at the heart of many atomic clocks [Ludlow *et al.*, 2015]

For superconducting artificial atoms, we can analyze selection rules as an extension of those of a harmonic oscillator. For a harmonic oscillator, the drive operator which generates transitions

between energy eigenstates (see Section 3.3.2), $(\mathbf{a} + \mathbf{a}^\dagger)$, is a combination of creation and annihilation operators and can thus only cause a transition between two neighboring energy eigenstates, such as $|n\rangle$ and $|n+1\rangle$. Transitions between non-neighboring states are thus always multi-photon transitions mediated by the levels in between.

For non-linear systems, this rule is no longer true. As discussed previously, the drive operator should not be interpreted as a creation and annihilation operator for the non-linear system, which can be quite significantly different from its linear part. However, some limited symmetry can still remain, which leads to selection rules. Consider the important case in which the Hamiltonian of our single-mode non-linear system contains only even terms (compare to the general case in Eq. 3.1), i.e is of the form:

$$\mathbf{H} = \omega_0 \mathbf{a}^\dagger \mathbf{a} + d_4 (\mathbf{a} + \mathbf{a}^\dagger)^4 + d_6 (\mathbf{a} + \mathbf{a}^\dagger)^6 + \dots \quad (5.2)$$

where ω_0 is the resonance frequency of the linear mode and d_n are the nonlinear coefficients such that $d_{2n+1} = 0$ for every $n \in \mathbb{N}$. We can express this system in the basis of the linear system eigenstates $\{|n\rangle\}$. It is easy to see that this Hamiltonian commutes with the parity operator $\mathbf{P} = \sum_{n=0}^{\infty} (-1)^n |n\rangle\langle n|$ and thus its (non-degenerate) eigenstates are also eigenstates of parity. Thus the eigenstates of the full non-linear Hamiltonian are combinations of either only-even or only-odd eigenstates of the linear system. As the drive operator is an odd operator (it anti-commutes with the parity operator \mathbf{P}), it can only cause transitions between states of different parity. This is analogous to the Laporte (orbital inversion symmetry) selection rule for transitions between atomic orbitals [Laporte and Meggers, 1925, Harris and Bertolucci, 1978].

This selection rule has significant consequences on the artificial atoms we can build. In all the common superconducting artificial atoms, the two lowest eigenstates of the Hamiltonian, $|g\rangle$ and $|e\rangle$, have opposite parities and thus we can perform operations between them. However, every higher excited state $|m\rangle$ has a distinct parity. Thus, if $\langle g | (\mathbf{a} + \mathbf{a}^\dagger) | m \rangle \neq 0$ then definitely $\langle e | (\mathbf{a} + \mathbf{a}^\dagger) | m \rangle = 0$ and vice versa. This property prevents us from constructing Λ -type artificial atoms (see Fig. 1.1c) using our lowest energy eigenstates.

This symmetry can be broken by introducing an odd term in the Hamiltonian. Physically it is achieved by applying an external offset, for example a charge offset for the Cooper pair box (see Fig. 2.4a) or a flux offset for the flux qubit or fluxonium (see Fig. 2.4c,d). This additional offset breaks the symmetry of the system, and transitions between all energy levels become allowed. This, however, comes at the price of lower coherence times. The frequency of the $|g\rangle \leftrightarrow |e\rangle$ transition depends on the value of the offset and so the Cooper pair box becomes sensitive to charge noise and the flux qubits become sensitive to flux noise. This dependence is minimized in the “sweet spots”, where the first derivative of the frequency w.r.t. the offset vanishes [Ithier *et al.*, 2005], but those are exactly the offset values for which the symmetry exists and the selection rules stand. For example, the eigenstates of the fluxonium are shown in Fig. 2.5 for different values of the external flux. At $\Phi_{\text{ext}} = 0$ and 0.5 , which are the fluxonium “sweet spots”, the eigenstates have distinct opposite parities and the selection rules apply. At $\Phi_{\text{ext}} = 0.25$ the wavefunctions do not have a distinct parity and all transitions are allowed, but at the cost of decreased coherence times. For a detailed study of selection rules in the flux qubit, see Ref. Liu *et al.* [2005] and in the fluxonium artificial atom, see Ref. Manucharyan [2011].

This treatment can be extended to multi-mode systems. For example, we can study a non-linear system coupled to a linear system such as the JC Hamiltonian (Eq. 3.5). In this case, in addition to the Hamiltonians of the individual systems, there is a coupling term which can be expressed in the form $\propto \phi_q \phi_r$ where ϕ_q is the flux of the non-linear system, or qubit, and ϕ_r is the flux of the linear resonator. With this term, the individual parity is no longer conserved, but the total parity $P = \sum_{n_r, n_q=0}^{\infty} (-1)^{n_r+n_q} |\mathbf{n}_r\rangle |\mathbf{n}_q\rangle \langle \mathbf{n}_q| \langle \mathbf{n}_r|$ is conserved if the non-linear system contains only even terms. Thus, transitions such as $|g, 0\rangle \leftrightarrow |e, 1\rangle$ and $|e, 0\rangle \leftrightarrow |g, 1\rangle$ are forbidden by selection rules at the symmetry point of the non-linear system. Fig. 5.1 shows the selection rules for a qubit-resonator system. Further details in the JC formalism can be found in Appendix E of Ref. Blais *et al.* [2007] and for flux qubits in Refs. Chiorescu *et al.* [2004], Liu *et al.* [2006].

These forbidden transitions can also be driven with two photons. For example, the transition $|g\rangle \leftrightarrow |f\rangle$ can be accessed by applying two drives: one at a frequency $\omega_{ge} + \Delta$ and another at $\omega_{ef} - \Delta$ where ω_{ge} and ω_{ef} are the frequency differences between the $|g\rangle, |e\rangle$ and $|e\rangle, |f\rangle$ states

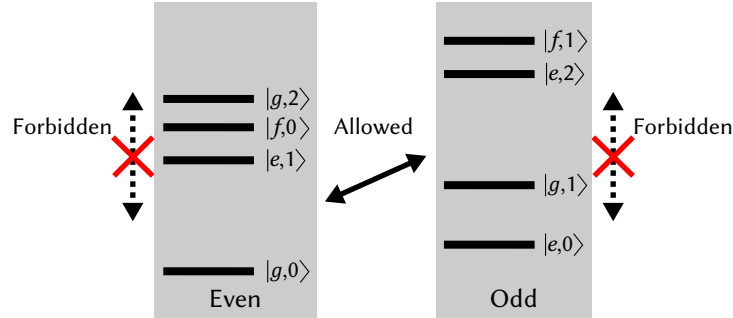


Figure 5.1: The selection rules for a non-linear system that is linearly coupled to a linear oscillator. If the non-linearity contains only even terms (see text), there is a selection rule which forbids transitions between two states with the same parity in the number of excitations. In the sketch, we divide the levels of our system to two sets with even and odd total parities. Using a linear drive, we are only able to excite transitions between the two sets, never within each of the sets.

respectively, and Δ is a given detuning. This is a Raman transition [Steck, 2007] through the $|e\rangle$ state, which is accessed virtually. A special case of this transition is the two-photon transition, in which we apply only one drive at half of the frequency difference and use two photons from the same drive to drive both the $|g\rangle \leftrightarrow |e\rangle$ and $|e\rangle \leftrightarrow |f\rangle$ transitions. In this case $\Delta = K/2$ where K is the Kerr non-linearity of the qubit.

Two-photon transitions are also used in the two-mode case to drive transitions such as $|g, 0\rangle \leftrightarrow |e, 1\rangle$ [Wallraff *et al.*, 2007, Novikov *et al.*, 2016]. In this case the virtual transition is done both through the $|g, 1\rangle$ and the $|e, 0\rangle$ states¹.

To conclude, superconducting artificial atoms at their sweet-spots have a selection rule which prevents transitions between states with equal total parity in the harmonic oscillator basis. This significantly limits the variety of artificial atoms we can construct. This can be overcome by moving off of the sweet-spots, at the cost of a decrease in qubit coherence. It can also be overcome by using a two-photon process, at the cost of a more complicated driving scheme, as well as requiring strong coupling to an intermediate level - which may also limit qubit coherence. In the following section we present a third option, which allows us to drive a forbidden transition while maintain-

¹There is a small subtlety here. If the qubit and resonator modes are completely decoupled, we certainly have no way to entangle the two systems by applying a drive on each of the modes. Since $|g, 0\rangle \leftrightarrow |e, 1\rangle$ is an entangling transition, it must vanish, and indeed the virtual transitions through the $|g, 1\rangle$ and the $|e, 0\rangle$ states cancel each other out. If the modes are coupled, we have an additional dispersive shift (χ) of the cavity mode depending on the state of the qubit. This shift breaks the cancellation and allow a virtual two-photon transition from $|g, 0\rangle$ to $|e, 1\rangle$.

ning the qubit at the sweet-spot and using only a single photon. We do this by implementing a non-linear drive on our system.

Before we continue, let us discuss two additional side notes on selection rules. The first involves an additional approximate selection rule in flux-based artificial atoms off of their sweet spots. As their eigenstates can live in different potential wells (see Fig. 2.5b), the overlap between the wavefunctions decreases exponentially with the distance between the wells compared to the well size. This can decrease the matrix element $\langle g|\phi|e\rangle$ significantly. This selection rule was studied for the fluxonium artificial atom in a recent paper given in Ref. Lin *et al.* [2017]. While they are still able to drive the $|g\rangle \leftrightarrow |e\rangle$ transition directly, the decrease in the matrix element leads to a $\times 100$ increase in the qubit lifetime. However, as the fluxonium is away from its sweet spot, its coherence time is still limited. This approximate selection rule is a very promising idea and is related to the notion of inherently protected superconducting qubits [Brooks *et al.*, 2013, Douçot and Ioffe, 2012, Bell *et al.*, 2014].

As a second side note, given our selection rule it seems there is another natural way to produce a perfect Λ system. If we have a Hamiltonian in which the two lowest eigenstates $|g\rangle$ and $|e\rangle$ have the same parity, these states form a Λ -system with any higher excited state of the opposite parity, and there is no way to directly transition between $|g\rangle$ and $|e\rangle$. Ref. Xu *et al.* [2016] shows a similar idea in which the $|g\rangle$ and $|f\rangle$ states of a transmon qubit are used to form a Λ system. While they indeed have the correct parity structure, these are not the lowest energy eigenstates and the $|f\rangle$ state will eventually decay outside of the encoded Λ -system.

Obtaining a Hamiltonian in which the two lowest eigenstates are of the same parity seems like a very important goal. A possible implementation of this is the $\cos 2\varphi$ element [Douçot and Vidal, 2002] which only allows tunneling between pairs of Cooper-pairs. The two lowest eigenstates of a qubit based on this element have opposite parity in Cooper-pair number, but equal parity in the harmonic oscillator basis as both their wavefunctions are symmetric. This kind of qubit has been originally studied by Rutgers [Bell *et al.*, 2014], and a fluxonium-like implementation is currently being studied at Yale [Smith *et al.*, 2017].

5.2 SNAIL

The selection rule which forbids transitions between states of equal parity is a result of the drive operator being odd. To drive these forbidden transitions, we require an operator of the form $(\mathbf{a} + \mathbf{a}^\dagger)^2$. As this operator is even (commutes with an even Hamiltonian), it enables transitions between states of the same parity (but not between states of different parity). The original (linear) drive operator was a result of linear coupling between the qubit and the resonator, and thus, to create the desired operator, we would require a non-linear coupling element with third-order non-linearity.

This project started with the goal of breaking selection rules in the 3D fluxonium architecture, in which the fluxonium qubit is coupled to an on-chip resonator by a shared linear inductance². We thus wanted to design a third-order non-linear inductance to couple the fluxonium and the resonator, and drive forbidden transitions through it.

The device we came up with is named the Superconducting Non-linear Asymmetric Inductive eLement, or SNAIL - a pun on other mollusk-inspired circuits such as the SQUID [Zimmerman and Silver, 1966, Clarke and Braginski, 2006] and the SLUG [Clarke, 1966, Hover *et al.*, 2012]. A sketch of the SNAIL circuit is shown in Fig. 5.2a. The SNAIL is a superconducting loop which consists of n large Josephson junctions with Josephson energy E_J , shunted by a single smaller Josephson junction with Josephson energy αE_J . An external flux Φ_{ext}^S is threaded through the SNAIL loop.

We can express the potential (inductive) energy of the SNAIL as:

$$U_{\text{SNAIL}}(\varphi) = -\alpha E_J \cos \varphi - n E_J \cos \left(\frac{\Phi_{\text{ext}}^S / \phi_0 - \varphi}{n} \right), \quad (5.3)$$

where φ is the superconducting phase across the small junction. Note that we have eliminated the dynamics of the modes within the n -junction array, and consider the circuit as a single DOF with equal phases across the array junctions. This is valid when $E_J \gg E_C$ for every array junction, and $C_0 \ll C_J/n^2$ where C_0 is the ground capacitance of the islands between the junctions and C_J is the

²Practically, this inductance is not quite linear as it is made up of an array of Josephson junctions. However, since the Josephson potential is even (a cosine), the additional non-linear terms still cannot drive the forbidden transitions.

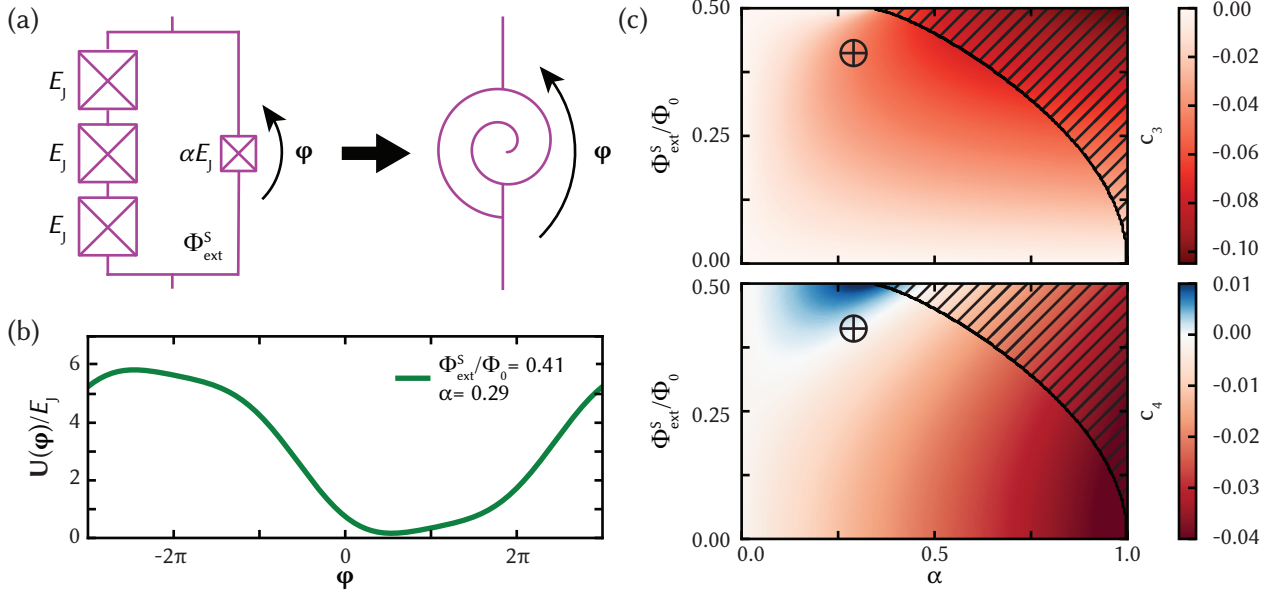


Figure 5.2: (a) Circuit for the Superconducting Nonlinear Asymmetric Inductive eLement (SNAIL) reduced to one degree of freedom φ . A loop made of three large junctions (with tunneling energy E_J) in parallel with one smaller junction (tunneling energy αE_J) is threaded with an external DC flux Φ_{ext}^S . (b) An example SNAIL potential for $\alpha = 0.29$ and $\Phi_{\text{ext}}^S/\Phi_0 = 0.41$ that includes third-order nonlinearity ($c_3 \neq 0$) without fourth-order nonlinearity ($c_4 = 0$). (c) Color maps of the $(\alpha, \Phi_{\text{ext}}^S)$ parameter space for the third-order (top) and fourth-order (bottom) nonlinear terms. Notice the white region in the bottom panel, corresponding to points with $c_3 \neq 0$ but $c_4 = 0$. The black-hatched regions in (c) correspond to double well behavior. The crosses in (c) mark the set of parameters chosen for (b).

Josephson capacitance of each junction [Masluk *et al.*, 2012]. Thus, the frequencies corresponding to the array modes are high, and we can neglect them within our treatment.

Note that our circuit is basically identical to that of the flux qubit (see Section 2.4.3). However, our operation point is completely different. The flux qubit is operated around $0.5\Phi_0$, and the ratio of junction areas is usually $\alpha \approx 0.8$. This creates the double-well potential in which the flux qubit levels reside. We would like to completely avoid the double-well area, and operate the SNAIL in a regime which resembles a parabolic well, but with an asymmetry around the minimum of the well - this asymmetry is precisely the third-order non-linearity we are looking for. Fig. 5.2b shows one period of the SNAIL potential for a particular choice of Φ_{ext}^S and α , and for $n = 3$. The asymmetry around the minimum is visible.

To expand Eq. 5.3 as a non-linear inductor, we must first find the minimum φ_{min} of the poten-

tial. This minimum depends on $\Phi_{\text{ext}}^{\text{S}}$ and α , and can be numerically obtained for each of those. Then we can expand the SNAIL potential around the minimum, using the new coordinate $\tilde{\varphi} = \varphi - \varphi_{\text{min}}$. We express the Taylor expansion of the potential as:

$$U_{\text{SNAIL}}(\tilde{\varphi})/E_{\text{J}} = c_2\tilde{\varphi}^2 + c_3\tilde{\varphi}^3 + c_4\tilde{\varphi}^4 + \dots, \quad (5.4)$$

where c_m is the coefficient of the m -th order in the expansion³. c_2 is related to the linear inductance of the SNAIL as $L_{\text{S}} = \frac{\phi_0^2}{2c_2E_{\text{J}}}$. These coefficients also depend on $\Phi_{\text{ext}}^{\text{S}}$, α , and n , and can be obtained numerically. The SNAIL can thus be viewed as a new non-linear element with the potential in Eq. 5.4, and in future circuits we represent the SNAIL using a snail symbol, as shown in Fig. 5.2a.

The case $n = 1$ corresponds to the asymmetric SQUID. In this case, the periodicity of the two cos terms in Eq. 5.3 is identical and so their sum is simply an offset cos term. Thus in this case, $c_3 = 0$ regardless of the other parameters. For $n \geq 1$, the competition between the different periodicities of the cos function gives rise to an asymmetry for certain fluxes and junction size ratios. The case $n \gg 1$ corresponds to the fluxonium circuit (see Section 2.4.4), where we know the asymmetry exists. In the experimental implementations of the SNAIL shown in this thesis, we use $n = 3$. This is done mostly for fabrication constraints (see the following section for more details).

In Fig. 5.2c, we plot the third-order non-linearity (c_3) and the fourth-order non-linearity (c_4) vs. $\Phi_{\text{ext}}^{\text{S}}$ and α in the top and bottom plots respectively, for $n = 3$. The dashed area corresponds to values for which the potential has multiple wells, and thus the expansion is more problematic and our circuit may show hysteretic behavior. This is the regime in which the flux qubit operates, and we avoid it for the SNAIL.

Notice that the SNAIL has the unique feature that its c_4 value changes sign for different values of $\Phi_{\text{ext}}^{\text{S}}$ and α . Thus, there is a particular selection of values (marked as a cross in Fig. 5.2c) for which $c_3 \neq 0$ but $c_4 = 0$. The potential in Fig. 5.2b is plotted for this value.

The third-order non-linearity of SNAIL allows it to facilitate three-wave mixing between dif-

³ These coefficients are very related to the d_m coefficients in Eq. 3.1, as those were derived from a generic non-linear inductor we assumed in our circuit. They are identical up to units, as $d_m = c_m \varphi_{\text{ZPF}}^m E_{\text{J}}$

ferent modes. This has attracted interest in the SNAIL as a dipole 3-wave mixing element, with potential use for amplification and mode conversion. The cancellation of c_4 is of special interest in this case, as it may allow us to amplify signals and drive transitions between modes without the Stark shift caused by the Kerr non-linearity⁴.

We have implemented a parametric amplifier based on the SNAIL, by integrating four SNAILs in a loop inspired by the Josephson ring modulator (JRM) design for parametric amplification [Bergeal *et al.*, 2010]. The details of this experiment are beyond the scope of this thesis. To summarize, we were able to observe phase-preserving amplification, facilitated by the third-order non-linearity of the SNAIL and not the loop of the JRM, which was removed. This SNAIL amplifier showed performance comparable to commercial JRM-based quantum-limited amplifiers. The details of this experiment are available in Ref. Frattini *et al.* [2017].

The SNAIL has also been independently discovered by A. Zorin [Zorin, 2016] for its use as part of a three-wave mixing traveling-wave parametric amplifier (TWPA). Such a TWPA was implemented in a recent experiment given in Ref. Zorin *et al.* [2017].

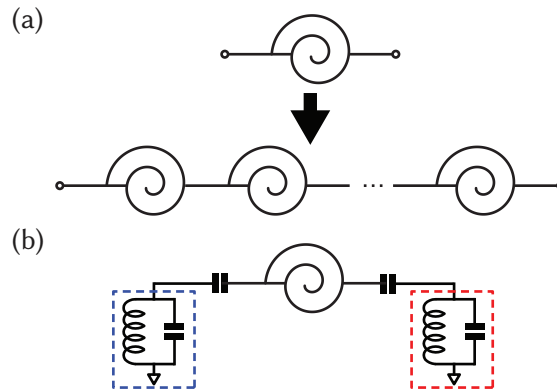


Figure 5.3: (a) The dipole nature of the SNAIL allows for arraying of three-wave mixing elements. This can be construct an amplifier with increased dynamic range or bandwidth. (b) An example of a circuit in which the SNAIL is used as a tunable coupling device between two modes, represented by red and blue boxes.

An important advantage of the dipole nature of the SNAIL is the ability to combine many

⁴Recall the discussion at the beginning of Section 3.1. $c_4 = 0$ does not quite imply that the Kerr non-linearity $K = 0$. Second-order corrections from the c_3 can add to the Kerr and should be included in the calculation. However, the varying sign of the c_4 term should still allow us to find a regime in which these effects cancel to produce $K = 0$. The experimental study of the Kerr non-linearity of the SNAIL vs. $\Phi_{\text{ext}}^{\text{S}}$ and α is currently ongoing.

SNAILs into an array. This is an important technique for improving the the performance of parametric amplifiers, and is commonly used in four-wave mixing amplifiers [Castellanos-Beltran *et al.*, 2008]. Such an arraying for the SNAIL, as is shown in Fig. 5.3a, can lead to similar improvements in three-wave mixing amplifiers.

Additionally, the SNAIL can be used to facilitate tunable coupling between different modes. Consider two resonators which are coupled by a SNAIL, as shown in Fig. 5.3b. The SNAIL is the non-linearity in this circuit, and thus provides the three-wave mixing between the linear resonator modes (see the non-linear potential term in Eq. 2.38). By applying a single drive at the difference of the mode resonance frequencies, the three wave mixing term and the drive term can combine to create the effective beam-splitter Hamiltonian:

$$\mathbf{H}_{\text{BS}} = g_{\text{eff}}(t) \left(\mathbf{a}_b^\dagger \mathbf{a}_r + \mathbf{a}_r^\dagger \mathbf{a}_b \right), \quad (5.5)$$

where \mathbf{a}_r and \mathbf{a}_b are the annihilation operators of the red and blue resonators respectively, and g_{eff} is the effective coupling which is proportional to the drive amplitude. This Hamiltonian leads to a coherent conversion between the populations of the two resonators. Similarly, by driving at the sum of the two frequencies, we can create an effective two-mode squeezing Hamiltonian:

$$\mathbf{H}_{2\text{MS}} = G_{\text{eff}}(t) \left(\mathbf{a}_b^\dagger \mathbf{a}_r^\dagger + \mathbf{a}_r \mathbf{a}_b \right), \quad (5.6)$$

which is actually the Hamiltonian term responsible for the amplification of the JRM and the SNAIL amplifier. However, it can also be used as another form of coupling between two modes.

Such tunable couplers are becoming more important for the control of superconducting circuits. For example, recent experiments at Yale utilize tunable coupling between a long-lived cavity mode and a fast cavity mode. This allows for the coherent conversion between long-lived stationary cavity states and traveling waves [Pfaff *et al.*, 2017], and can potentially allow us to communicate between long-lived cavity nodes in a network. Currently, this is done using the four-wave mixing property of a single Josephson junction with the addition of two pumps. Using the SNAIL, it would be possible to perform this process more simply with a single pump, and potentially

without the Stark shifts due to the Kerr non-linearity.

5.3 SNAIL-fluxonium

We now present the 3D fluxonium qubit which enables us to drive forbidden transitions at the fluxonium sweet spot. This design integrates the SNAIL into the 3D fluxonium architecture as an inductance shared between the fluxonium and its antenna resonator.

5.3.1 Theoretical model

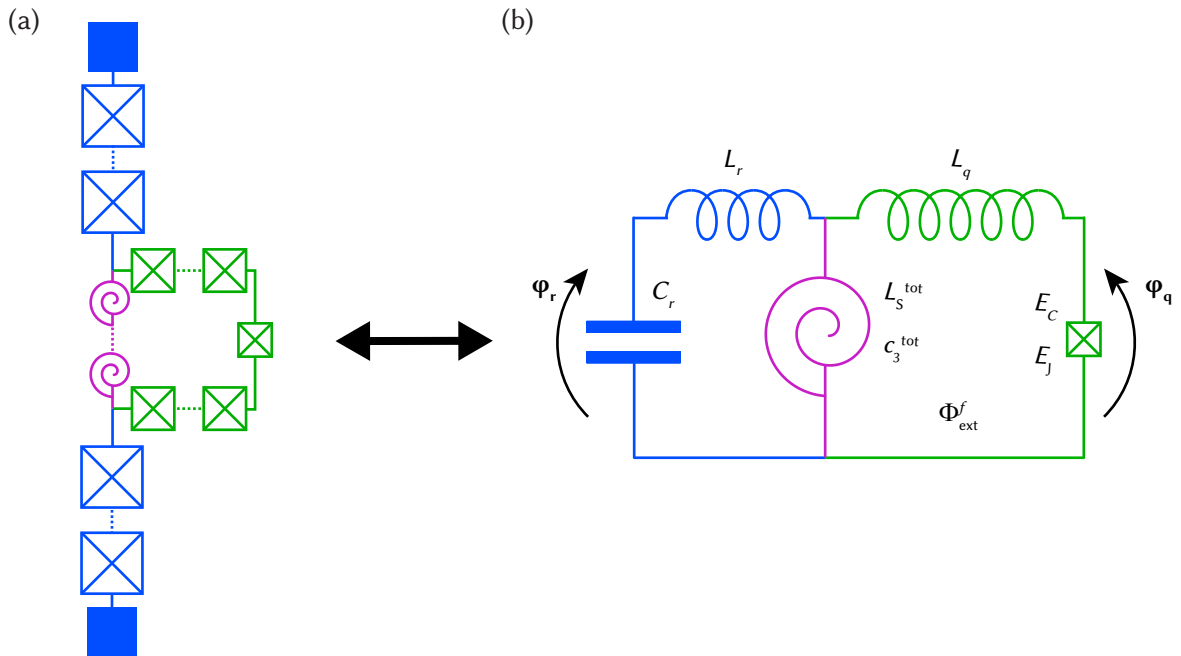


Figure 5.4: (a) The fluxonium artificial atom (green) is made up of a small junction shunted by a large inductance, itself made of an array of larger Josephson junctions. Some of this inductance is shared with the resonator (blue). In this design, the shared elements (magenta) are taken to be SNAILs, which allows us to break selection rules at the fluxonium sweet spot. (b) The equivalent circuit diagram. This circuit has two DOF, and we express the Hamiltonian as a function of φ_r - the flux across the resonator capacitor and φ_q , the flux across the fluxonium small junction.

Fig. 5.4a shows a sketch of the device. The fluxonium artificial atom, shown in green, is made up of a small junction shunted by an array of larger junctions. Some of the inductance of the fluxonium

array is made up of N SNAILs (magenta), which are a shared inductance between the fluxonium and an antenna resonator (blue). The resonator is made up of capacitor pads, and junctions which form its own unshared inductance.

To understand the behavior of the circuit quantitatively, let us simplify it into an effective circuit given in Fig. 5.4b. The fluxonium (green) is now represented by a small junction with Josephson energy E_J and capacitive energy E_C , shunted by a linear inductance L_q . An external flux Φ_{ext}^f is threaded through the fluxonium loop. The resonator (blue) is represented as an LC oscillator with capacitance C_r and unshared inductance L_r . The N SNAIL array which couples the two systems is reduced to a single effective SNAIL (magenta). We represent the SNAIL as having only second-order and third-order terms.

We can label the superconducting phase across the SNAIL array as φ_S , and assume it is divided equally across all N SNAILs in the array (neglecting higher frequency modes as we have done previously). Thus, we can calculate the coefficients of the total SNAIL array from those of the SNAIL.

$$c_2^{\text{tot}} \varphi_S^2 = N c_2 \left(\frac{\varphi_S}{N} \right)^2, \quad (5.7)$$

where c_2 is the second-order coefficient of a single SNAIL in the array, and c_2^{tot} is the second-order coefficient of the whole array. Thus, $c_2^{\text{tot}} = c_2/N$ or $L_S^{\text{tot}} = N L_S$. Linear inductances in series are simply added, as expected. A similar calculation shows that $c_3^{\text{tot}} = \frac{c_3}{N^2}$, and so the third-order non-linearity is suppressed by an additional factor of N . Higher order non-linearities are similarly suppressed by higher and higher factors, making the low-order non-linearity assumption better⁵.

The circuit in Fig. 5.4b has only two true DOF and we choose to use the phase across the Josephson junction φ_q , and the phase across the resonator capacitance φ_r . We can calculate the Hamiltonian by following the steps provided in Chapter 2. A very similar derivation is given in Ref. Smith *et al.* [2016], with a shared linear inductance replacing the SNAIL. The addition of the SNAIL adds a three-wave mixing term to the simple fluxonium-resonator Hamiltonian, of the

⁵This is precisely the benefit of the arraying we discussed in the previous section (see Fig. 5.3a) to improve the performance of amplifiers.

form:

$$\mathbf{H}_{\text{3WM}} = c_3^{\text{tot}} \phi_0^3 \left(\frac{L_r L_S^{\text{tot}}}{L_q (L_r + L_S^{\text{tot}})} \varphi_q + \frac{L_S^{\text{tot}}}{L_r + L_S^{\text{tot}}} \varphi_r \right)^3, \quad (5.8)$$

where we have assumed that $L_q \gg L_r, L_S^{\text{tot}}$. This three-wave mixing Hamiltonian gives rise to several effects through its different mixing terms, but let us focus on two terms of special importance:

$$\mathbf{H}_{|g\rangle-|f\rangle} = 3c_3^{\text{tot}} \phi_0^3 \left(\frac{L_S^{\text{tot}}}{L_q} \right)^2 \frac{L_r^2 L_S^{\text{tot}}}{(L_r + L_S^{\text{tot}})^3} \varphi_r \varphi_q^2 \quad (5.9)$$

$$\mathbf{H}_{|g,0\rangle-|e,1\rangle} = 3c_3^{\text{tot}} \phi_0^3 \frac{L_S^{\text{tot}}}{L_q} \frac{L_r (L_S^{\text{tot}})^2}{(L_r + L_S^{\text{tot}})^3} \varphi_r^2 \varphi_q \quad (5.10)$$

The term in Eq. 5.9 is proportional to the term $\varphi_r \varphi_q^2$. With an additional resonator drive, this gives rise to an even drive term⁶ of the form φ_q^2 which is able to drive the fluxonium $|g\rangle \leftrightarrow |f\rangle$ transition at the fluxonium sweet spot as $\langle g | \varphi_q^2 | f \rangle \neq 0$. The term in Eq. 5.10 similarly leads to a drive term of the form $\varphi_q \varphi_r$. This is another even term, but one that allows us to drive the forbidden joint transitions such as $|g, 0\rangle \leftrightarrow |e, 1\rangle$ ⁷.

Eq. 5.10 should remind us of the tunable mode coupling we have discussed in the previous section, and specifically Eqs. 5.5 and 5.6. The even drive created by Eq. 5.10 actually gives rise to both a beam-splitter term, as in Eq. 5.5, which can drive the $|e, 0\rangle \leftrightarrow |g, 1\rangle$ term, and a two-mode squeezing term, as in Eq. 5.6, which can drive the $|g, 0\rangle \leftrightarrow |e, 1\rangle$ transition. Thus, our selection-rule-breaking drive can also be understood as a tunable coupling between modes, such that the parity is preserved.

There are two important things to notice in the coefficients of Eqs. 5.9 and 5.10. First of all, they both depend on L_r in the numerator. L_r is the unshared resonator inductance, and thus one would expect that if the antenna shares more of its inductance, it is more coupled to the fluxonium

⁶We can see this by following the derivation in Section 3.3. Recall that $\varphi_r = \varphi_{\text{ZPF}}^r (\mathbf{a}_r + \mathbf{a}_r^\dagger)$, and we add a drive of the form $\epsilon (\mathbf{a}_r + \mathbf{a}_r^\dagger)$ in the drive frequency rotating frame. By applying the displacement operator, we end up with a drive term of the form $\varphi_{\text{ZPF}}^r \alpha_r \varphi_q^2$ where α_r is the coherent state amplitude in the resonator. A similar transformation takes $\varphi_r^2 \varphi_q \rightarrow 2\varphi_{\text{ZPF}}^r \alpha_r \varphi_r \varphi_q$.

⁷The distinction between φ_q^2 and $\varphi_q \varphi_r$ and the terms they can drive is not absolute, due to the coupling between the resonator and the fluxonium. Both of these drive terms can drive the transitions $|g\rangle \leftrightarrow |f\rangle$ and $|g, 0\rangle \leftrightarrow |e, 1\rangle$ to some extent. However, as the coupling between the resonator and the fluxonium is weak (we are in the dispersive regime), we associate each term with the transitions it couples to more strongly.

and thus the SNAIL is better able to drive the forbidden transitions. This intuition is false, as when $L_r = 0$, the SNAIL element is the entire inductance of the resonator and the phase across it is φ_r . There is still coupling between the two modes, mediated by the L_q inductor, but the SNAIL does not participate in it and thus there is no three-wave mixing for the qubit mode. Thus, a substantial L_r , comparable to L_S^{tot} , is necessary to drive forbidden transitions.

The second thing to notice is that the coefficient in Eq. 5.10 is larger than Eq. 5.9 by a factor of L_q/L_S^{tot} , which is experimentally ≈ 50 . Thus, this coupling scheme is more suited to drive the two-mode forbidden transitions such as $|g, 0\rangle \leftrightarrow |e, 1\rangle$.

It is important to remind again that φ_r and φ_q are **not** the field operators of the resonator and fluxonium modes, but simply convenient bases made up of their linear parts. Especially, φ_q is the field operator of a linear mode very different from the fluxonium qubit. The statements $\langle g|\varphi_q|f\rangle = 0$ and $\langle g|\varphi_q^2|f\rangle \neq 0$ are true due to the selection rules described in Section 5.1, but calculating the value of the matrix element requires a diagonalization of the fluxonium Hamiltonian, and is usually done numerically.

5.3.2 The device

The SNAIL fluxonium was fabricated using aluminum on a sapphire substrate. It was made in a single fabrication step, using the bridge-free fabrication technique (see Section 4.1.1 for more information).

Fig. 5.5a shows a scanning electron microscope (SEM) image of a SNAIL. In the image we see the SNAIL loop, with the upper path passing through three larger junctions, and the lower path passing through a single smaller junction. The ratio between the area of the smaller junction and the larger junctions (and thus their Josephson energies) is $\alpha = 0.4$.

A trick, unique to bridge-free fabrication, was used to make this device. As we have discussed in Section 4.1.1, in this technique we can choose to connect the top layers of adjacent junctions, or the bottom layers. The pattern of the upper path follows the normal array structure: the wire coming from the left connects to the **bottom** layer of the left larger junction, a wire connects the left larger junction's **top** layer to that of the middle larger junction, a wire connects the middle

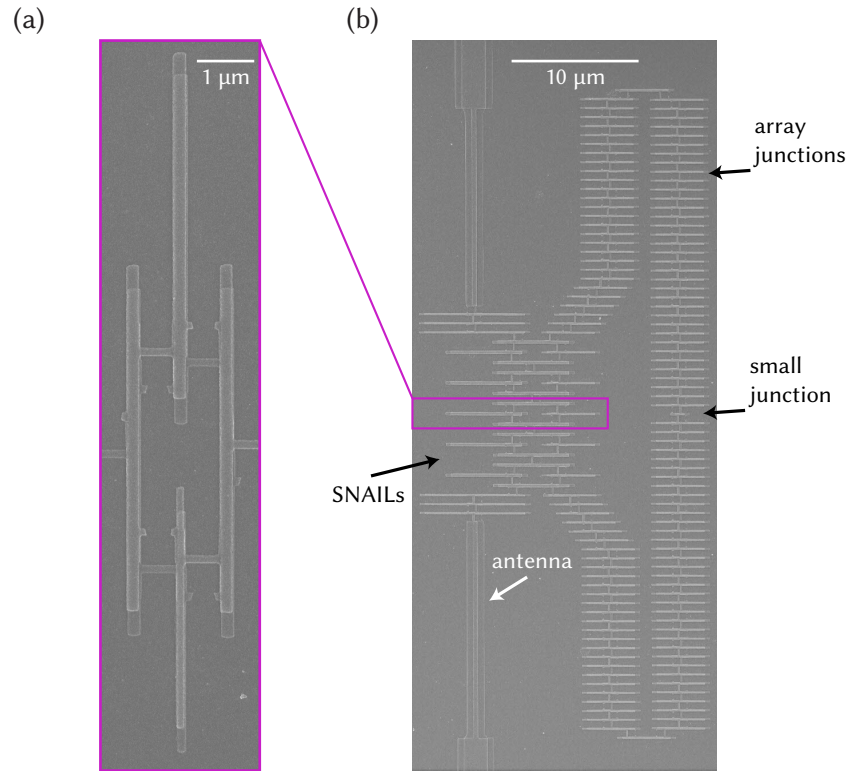


Figure 5.5: (a) an SEM image of a SNAIL made using the bridge-free fabrication technique. The top path of the loop is through three large Josephson junctions, while the bottom one is only through the smaller junction. The larger junctions are not participating in the bottom path as the lines connecting them are attached to the same junction pad. (b) The SNAIL in (a) is embedded as a coupling element between a fluxonium and an antenna resonator. The fluxonium is made of a small junction and 126 array junctions. It is coupled to the antenna using 5 SNAILs. The antenna resonator also has 6 unshared junctions. Note that for a given applied magnetic field, $\Phi_{\text{ext}}^f / \Phi_{\text{ext}}^S = 60 \pm 2$ due to the area difference. This allows us to independently tune both fluxes.

larger junction's **bottom** layer to that of the right larger junction, and a wire connects to the right larger junction's **top** layer and exits on the right. Thus the upper path passes through all three larger junction. On the other hand, the lower path is a bit more tricky: the wire coming from the left connects to the **bottom** layer of the left larger junction, a wire connects the left larger junction's **bottom** layer to that of the smaller junction, a wire connects the smaller junction's **top** layer to that of the right larger junction, and a wire connects to the right larger junction's **top** layer and exits on the right. Thus the lower path only passes through the smaller junction, with the wires connecting to the larger junctions only passing through one of their layers, thus shunting

them. The distinction between the top and bottom layer wires is visible in the SEM image. As the pattern must begin with a bottom layer and end in a top layer (or vice versa) - we must use an odd number of larger junctions in the SNAIL.

The SNAIL is embedded as a coupling element between the fluxonium and its antenna resonator, as is shown in the SEM image in Fig. 5.5b. The fluxonium is made of a small junction, and an array of 126 array junctions. There are also $N = 5$ SNAILs which couple the fluxonium and the resonator. The antenna resonator also has its own unshared inductance, which is made up of 6 unshared junction. The antenna wire, not shown due to scale, has a total length of 1 mm.

Note that the fluxonium loop is significantly larger than that of the SNAIL. The area of the SNAIL loop is $A_S = 6 \pm 0.2 \mu\text{m}^2$ while the area of the fluxonium loop is $A_f = 350 \pm 10 \mu\text{m}^2$. For a given applied magnetic field, the ratio of the fluxes through the fluxonium and SNAIL loops is $\Phi_{\text{ext}}^f / \Phi_{\text{ext}}^S = 60 \pm 2$. This allows us to independently control the flux through each loop, even though we only have global control of the magnetic field. We can first set the the magnetic field to a value such that Φ_{ext}^S is significant and so we have a substantial third-order term (see Fig. 5.2c). Then we can finely tune the magnetic field to find a half-flux sweet spot of the fluxonium qubit, i.e $\Phi_{\text{ext}}^f \bmod \Phi_0 = 0.5$. This fine tuning does not substantially vary the value of Φ_{ext}^S .

From resistance measurements of the different elements in the SNAIL fluxonium we can estimate the different inductances [Ambegaokar and Baratoff, 1963, Nigg *et al.*, 2012]. We estimate that $L_q = 410\text{nH}$, $L_r = 14\text{nH}$, and $L_S^{\text{tot}} = 9\text{nH}$ at zero flux (it increases as flux is threaded through the SNAIL loop). The measured antenna resonator resonance frequency is $\omega_r = 2\pi \times 6.82 \text{ GHz}$, and thus we can estimate $C_r = 24 \text{ fF}$. From a measurement of the small junction resistance and qubit spectroscopy (shown immediately below), we estimate $E_J/h = 8.5 \text{ GHz}$ and $E_C/h = 2.8 \text{ GHz}$.

We cooled the device down using a dilution refrigerator, and characterized the properties of our artificial atom. Fig. 5.6a shows a two-tone spectroscopy of the $|g\rangle \leftrightarrow |e\rangle$ transition of the fluxonium qubit. The phase of a resonant drive reflecting from the antenna resonator is measured (see Section 4.2), while applying a CW tone at a varying frequency. A background has been subtracted from the measurement to account for a change in the resonator frequency with flux. The measurement shown is at the vicinity of $\Phi_{\text{ext}}^f / \Phi_0 = 6.5$, which will eventually be our working

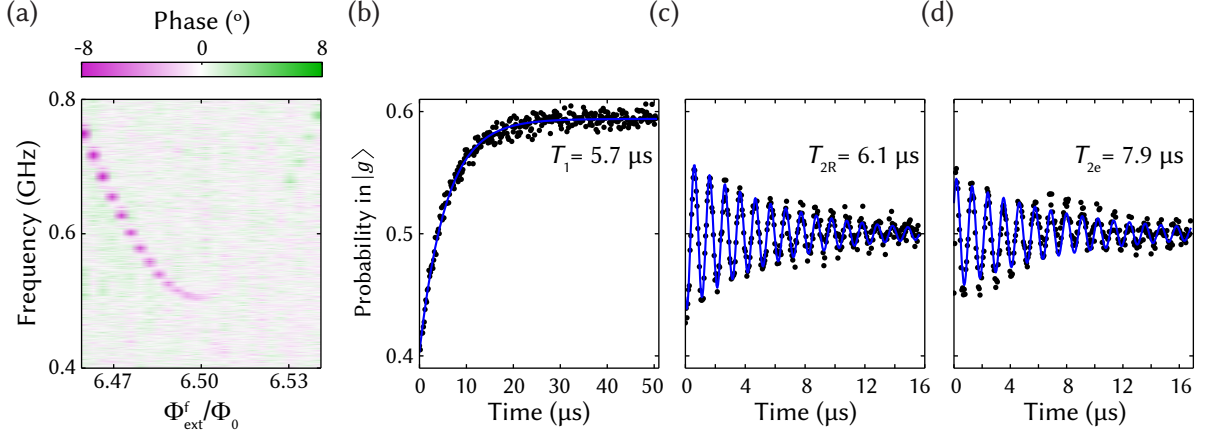


Figure 5.6: (a) Two-tone spectroscopy of the $|g\rangle \leftrightarrow |e\rangle$ transition around $\Phi_{\text{ext}}^f/\Phi_0 = 6.5$. The change in the phase sign corresponds to a change in the dispersive coupling χ between the fluxonium and the resonator. (b) A T_1 measurement of the fluxonium qubit, with an exponential fit (straight line) (c) & (d) Measurements of the Ramsey (T_{2R}) and echo (T_{2e}) decay times respectively.

point, but similar curves have been measured near other half-flux sweet spots of the fluxonium. The fluxonium qubit frequency at its half-flux sweet spot is $\omega_q = 500$ MHz. Notice there is a change in the sign of the resonator response phase at around $\Phi_{\text{ext}}^f/\Phi_0 = 6.52$. This is likely due to a change in the sign of the dispersive shift χ between the fluxonium and the resonator. The dispersive shift of the fluxonium depends on higher level fluxonium-resonator transitions in a subtle way [Smith *et al.*, 2016], and similar transitions have been observed in the fluxonium. Luckily, $\chi \neq 0$ at the fluxonium sweet-spot, and thus we are able to measure the fluxonium transitions.

We measured the coherence times of the fluxonium $|g\rangle \leftrightarrow |e\rangle$ transition at the fluxonium half-flux sweet spots. The measurements at $\Phi_{\text{ext}}^f = 6.5\Phi_0$ are shown in Fig. 5.6b, c, and d. We find the qubit lifetime is $T_1 = 5.7 \mu\text{s}$, the Ramsey decoherence time is $T_{2R} = 5.7 \mu\text{s}$ and the echo decoherence time is $T_{2e} = 7.9 \mu\text{s}$ ⁸. Similar values were observed at $\Phi_{\text{ext}}^f = 0.5\Phi_0$. The y -axis calibration of the qubit population was done using a later measurement, and is discussed in Section 5.3.4.

There is a concern that the addition of the SNAIL can introduce losses to our artificial atom.

⁸The oscillations in Fig.5.6c and d are due to an artificial detuning of 1 MHz made by changing the phase of the second $\pi/2$ pulse in the sequence. All $\pi/2$ pulses were performed on qubit resonance.

The fluxonium is taken at its sweet-spot, but notice that the SNAIL is not in its sweet-spot (this is necessary to obtain the three-wave mixing). Thus, flux noise causes a change in its inductance, and thus in the array inductance of the fluxonium L_q . At half-flux, the fluxonium $|g\rangle \leftrightarrow |e\rangle$ transition depends on the parameters of the small junction⁹ and thus it should theoretically be first-order insensitive to the array inductance.

This has already been partially experimentally validated as the fluxonium in Refs. Pop *et al.* [2014], Vool *et al.* [2014] used SQUIDs as coupling elements, and high coherences were measured. However, these values were only measured at the lowest flux sweet spot $\Phi_{\text{ext}}^f = 0.5\Phi_0$ and not at higher values. Also, the three-wave-mixing nature of the SNAIL could introduce additional losses compared to the SQUID.

In our sample, we measure T_2 values that are consistent with the best 3D fluxonium samples, and a T_1 value well below other waveguide 3D fluxonium samples ($\approx 100 \mu\text{s}$ in Ref. Kou *et al.* [2017]). The low T_1 value could be a result of introducing the SNAIL into the circuit. However, an identical T_1 value was measured at $\Phi_{\text{ext}}^f = 0.5\Phi_0$, where the SNAIL three-wave-mixing term is negligible. While the coherence of the SNAIL fluxonium requires further study, we believe this low T_1 is not introduced by the SNAIL but is due to other noise sources, such as dielectric loss.

These coherences of the SNAIL fluxonium are certainly high enough to observe and control the fluxonium selection rules, and so we proceed to drive the forbidden transitions of the circuit.

5.3.3 Spectroscopy of forbidden transitions

The ratio $\Phi_{\text{ext}}^f/\Phi_{\text{ext}}^S = 60$ allows us to study the effect of the SNAIL on the fluxonium transitions. The fluxonium spectrum is identical at its different sweet-spots, but the flux through the SNAILs varies substantially - leading to a change in the value of the c_3^{tot} coefficient for the SNAIL array. We observe the $|g, 0\rangle \leftrightarrow |e, 1\rangle$ transition which should be stronger due to its larger coefficient (see Eq. 5.10).

Fig. 5.7 shows a two-tone spectroscopy in the vicinity of the $|g, 0\rangle \leftrightarrow |e, 1\rangle$ transition ($\omega_r + \omega_q$)

⁹The fluxonium $|g\rangle \leftrightarrow |e\rangle$ transition energy at half-flux is related to the tunneling rate between the two lowest fluxonium wells, and is proportional to $\propto e^{-\sqrt{8E_J/E_C}}$ [Manucharyan, 2011, Matveev *et al.*, 2002].

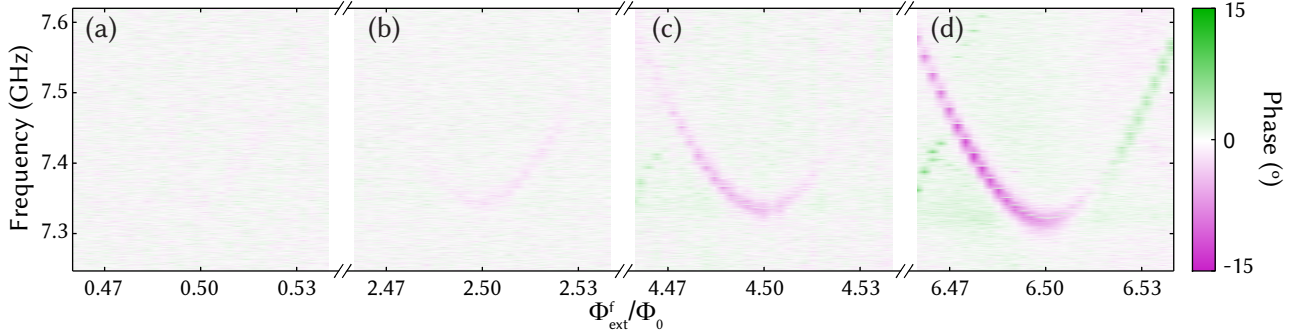


Figure 5.7: (a), (b), (c), and (d) show a two-tone spectroscopy of the $|g, 0\rangle \leftrightarrow |e, 1\rangle$ transition with a SNAIL-fluxonium device around $\Phi_{\text{ext}}^f/\Phi_0 = 0.5, 2.5, 4.5,$ and 6.5 respectively. The different regions are all around half-flux sweet spots of the fluxonium qubit, but the flux through the SNAIL increases. At higher flux values, the SNAIL becomes a significant three-wave-mixing element, which allows us to drive the previously forbidden transitions. The change in the sign of phase observed in (d) is due to a change in the dispersive coupling χ between the fluxonium and the resonator. It is also visible in a direct measurement of the $|g\rangle \leftrightarrow |e\rangle$ transition in Fig. 5.6a.

around four different fluxonium half-flux sweet spots: $\Phi_{\text{ext}}^f/\Phi_0 = 0.5, 2.5, 4.5,$ and 6.5 shown in Fig. 5.7a, b, c, and d respectively. The measurements were done in the same setup and using a tone of the same amplitude, yet they show substantially different responses.

At $\Phi_{\text{ext}}^f/\Phi_0 = 0.5$ (Fig. 5.7a) we see no response at the $|g, 0\rangle \leftrightarrow |e, 1\rangle$ transition, which agrees with a regular fluxonium sample as seen in Ref. Manucharyan [2011]. This is due to the parity selection rule near the fluxonium sweet spot. At half-flux sweet spots with higher flux (Fig. 5.7b, c, and d), the forbidden transition becomes more and more visible. This is due to an increase in the value of the three-wave-mixing coefficient, which we predict to be $E_J \times c_3^{\text{tot}}/h = 8, 40, 70,$ and 100 MHz for $\Phi_{\text{ext}}^f/\Phi_0 = 0.5, 2.5, 4.5,$ and 6.5 respectively. The new non-linear drive allows us to break the selection rule and drive the forbidden transition at the fluxonium sweet spot. While it is difficult to obtain the amplitude of the three-wave-mixing drive from the spectroscopy, in the following chapters we present independent ways to measure this non-linear drive amplitude and compare it to the theoretical prediction.

Notice that the frequency of the $|g, 0\rangle \leftrightarrow |e, 1\rangle$ transition at the fluxonium half-flux decreases slightly as the magnetic flux increases. This is due to a decrease in the resonator frequency, as the linear inductance of the SNAILS increases with flux. Also notice that we see a shift in the sign of

the response in Fig. 5.7d. This is likely due to a change in the fluxonium-resonator dispersive shift χ , as we have already seen in the direct qubit measurement in Fig. 5.6a.

And so we are able to drive a forbidden transition by using non-linear coupling! We now utilize this new ability to create a superconducting Λ -system within the fluxonium artificial atom.

5.3.4 Raman cooling

We operate the fluxonium qubit at $\Phi_{\text{ext}}^f/\Phi_0 = 6.5$, where we have a visible response in spectroscopy for the $|g, 0\rangle \leftrightarrow |e, 1\rangle$ transition. A similar response is visible for the $|e, 0\rangle \leftrightarrow |g, 1\rangle$ transition, which is also accessible through the same non-linear drive term. Using these two transitions, we are able to cool the fluxonium qubit via a Raman process, analogous to spontaneous Raman scattering [Steck, 2007].

Recall that the energy of the $|g\rangle \leftrightarrow |e\rangle$ transition in our fluxonium is $\omega_q = 500$ MHz, which corresponds to a temperature of 24 mK. Thus, even at dilution refrigerator temperatures, the fluxonium has significant excited state population in equilibrium. We label the thermal state of the qubit as: $P_{\text{th}}^g |g\rangle\langle g| + P_{\text{th}}^e |e\rangle\langle e|$ where P_{th}^g is the probability to be in the $|g\rangle$ state, P_{th}^e is the probability to be in the $|e\rangle$ state, and $P_{\text{th}}^g + P_{\text{th}}^e = 1$. As the resonator frequency is $\omega_q = 6.82$ GHz, we assume it is not populated in equilibrium.

Fig. 5.8 shows an experiment to cool the population below the thermal equilibrium temperature, by using Raman processes. The black curve corresponds to a regular amplitude-Rabi measurement of the qubit. A Gaussian pulse of 20 ns σ and varying amplitude is applied at the qubit $|g\rangle \leftrightarrow |e\rangle$ transition, followed by a measurement of the qubit state. The sinusoidal form corresponds to the expected Rabi oscillations of the qubit. The sinusoid amplitude shows the difference in the resonator response when the qubit is in thermal equilibrium (at pulse amplitude 0), and when the qubit population is inverted from thermal equilibrium ($P_{\text{th}}^g \leftrightarrow P_{\text{th}}^e$, at pulse amplitude π). The y -axis is calibrated to show the probability to be in the $|g\rangle$ state, and the details of this calibration are explained belows.

The red curve in Fig. 5.8 shows an identical amplitude-Rabi experiment, made after a Raman cooling sequence to $|g\rangle$. In this sequence, the $|e, 0\rangle \leftrightarrow |g, 1\rangle$ transition is driven for 5 μs . The

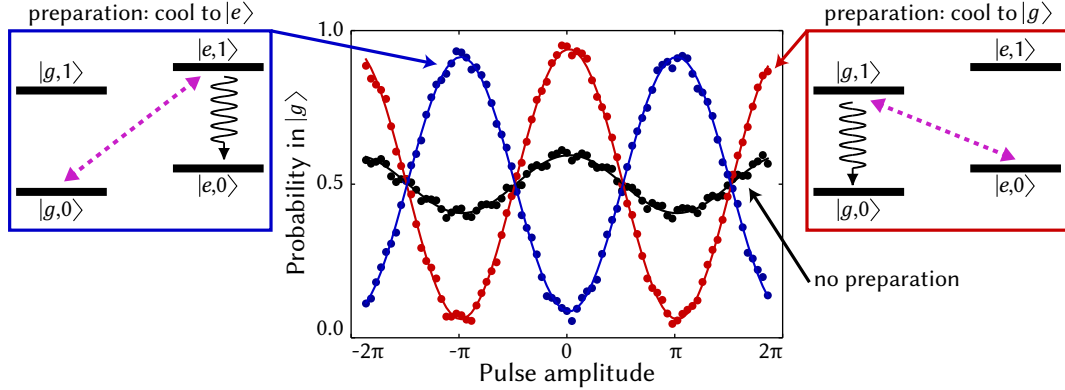


Figure 5.8: An amplitude Rabi experiment on the fluxonium qubit with different initial preparations. A 20 ns σ pulse of varying amplitude is applied at the qubit ($|g\rangle \leftrightarrow |e\rangle$) transition, followed by a measurement of the qubit state. Without preparation (black), the qubit is 60% likely to be in $|g\rangle$, which corresponds to an effective temperature of 62 mK. We repeated the experiment after initially cooling the qubit to $|g\rangle$ by applying a tone resonant with the $|e, 0\rangle \leftrightarrow |g, 1\rangle$ transition (red) for 5 μ s. We obtain 94% probability in $|g\rangle$. Similarly, we cooled the qubit to $|e\rangle$ by driving the $|g, 0\rangle \leftrightarrow |e, 1\rangle$ transition and inverted its population, obtaining 91.5% probability in $|e\rangle$. The straight lines are sinusoidal fits to the measured Rabi oscillations.

state $|g, 1\rangle$ is thus populated, and quickly decays to the state $|g, 0\rangle$ via the decay rate κ of the resonator (see red inset to Fig. 5.8). This increases the population in the ground state, and thus the amplitude of the Rabi oscillations is significantly higher. Similarly, the blue curve shows the same amplitude-Rabi experiment, after a Raman cooling sequence to $|e\rangle$. In this sequence, the $|g, 0\rangle \leftrightarrow |e, 1\rangle$ transition is driven for 5 μ s. The state $|e, 1\rangle$ is thus populated, and quickly decays to the state $|e, 0\rangle$ via the decay rate κ of the resonator (see blue inset to Fig. 5.8). Thus, at pulse amplitude 0 we see a response corresponding to the fluxonium in the $|e\rangle$ state, the new initial state of the amplitude-Rabi experiment.

Let us quantify our results. Recall that we measure the state of the fluxonium via its effect on the resonator frequency, and there are positions in the response I - Q phase-space which correspond to the fluxonium being in $|g\rangle$ and $|e\rangle$ (see Section 4.2). Let us mark half of the distance in phase-space between these two positions as A . Thus, if the initial state of the fluxonium qubit is exactly $|g\rangle$ and it performs perfect Rabi oscillations, the amplitude for these observed oscillations

would be A . However, as our qubit is in thermal equilibrium, the actual measured amplitude is:

$$A_{\text{th}} = A(P_{\text{th}}^g - P_{\text{th}}^e) = A(2P_{\text{th}}^g - 1) \quad (5.11)$$

Similarly, we can define the probability in $|g\rangle$ after the red Raman cooling sequence as P_{red}^g , and the probability in $|e\rangle$ after the blue Raman cooling sequence as P_{blue}^e . Their corresponding Rabi oscillation amplitudes are then:

$$A_{\text{red}} = A(2P_{\text{red}}^g - 1) \quad (5.12)$$

$$A_{\text{blue}} = A(2P_{\text{blue}}^e - 1) \quad (5.13)$$

We can also find expressions for P_{red}^g and P_{blue}^e . Let us label the transition rate of the $|e, 0\rangle \leftrightarrow |g, 1\rangle$ transition as g_{red} . The Raman cooling thus involves a coherent excitation to the state $|g, 1\rangle$ with a rate g_{red} , followed by an incoherent decay of the resonator to $|g, 0\rangle$ at rate κ . As our resonator has a large decay rate $\kappa = 2\pi \times 16.8$ MHz, we can reasonably assume that $g_{\text{red}} \ll \kappa$. We can thus adiabatically eliminate the higher state [Steck, 2007]. A similar process can be done for the $|g, 0\rangle \leftrightarrow |e, 1\rangle$ transition and its rate g_{blue} , and we can even make the approximation that these rates are equal $g_{\text{red}} = g_{\text{blue}} = g_3^{10}$. Thus, we express the cooling rate for both processes using adiabatic elimination:

$$\Gamma_{\text{cool}} = \frac{4g_3^2}{\kappa}. \quad (5.14)$$

Notice that this equation resembles the cavity-induced decay in Section 3.3.4, as our non-linear drive creates a coupling between the fluxonium and the resonator.

The thermal fluxonium population can be described in terms of an “up” rate Γ_{\uparrow} which is the rate of transition $|g\rangle \rightarrow |e\rangle$, and a “down” rate Γ_{\downarrow} which is the rate of transition $|e\rangle \rightarrow |g\rangle$. Their sum equals the total thermalization rate $\Gamma_{\downarrow} + \Gamma_{\uparrow} = \Gamma_1$, and the qubit population is related to them

¹⁰This is a reasonable approximation as these transitions have equal coefficients and matrix elements, and their frequencies are similar (6.3 GHz and 7.3 GHz) - so there should not be a substantial difference in line attenuation.

via:

$$P_{\text{th}}^g = \frac{\Gamma_{\downarrow}}{\Gamma_{\downarrow} + \Gamma_{\uparrow}} = \frac{\Gamma_{\downarrow}}{\Gamma_1} \quad (5.15)$$

from a detailed balance assumption in equilibrium.

The Raman cooling tones then enter to aid the different thermal equilibration rates. The red tone cools the qubit to $|g, 0\rangle$, and thus the cooling rate Γ_{cool} aids Γ_{\downarrow} . Similarly, the blue tone cools the qubit to $|e, 0\rangle$, and thus the cooling rate Γ_{cool} aids Γ_{\uparrow} . We can thus express the populations after cooling as:

$$P_{\text{red}}^g = \frac{\Gamma_{\text{cool}} + \Gamma_{\downarrow}}{\Gamma_{\text{cool}} + \Gamma_{\downarrow} + \Gamma_{\uparrow}} = \frac{4g_3^2 + \kappa\Gamma_{\downarrow}}{4g_3^2 + \kappa\Gamma_{\downarrow} + \kappa\Gamma_{\uparrow}} \quad (5.16)$$

$$P_{\text{blue}}^e = \frac{\Gamma_{\text{cool}} + \Gamma_{\uparrow}}{\Gamma_{\text{cool}} + \Gamma_{\downarrow} + \Gamma_{\uparrow}} = \frac{4g_3^2 + \kappa\Gamma_{\uparrow}}{4g_3^2 + \kappa\Gamma_{\downarrow} + \kappa\Gamma_{\uparrow}} \quad (5.17)$$

Let us summarize all these relations. Eqs. 5.11, 5.12, and 5.13 relate three measured quantities, A_{th} , A_{red} , and A_{blue} , to expressions with several unknowns. From the following equations, we see that we have expressed all of these terms using only three unknowns: A , g_3 , and P_{th}^g . All other unknowns can be expressed using these three, as well as known quantities such as κ and Γ_1 . Thus, we can solve a set of three equations with three unknowns, and extract the thermal population of our fluxonium qubit.

The extracted qubit equilibrium temperature is 62 mK, which corresponds to $P_{\text{th}}^g = 0.6$. We also obtain the population after cooling to $|g\rangle$, $P_{\text{red}}^g = 0.94$, and the population after cooling to $|e\rangle$, $P_{\text{blue}}^e = 0.915$. This is the calibration of the qubit population which is used in Figs. 5.6, 5.8, and 5.9.

This analysis also gives us the transition rate, $g_3 = 2\pi \times 0.87$ MHz. Notice we self-consistently justify our assumption $g_3 \ll \kappa$. We can also compare this measurement to the theoretical prediction. We can relate the value of g_3 to theory from Eq. 5.10 with the addition of a coherent drive amplitude and the matrix element:

$$g_3 = 6\varphi_{\text{ZPF}}^r \alpha_r c_3^{\text{tot}} \phi_0^3 \frac{L_{\text{S}}^{\text{tot}}}{L_q} \frac{L_r (L_{\text{S}}^{\text{tot}})^2}{(L_r + L_{\text{S}}^{\text{tot}})^3} \langle g, 0 | \varphi_r \varphi_q | e, 1 \rangle, \quad (5.18)$$

and all the values in this equation have independent theoretical predictions besides α_r , which is the coherent state population in the resonator which enables this drive. From the measurement of g_3 , we can estimate the photon population in the resonator due to this cooling drive as $|\alpha_r|^2 = 0.35$.

5.3.5 The SNAIL-fluxonium as a Λ -system

In the previous section, we have already seen the use of a Λ -system formed between the low-energy states $|g, 0\rangle$, $|e, 0\rangle$, and the higher state being $|g, 1\rangle$ for the red tone, and $|e, 1\rangle$ for the blue. We observed spontaneous Raman scattering through the higher transition, which allowed us to cool the system to either one of its low-energy eigenstates.

In this Section, we complete the picture by presenting coherent manipulation of a Λ -system formed by the $|g, 0\rangle$, $|e, 0\rangle$, and $|e, 1\rangle$ states of the fluxonium-resonator system. We show Rabi oscillations of the fluxonium qubit at its sweet-spot, with no drive tone being sent at the fluxonium $|g\rangle \leftrightarrow |e\rangle$ transition frequency. The entire manipulation is done through stimulated Raman transition, using detuned drives to the higher energy state $|e, 1\rangle$.

Fig. 5.9a, shows a level diagram for a stimulated Raman transition, in which the transition $|g, 0\rangle \leftrightarrow |e, 0\rangle$ is excited through the virtually populated $|e, 1\rangle$ state. We apply two tones to the system. One direct drive on the resonator (black line in Fig. 5.9a) is sent at frequency $\omega_d = \omega_r - \Delta_r$, where the detuning is fixed to be $\Delta_r = 150$ MHz. Another tone is sent to excite the non-linear transition (magenta line in Fig. 5.9a) at frequency $\omega_{nl} = \omega_r + \omega_q - \Delta_r - \Delta$, where Δ is an additional detuning of the non-linear drive¹¹.

After cooling the fluxonium to $|g, 0\rangle$, we apply both tones together at constant amplitude for a varying amount of time. Fig. 5.9b shows the resulting time-Rabi oscillations, for varying values of the additional detuning Δ of the non-linear drive. Many coherent oscillations are observed, and our results seem very similar to a regular detuned Rabi drive of a qubit. We are able to coherently control the fluxonium qubit on the timescale of ≈ 100 ns using only high-frequency transitions.

We can write an effective Hamiltonian for this system, treating the fluxonium as a two-level

¹¹Note that the drives are not inherently different, as they are both applied at the same port. We associate a tone with a transition because they are closer in frequency to it, but in principle both drives couple to both transitions.

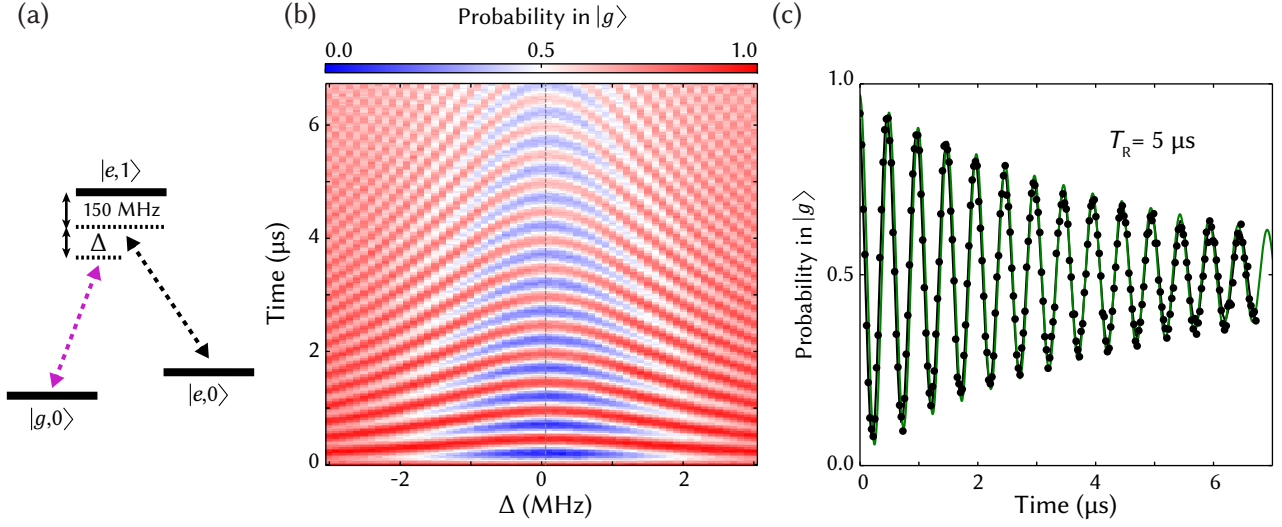


Figure 5.9: (a) Level diagram for a stimulated Raman transition using a direct resonator drive (black) and non-linear drive (magenta) (b) Time Rabi oscillations of the fluxonium qubit using a stimulated Raman transition through the $|e, 1\rangle$ state. Initially the qubit was cooled to the $|g, 0\rangle$ state, followed by two simultaneous tones for a varying time. Both tones were applied 150 MHz detuned from resonance, and the $|g, 0\rangle \leftrightarrow |e, 1\rangle$ had an additional varying detuning Δ . Note the optimal detuning corresponds to $\Delta = 60$ kHz, due to a Stark shift. From this we can infer the amplitude of the coherent $|g, 0\rangle \leftrightarrow |e, 1\rangle$ drive to be $g_3 = 3$ MHz. (c) A cut taken at $\Delta = 100$ kHz. We can infer the decay of Rabi oscillations $T_R = 5 \mu\text{s}$. The green line is a simulation of Eq. 5.20 with only one fit parameter ϵ .

atom:

$$\mathbf{H}_\Lambda/\hbar = \omega_r \mathbf{a}_r^\dagger \mathbf{a}_r + \frac{\omega_q}{2} \boldsymbol{\sigma}_z + \frac{\chi}{2} \mathbf{a}_r^\dagger \mathbf{a}_r \boldsymbol{\sigma}_z + 2\epsilon \cos(\omega_d t) (\mathbf{a}_r + \mathbf{a}_r^\dagger) + 2g_3 \cos(\omega_{nl} t) (\mathbf{a}_r \boldsymbol{\sigma}_- + \mathbf{a}_r^\dagger \boldsymbol{\sigma}_+), \quad (5.19)$$

where g_3 is the transition rate of the non-linear drive (same coefficient as in Eq. 5.18), ϵ is the coefficient of the direct resonator drive and $\chi = 2\pi \times 0.7$ MHz is the dispersive coupling between the fluxonium and the resonator (estimate from the I - Q response of the fluxonium)¹².

By moving to the rotating frames $\mathbf{U}_r = e^{i\mathbf{a}_r^\dagger \mathbf{a}_r \omega_d t}$, $\mathbf{U}_q = e^{i\boldsymbol{\sigma}_z \frac{\omega_q - \Delta}{2} t}$ and taking the RWA, we

¹²As $\chi \ll \kappa$, notice that the resonator transition does not only drive $|e, 0\rangle \leftrightarrow |e, 1\rangle$ but also $|g, 0\rangle \leftrightarrow |g, 1\rangle$. However, this transition is strongly detuned and there is no second transition to “catch” this virtual excitation, and thus this effect can be neglected.

arrive at the time-independent Hamiltonian:

$$\mathbf{H}_\Lambda/\hbar = \Delta_r \mathbf{a}_r^\dagger \mathbf{a}_r + \frac{\Delta}{2} \sigma_z + \frac{\chi}{2} \mathbf{a}_r^\dagger \mathbf{a}_r \sigma_z + \epsilon(\mathbf{a}_r + \mathbf{a}_r^\dagger) + g_3(\mathbf{a}_r \sigma_- + \mathbf{a}_r^\dagger \sigma_+), \quad (5.20)$$

and we can use this Hamiltonian to understand the behavior of the system.

Notice that the Rabi-oscillations in Fig. 5.9b are not quite centered at $\Delta = 0$, but rather are slightly offset at $\Delta = 60$ kHz (the gray dashed line). This is a result of the Stark shift in the non-linear mode, and it is related to the drive amplitude and the detuning by $\Delta_{\text{Stark}} = \frac{g_3^2}{\Delta_r}$ ¹³. This allows us to estimate $g_3 = 2\pi \times 3$ MHz. From Eq. 5.18 we can thus estimate the photon number in the resonator to be $|\alpha_r|^2 = 4.3$ ¹⁴.

Fig. 5.9c shows a cut of Fig. 5.9b at $\Delta = 100$ kHz. From the time Rabi oscillation we can extract the Rabi decay time $T_R = 5 \mu\text{s}$. The measured time is shorter than the prediction for the decay of a resonantly driven atom [Ithier, 2005]: $\Gamma_R = \frac{3}{4}\Gamma_1 + \frac{1}{2}\Gamma_\varphi = 5.9 \mu\text{s}$. This is likely due to an imperfection of the Λ -system simulation of two-level system dynamics. To test this, we simulated the oscillations using Eq. 5.20.

Notice that we have independent measurements of every coefficient in Eq. 5.20 except ϵ . We also know all the decay constant in the fluxonium and resonator, and the initial population of the fluxonium (which was cooled to 94% in $|g, 0\rangle$, see the previous section). Thus, we can simulate the master equation for our system, and fit it to our measurement in Fig. 5.9c with only a single fit parameter ϵ . This numerical simulation result¹⁵ is shown as the green line in the figure. Notice we obtain good agreement with the measurement, and thus we conclude that our Hamiltonian in Eq. 5.20 is a good description for the dynamics of the system.

The value we get is $\epsilon = 2\pi \times 50.8$ MHz, and from it we obtain the effective Rabi rate of our oscillations $\Omega_R = \frac{2g_3\epsilon}{\Delta_r} = 2$ MHz.

¹³See Ref. Steck [2007] Part 6.1.1 for a derivation. Notice that in this case there is only one non-linear mode, and only it experiences a Stark shift.

¹⁴This seems to contradict the transition $|g, 0\rangle \leftrightarrow |e, 1\rangle$ as there are more photons in the cavity. But note that while this drive is on we are in a displaced frame, and the states $|g, 0\rangle$ and $|e, 1\rangle$ are defined from this displaced value. Also note this value is larger than that of the cooling drive by a factor of ≈ 10 , consistent with the generator being set 10 dB higher for this measurement.

¹⁵Numerical master-equation simulations shown in this chapter and the following made use of the QuTiP simulation software in Python [Johansson *et al.*, 2012, 2013].

To conclude, we have shown that by using non-linear coupling via the SNAIL, we are able to drive transitions which are forbidden by the parity selection rule. We use this to construct a Λ -system at the fluxonium sweet-spot, and implement both spontaneous Raman scattering and stimulated Raman transitions within it. To the best of our knowledge, this is the first such superconducting Λ -system. Other superconducting Λ -systems have been made within effective driven systems [Inomata *et al.*, 2014], flux-tunable qubits off of their sweet-spot [Yang *et al.*, 2004, Murali *et al.*, 2004, Valenzuela *et al.*, 2006, Grajcar *et al.*, 2008], and by using two-photon transitions [Kelly *et al.*, 2010, Novikov *et al.*, 2016, Earnest *et al.*, 2017].

This system can be useful for future implementations of the fluxonium qubit and more advanced artificial atoms based on it. This scheme allows us to have two nearly-degenerate eigenstates, while performing all operations and measurements on them using only high frequency drives. Thus we can completely isolate the environment at the resonance frequency of this effective qubit, and improve its coherence without sacrificing our control.

More generally, this is a new artificial atom which expands our capability to synthesize quantum systems. As a Λ -system, it can simulate many interesting effects used in quantum optics with conventional atoms (see Chapter 1). However, while we have used our artificial atom as a Λ -system, it is only one aspect of it. The Hamiltonian in Eq. 5.20 seems like an effective JC-like Hamiltonian where the frequencies of both the resonator and the qubit are tunable, and so is the interaction between them. We can even choose to have beam-splitter-like interaction of the form $\mathbf{a}_r \sigma_+ + \mathbf{a}_r^\dagger \sigma_-$, or two-mode-squeezing-like interaction of the form $\mathbf{a}_r \sigma_- + \mathbf{a}_r^\dagger \sigma_+$, or even both at the same time with independently tunable coefficients. Thus, the new quantum operations that can be implemented using this type of device have not been exhausted, but rather we are only scratching the surface of possibilities.

Chapter 6

Monitoring a qubit along σ_x

In the previous chapters, we saw how to create an artificial two-level atom from a superconducting circuit. It is convenient to write the Hamiltonian for such a system using the Pauli operators. By convention, the z axis is defined as the energy axis of the circuit. $|g\rangle$ and $|e\rangle$, the energy eigenstates of the artificial atom, are taken to be the eigenstates of σ_z with eigenvalues -1 and $+1$ respectively.

The σ_x operator is then used to represent the off-diagonal terms of the Hamiltonian. It flips between the eigenstates of σ_z ($\sigma_x|g\rangle = |e\rangle$ and vice versa) and is thus used to describe drives and interactions which perturb the “original” eigenstates of the Hamiltonian. The presence of a σ_x term in the Hamiltonian usually indicates that our basis is not the basis of energy eigenstates. A possible conclusion would be that σ_x terms lead to a confusing description, and thus should never appear in our Hamiltonian: we should rediagonalize the system to get rid of them. However, there are several occasions where these terms help us describe the physics. For example, a time-dependent perturbation to the Hamiltonian is useful to describe in the unperturbed basis, as this will be the energy basis once the perturbation is turned off. It can also be useful if we are studying an open system. To understand the effects of energy and information loss, it is convenient to work in the basis native to the corresponding loss operators, even if it is not the native Hamiltonian basis.

In this Chapter, we present a qubit made of the eigenstates of σ_x . By using the JC coupling of our (σ_z) artificial atom to a cavity and applying continuous drives, we create an effective JC

Hamiltonian between a σ_x qubit and a harmonic oscillator. As our atom was already artificial, this is a second-order artificial atom which allows for additional flexibility: all system energies and the coupling between them are completely tunable *in situ*.

This effective σ_x JC Hamiltonian can thus be used to study the physics of the Rabi Hamiltonian (Eq. 3.4) in a variety of regimes. It is also interesting to discuss this interaction in the frame of the original σ_z qubit - as in this frame the interaction enables several unique quantum operations that we can add to our toolbox. This Chapter will focus on this aspect of the σ_x qubit.

This Chapter starts with a theoretical description of our driven JC system, and the effective artificial atom which is derived from it. The following section discusses the experimental implementation of the resonant σ_x JC Hamiltonian, which we use to cool the qubit to its transverse eigenstates. The final section discusses the dispersive σ_x JC Hamiltonian, which allows us to continuously monitor the quantum jumps between the transverse eigenstates of our qubit - the first such measurement in any coherent quantum system.

6.1 Theoretical analysis

We begin our treatment with Eq. 3.8, which describes the dispersive JC Hamiltonian made of a two-level atom (qubit) coupled to a harmonic oscillator (cavity):

$$\mathbf{H}_{\text{disp}}/\hbar = \omega_c \mathbf{a}^\dagger \mathbf{a} + \frac{\omega_q}{2} \sigma_z + \frac{\chi}{2} \mathbf{a}^\dagger \mathbf{a} \sigma_z, \quad (6.1)$$

where ω_c is the cavity resonance frequency, ω_q is the qubit resonance frequency and χ is the dispersive shift between the qubit and the cavity. We now add two continuous drive terms to the system: one on the cavity mode with amplitude ϵ_{sb} and frequency ω_{sb} near the cavity resonance frequency ω_c , and one on the qubit mode with amplitude (Rabi frequency) Ω_R at frequency ω_{qd} near the qubit resonance frequency ω_q .

A diagram of the modes and drives can be seen in Fig. 6.1. Note that in the diagram the qubit Rabi drive is shown to be on resonance with the qubit. This is the condition we desire for the Rabi drive, but there is a subtlety in this definition which we discuss shortly. The diagram also includes

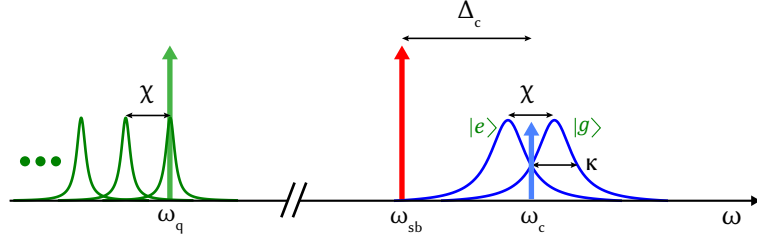


Figure 6.1: Frequency landscape. Our system consists of a qubit at frequency ω_q and cavity with qubit-state-dependent frequency $\omega_c \pm \chi/2$ and linewidth κ . The qubit frequency correspondingly depends on the number of photons in the cavity, changing by χ for every photon. We apply a strong sideband tone (red) detuned from the cavity frequency by Δ_c and a strong Rabi tone (green) at the qubit frequency. Readout is performed by applying a weak readout tone (blue) at the cavity resonance frequency ω_c to readout the system.

an additional probe drive (blue) which is used to read out the system. For now we ignore this tone, and we will return to it as we discuss the experimental results. The total Hamiltonian is now:

$$\mathbf{H}/\hbar = \omega_c \mathbf{a}^\dagger \mathbf{a} + \frac{\omega_q}{2} \sigma_z + \frac{\chi}{2} \mathbf{a}^\dagger \mathbf{a} \sigma_z + \Omega_R \cos(\omega_{qd}t) \sigma_x + 2\epsilon_{sb} \cos(\omega_{sb}t) (\mathbf{a} + \mathbf{a}^\dagger) \quad (6.2)$$

We can move to the rotating frame of both the qubit and the cavity, $\mathbf{U}_c = e^{i\mathbf{a}^\dagger \mathbf{a} \omega_{sb}t}$, $\mathbf{U}_q = e^{i\sigma_z \frac{\omega_{qd}}{2}t}$ and apply the RWA to remove terms oscillating at $2\omega_c$ and $2\omega_q$. We are now left with the time-independent Hamiltonian:

$$\mathbf{H}/\hbar = \Delta_c \mathbf{a}^\dagger \mathbf{a} + \frac{\Delta_q}{2} \sigma_z + \frac{\chi}{2} \mathbf{a}^\dagger \mathbf{a} \sigma_z + \frac{\Omega_R}{2} \sigma_x + \epsilon_{sb} (\mathbf{a} + \mathbf{a}^\dagger), \quad (6.3)$$

where $\Delta_c = \omega_c - \omega_{sb}$ and $\Delta_q = \omega_q - \omega_{qd}$. We can now eliminate the sideband pump by displacing the cavity such that its steady state, which is a coherent state, becomes the new ground state. This can be done using the displacement operator $\mathbf{U}_d = e^{\bar{a}^* \mathbf{a} - \bar{a} \mathbf{a}^\dagger}$ which is equivalent to the change of frame $\mathbf{a} = \bar{a} + \mathbf{d}$, where \mathbf{d} is the new operator of the cavity and \bar{a} , a c-number, is the displacement in phase space. To eliminate the sideband pump term in Eq. 6.3, we choose $\bar{a} = \frac{-\epsilon_{sb}}{\Delta_c - i\kappa/2}$, where κ is the energy relaxation rate of the oscillator (see Section 3.3.2 for more details). Under this

transformation, the Hamiltonian becomes:

$$\mathbf{H}/\hbar = \Delta_c \mathbf{d}^\dagger \mathbf{d} + \frac{\Delta_q + \bar{n}_{sb} \chi}{2} \sigma_z + \frac{\Omega_R}{2} \sigma_x + \frac{\chi}{2} (\bar{a}^* \mathbf{d} + \bar{a} \mathbf{d}^\dagger + \mathbf{d}^\dagger \mathbf{d}) \sigma_z, \quad (6.4)$$

where $\bar{n}_{sb} = \bar{a}^* \bar{a}$. We can now choose $\Delta_q = -\bar{n}_{sb} \chi$ to cancel the σ_z term, as we choose the Rabi drive to be resonant (see Fig. 6.1).

The next trick will be labeling $\sigma_z = \sigma_x^+ + \sigma_x^-$ where σ_x^+ and σ_x^- are the raising and lowering operators of the σ_x eigenstates respectively. We label the eigenstates of σ_x with eigenvalues 1 and -1 as $|+\rangle$ and $|-\rangle$ respectively. And so $\sigma_x^+ |-\rangle = |+\rangle$ and $\sigma_x^- |+\rangle = |-\rangle$. Under this substitution, we can rewrite the Hamiltonian as:

$$\mathbf{H}/\hbar = \Delta_c \mathbf{d}^\dagger \mathbf{d} + \frac{\Omega_R}{2} \sigma_x + \frac{\chi}{2} (\bar{a}^* \mathbf{d} + \bar{a} \mathbf{d}^\dagger + \mathbf{d}^\dagger \mathbf{d}) (\sigma_x^+ + \sigma_x^-) \quad (6.5)$$

This Hamiltonian resembles the Rabi Hamiltonian (Eq. 3.4) between the displaced cavity and the σ_x quadrature of the qubit. The Rabi drive term in the rotating frame can be seen as an undriven transverse qubit with energy difference Ω_R , as discussed in Section 3.3.3, and the dispersive shift term under displacement resembles a linear interaction between the transverse qubit and the cavity, with an effective interaction strength $g_{\text{eff}} = \frac{\chi |\bar{a}|}{2}$.

Notice that Δ_c is tunable by changing the frequency of the sideband drive, Ω_R is tunable by changing the Rabi drive amplitude, and the coupling g_{eff} is tunable by changing the sideband drive amplitude. Thus, we have created an effective Rabi Hamiltonian where every parameter is completely tunable *in situ*, allowing us to explore atom-cavity physics in any regime we are interested in.

As we have done in our JC Hamiltonian treatment in chapter 3, we treat the system in two extreme cases¹: The resonant case where $\Omega_R = \Delta_c$, and the dispersive case where $|\Omega_R - \Delta_c| \gg \frac{|\chi \bar{a}|}{2}$.

¹Notice that these equations are somewhat surprising - they compare the detuning of the sideband drive with the amplitude of the qubit Rabi drive.

6.1.1 Resonant σ_x JC Hamiltonian

In the resonant case, where $\Delta_c = \Omega_R$, we can use the RWA to simplify Eq. 6.5. In the frame rotating at the effective cavity and effective qubit frequency ($U_{cx} = e^{id^\dagger d \Delta_c t}$, $U_{qx} = e^{i\sigma_x \frac{\Omega_R}{2} t}$), we see that terms of the form $d^\dagger \sigma_x^-$ are stationary, while terms of the form $d \sigma_x^-$ rotate at $2\Omega_R$ and terms of the form $d^\dagger d \sigma_x^-$ rotate at Ω_R . The latter two terms can thus be ignored, and we arrive at a true effective resonant JC Hamiltonian (compare to Eq. 3.5):

$$H_{\text{JCx}}/\hbar = \Delta_c d^\dagger d + \frac{\Omega_R}{2} \sigma_x + \frac{\chi \bar{a}}{2} (d \sigma_x^+ + d^\dagger \sigma_x^-), \quad (6.6)$$

where we have assumed \bar{a} is real for simplicity.

The ground state of the Hamiltonian in Eq. 6.6 is $|-, 0\rangle$, with the qubit in its transverse $|-\rangle$ state and the displaced cavity in its ground state. The Purcell effect (see Section 3.3.4) in this case leads to a cooling of the qubit to its transverse ground state, mediated by cavity decay.

In Section 6.2 we present an experimental implementation of this idea, which is published in Ref. Murch *et al.* [2012]. We also present an alternative way to view this effect, in terms of engineering the bath which governs qubit decoherence.

6.1.2 Dispersive σ_x JC Hamiltonian

In the dispersive case, where $|\Delta| = |\Omega_R - \Delta_c| \gg \frac{|\chi \bar{a}|}{2}$, we do not make the RWA but rather keep all the terms in Eq. 6.5. These terms are important, as they add a correction to the dispersive shift².

Similarly to the treatment in Section 3.2, we treat the coupling perturbatively by performing the Schrieffer-Wolff dispersive transformation $U = e^{\frac{\chi}{2\Delta} (\bar{a}^* d \sigma_x^+ - \bar{a} d^\dagger \sigma_x^-)}$ and keeping the terms up to first order in $\frac{\chi |\bar{a}|}{2\Delta}$ [Schrieffer and Wolff, 1966, Blais *et al.*, 2004]. This transformation diagonalizes and removes the zeroth-order term $\frac{\chi}{2} (\bar{a}^* d \sigma_x^+ + \bar{a} d^\dagger \sigma_x^-)$ but we are still left with the zeroth order terms $\frac{\chi}{2} (\bar{a}^* d \sigma_x^- + \bar{a} d^\dagger \sigma_x^+) + \frac{\chi}{2} d^\dagger d (\sigma_x^- + \sigma_x^+)$. To see the contribution arising

²Note that in Section 3.2 we have used the RWA immediately, and we use the JC Eq. 3.5 in both the resonant and dispersive case. This assumes that even in the dispersive case $\Delta \ll 2\omega_q, 2\omega_c$ and so the counter-rotating terms can be neglected. This is not always a reasonable assumption, especially when these are tunable parameters in a driven Hamiltonian. In the experiment presented in Section 6.3, Δ , Δ_c , and Ω_R are actually all of the same order. Thus, we derive the corrections of the counter-rotating terms to the dispersive shift.

from these rotating zeroth order terms, we can perform similar Schrieffer-Wolff transformations $U' = e^{\frac{\chi}{2\Sigma}(\bar{a}d^\dagger\sigma_x^+ - \bar{a}^*d\sigma_x^-)}$ and $U'' = e^{\frac{\chi}{2\Omega_R}d^\dagger d(\sigma_x^+ - \sigma_x^-)}$ where $\Sigma = \Omega_R + \Delta_c$ and we assume $|\Sigma| \gg \frac{\chi|\bar{a}|}{2}$ and $\Omega_R \gg \frac{\chi}{2}$. Performing the three unitary transformations U , U' , and U'' and keeping first order terms in $\frac{\chi|\bar{a}|}{2\Delta}$, $\frac{\chi|\bar{a}|}{2\Sigma}$, and $\frac{\chi}{2\Omega_R}$, we obtain the Hamiltonian:

$$\mathbf{H}/\hbar = \Delta_c d^\dagger d + \frac{\Omega_R + \zeta'/2}{2} \sigma_x + \frac{\zeta}{2} d^\dagger d \sigma_x + \frac{\chi^2}{4\Omega_R} d^\dagger d^\dagger d d \sigma_x, \quad (6.7)$$

where the Lamb shift is $\zeta' = \frac{\chi^2}{2} \left(\frac{\bar{n}_{sb}}{\Delta} + \frac{\bar{n}_{sb}}{\Sigma} \right)$ and the σ_x dispersive shift ζ is:

$$\zeta = \frac{\chi^2}{2} \left(\frac{\bar{n}_{sb}}{\Delta} + \frac{\bar{n}_{sb}}{\Sigma} + \frac{1}{\Omega_R} \right) \quad (6.8)$$

The transformation U'' contributes the final term in Eq. 6.8, but it also gives rise to the final term in Eq. 6.7 - a Kerr term on the displaced cavity which depends on the state of the σ_x qubit. This term is neglected in our experiment as it only affects states with two or more photons, and the population in the displaced cavity is significantly lower. However, in a different experiment this could be an interesting effect by itself.

Suppressing this term and incorporating the Stark shift into the Rabi frequency, we get a true dispersive JC Hamiltonian (compare to Eq. 3.8):

$$\mathbf{H}_{\text{disp}}/\hbar = \Delta_c d^\dagger d + \frac{\Omega_R}{2} \sigma_x + \frac{\zeta}{2} d^\dagger d \sigma_x \quad (6.9)$$

In the dispersive regime, the cooling effect discussed in the previous section is completely suppressed due to the frequency mismatch. However, the second-order effect of this interaction is significant, and possibly even more profound than the resonant case. In the limit of bad cooling, we obtained the ability for a QND measurement of the σ_x qubit operator.

In Section 6.3 we show an experimental implementation of this idea, which is also given in Ref. Vool *et al.* [2016]. We implement the Hamiltonian in Eq. 6.9 and measure the cavity to project the qubit onto its transverse eigenstates. We also utilize the QND nature of this measurement, and continuously measure the qubit to obtain transverse quantum jumps.

6.2 Cooling to $|g\rangle - |e\rangle$

In this section, we present the experiment to cool a superconducting qubit to a state along the equator of the Bloch sphere (Fig. 1.2), mediated by cavity decay. This experiment was performed at the quantum nanoelectronics lab at UC Berkeley, and is published in Ref. Murch *et al.* [2012].

The experimental setup consisted of a standard transmon qubit at $\omega_q/2\pi = 5$ GHz, coupled to a 3D cavity at $\omega_c/2\pi = 6.8$ GHz. The linewidth of the cavity was $\kappa/2\pi = 4.3$ MHz, and the dispersive shift was $\chi/2\pi = -0.66$ MHz.

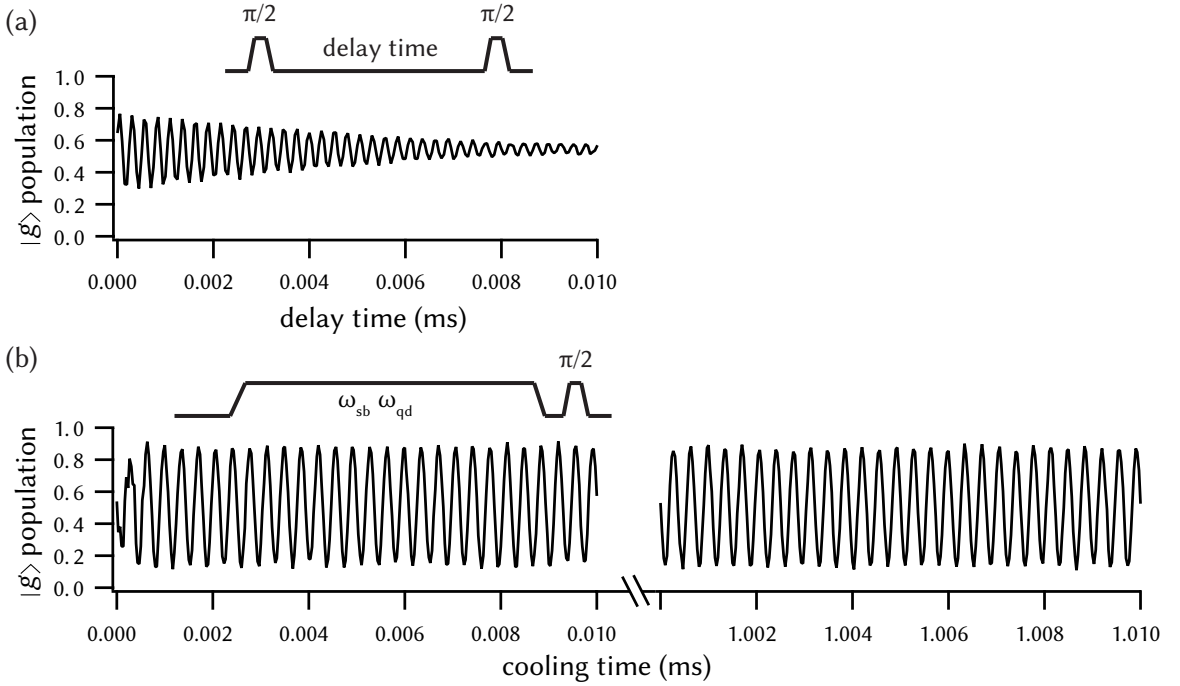


Figure 6.2: (a) A Ramsey measurement of a transmon qubit. The measured Ramsey decay time was $T_{2R} = 4.9 \mu\text{s}$. (b) Ramsey fringes in the presence of the cavity sideband tone at frequency ω_{sb} and the Rabi drive tone at ω_{qd} . The drives are turned on for a varying duration, followed by a $\pi/2$ pulse. Note that T_2 in the presence of the drive was actually shorter (below $1 \mu\text{s}$), yet the Ramsey fringes lasted forever as the system was stabilized into the $|-\rangle$ state.

Fig. 6.2a shows a standard Ramsey experiment of the transmon, which consists two $\pi/2$ pulses with a varying time delay between them. The pulses are intentionally detuned by 2.8 MHz from the qubit frequency to produce the oscillations. The initial $\pi/2$ pulse places the qubit on the Bloch sphere equator, where it rotates at the pulse detuning frequency (in the qubit rotating frame), but

eventually decays to its equilibrium at the center of the Bloch sphere. The final $\pi/2$ pulse is thus just as likely to project the qubit to its $|g\rangle$ or $|e\rangle$ state. The Ramsey decoherence time measured for this qubit was $T_{2R} = 4.9 \mu\text{s}$.

In Fig. 6.2b, we present the Ramsey fringes in the presence of the sideband and Rabi drive tones. The resonance condition for the drives was chosen to be $\Delta_c/2\pi = \Omega_R/2\pi = 9 \text{ MHz}$, meaning we are in the resonant JC regime (see Section 6.1.1). The Rabi drive was on resonance with the qubit, and the sideband drive amplitude was such that $\bar{n}_{sb} = 3.6$. In the experiment presented, no initial $\pi/2$ pulse was applied. The two drives were turned on for a varying amount of time, followed by a final $\pi/2$ pulse.

The infinite Ramsey fringes in Fig. 6.2b, which do not decay even up to 1 ms, show that the equilibrium state of the qubit in the presence of the drives is along the equator. This agrees with the prediction in Section 6.1.1, that the qubit is cooled to the $|-\rangle$ state due to the Purcell effect.

Note that this does not mean that the decoherence time T_2 is infinite! In fact, the decoherence time is visible during the first part of the measurement in Fig. 6.2b, where the qubit decays to its equilibrium state in less than $1 \mu\text{s}$. The dissipation through the cavity cannot improve qubit coherence, it can only make it worse. It is actually important that the engineered dissipation is significantly stronger than the original qubit dissipation, so that we stabilize our desired state.

There is a different formalism with which we can view this experiment, and it can help us quantitatively understand the different rates which are competing in the cooling process. In this interpretation, the cooling experiment is analogous to sideband cooling, in which a red-detuned drive on a high-frequency oscillator cools a low-frequency system through the oscillator dissipation³. This technique has been used to great effect in ion traps [Diedrich *et al.*, 1989], cold atoms [Hamann *et al.*, 1998], and opto/electro-mechanical systems [Teufel *et al.*, 2011].

Fig. 6.3 shows a sketch of this interpretation. The sideband tone (black) is applied below the cavity resonance. A photon of this sideband tone is not quite at the right frequency to enter the

³It is important to note that sideband cooling relies on third-order coupling between the low-frequency and high-frequency systems. Our Hamiltonian uses the transmon non-linearity which only has terms of even order, so there seems to be a contradiction. Notice, however, that the Hamiltonian term $a^\dagger a \sigma_z$ is a third-order term when our qubit is defined along the σ_x axis, and that is the trick at the heart of our scheme. This is a good example of why the notion of order is problematic when we operate in the spin basis (see Section 3.1).

cavity. However, it can take additional energy from an excitation of the effective qubit, and the two combine to create a blue sideband photon at $\omega_{sb} + \Omega_R = \omega_c$. This photon is now precisely on resonance with the cavity and can enter it and be dissipated. This process has taken energy Ω_R from the qubit, and thus it made the transition $|+\rangle \rightarrow |-\rangle$. The opposite process, $|-\rangle \rightarrow |+\rangle$, occurs when an red sideband photon at $\omega_{sb} - \Omega_R$ is created. This photon is even more detuned from the cavity frequency and unlikely to enter, and thus this effect is suppressed and the dominant effect will be cooling to $|-\rangle$ ⁴.

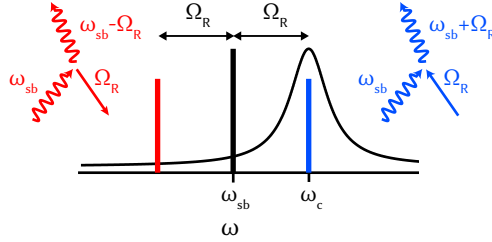


Figure 6.3: The cavity-assisted cooling of a two-level system to the $|-\rangle$ state can be understood as a Raman sideband cooling of the system. The cavity sideband tone at frequency ω_{sb} (straight black line) is detuned from the cavity resonance frequency ω_c . The tone combines with the qubit Rabi frequency Ω_R to produce two sidebands. The upper sideband (blue) takes energy from the qubit to produce a photon of frequency $\omega_d + \Omega_R$ while the lower sideband (red) gives energy to the qubit and creates a photon of frequency $\omega_d - \Omega_R$. As the upper sideband is resonant with the cavity ($\Delta_c = \Omega_R$), the blue process is enhanced and the qubit loses energy to cool into the $|-\rangle$ state.

For a more quantitative understanding, let us recall the spectral density for photon noise in the cavity in the presence of a coherent drive (see Section. 3.3.5 and Eq. 3.24):

$$S_{nn}^d(\omega) = \frac{\bar{n}_{sb}\kappa}{(\omega - \Delta_c)^2 + (\kappa/2)^2}, \quad (6.10)$$

where in this case we are expressing the noise in the presence of the sideband cavity drive. Note that we are in the weak dispersive coupling regime $\chi \ll \kappa$, and thus can use Fermi's golden rule.

⁴Note that this entire process relies on the cavity being in the ground state, as it only allows for photon dissipation, and not photon creation which favors the opposite process. This is a general concept behind sideband cooling, in which a high-frequency system is used to cool a low-frequency system. Even if they are at the same temperature, due to the frequency difference the low-frequency system can be filled with photons while the high-frequency system is completely empty. The sideband tone then converts a low-frequency photon to a high-frequency one which decays, thus cooling the low-frequency system well below thermal equilibrium.

For an undriven qubit, the dephasing corresponds via Fermi's golden rule to the spectral density at $\omega = 0$, as in Eq. 3.22. However, the Rabi drive creates an energy splitting between $|-\rangle$ and $|+\rangle$, and thus we must separate between the rate Γ_- for the process $|+\rangle \rightarrow |-\rangle$, which corresponds to the spectral density at $\omega = \Omega_R$, and the rate Γ_+ for the process $|-\rangle \rightarrow |+\rangle$, which corresponds to the spectral density at $\omega = -\Omega_R$. Thus, we can calculate the two rates:

$$\Gamma_- = \frac{\chi^2}{4} S_{nn}^d(\Omega_R) + \frac{1}{2T_2} = \frac{\chi^2}{\kappa} \bar{n}_{sb} + \frac{1}{2T_2} \quad (6.11)$$

$$\Gamma_+ = \frac{\chi^2}{4} S_{nn}^d(-\Omega_R) + \frac{1}{2T_2} = \frac{\chi^2 \kappa}{16\Omega_R^2 + \kappa^2} \bar{n}_{sb} + \frac{1}{2T_2}, \quad (6.12)$$

where T_2 is the inherent decoherence time of the qubit due to all other decay sources, and we assume it does not prefer one of the transverse eigenstates (as is measured in Fig. 6.2a). Note that the new total qubit decoherence is $\Gamma_- + \Gamma_+$ which is much faster than the qubit coherence without the cavity-induced decay, as we discussed previously. However, $\Gamma_- \gg \Gamma_+$ and thus our equilibrium state is close to $|-\rangle$. The experimental purity of $|-\rangle$ after cooling was 85%, limited by measurement imperfection and population in the second excited state ($|f\rangle$) of the transmon.

Notice that Eq. 6.11 agrees with the Purcell effect expression in Eq. 3.21 when we define the effective coupling strength $g_{\text{eff}} = \frac{\chi|\bar{a}|}{2}$. Thus, these two methods of analyzing the effect are equivalent.

The state $|-\rangle$ is not the only achievable state with this cooling technique. By using the blue sideband detuning, $\Delta_c = -\Omega_R$, we can similarly show that we cool the qubit to its $|+\rangle$ state. Furthermore, by changing the detuning of the Rabi drive, Δ_q , and setting the sideband detuning to be $\Delta_c = \pm \sqrt{\Omega_R^2 + \Delta_q^2}$, we cool the qubit to $\cos \frac{\theta}{2} |g\rangle \mp \sin \frac{\theta}{2} |e\rangle$ where $\theta = \arctan \frac{\Omega_R}{\Delta_q}$. This allows us to cool the qubit to an arbitrary position on the Bloch sphere. However, the cooling rate is reduced compared to the resonant Rabi drive case. A detailed derivation of this result is beyond the scope of this thesis. See Ref. Murch *et al.* [2012] for an experimental realization of cooling to an arbitrary qubit state, and the supplementary material of the reference for a detailed derivation of the cooling rates in the different regimes.

To summarize, we have shown an experimental realization of an effective resonant JC Hamil-

tonian with tunable parameters, and use it to cool a qubit to a coherent superposition of its energy eigenstates. In the following section, we complete the picture by presenting an experimental realization of the effective dispersive JC Hamiltonian.

6.3 Measuring σ_x

In this section, we present a QND measurement of the σ_x operator of our artificial atom. This seems paradoxical, as the static Hamiltonian for a qubit ($\propto \sigma_z$) does not commute with σ_x , and so the projected states evolve during the measurement process, destroying the QND nature of the measurement. However, by using a driven JC system we can create the effective Hamiltonian in Eq. 6.9, which indeed commutes with σ_x . In the static qubit frame, our measurement axis evolves with the Hamiltonian so that the projected state is pointing along the measurement axis at all times, and thus our measurement is not destructive.

Here we describe the experimental implementation of an effective dispersive JC Hamiltonian between a σ_x qubit and a displaced cavity. The idea for this experiment, explained in Section 6.1.2, builds on our theoretical study of the driven JC Hamiltonian, and the experimental work shown in the previous section. We then use this Hamiltonian to perform a QND measurement of the σ_x operator, and thus observe quantum jumps between its eigenstates. This work is published in Ref. Vool *et al.* [2016].

6.3.1 Experimental setup

Our experimental setup, shown in Fig. 6.4, consists of a transmon qubit at frequency $\omega_q/2\pi = 4.9$ GHz coupled to a 3D aluminum cavity with frequency $\omega_c/2\pi = 7.48$ GHz. The cavity has two coupling pins, a weakly coupled input pin with quality factor $Q_{in} \simeq 5 \cdot 10^5$ and strongly coupled output port with $Q_{out} \simeq 1900$, and thus a total decay rate $\kappa/2\pi = 4$ MHz. The qubit has a decay time $T_1 = 90 \mu\text{s}$, a coherence time of $T_{2R} = 40 \mu\text{s}$, and in thermal equilibrium it has an excited state ($|e\rangle$) population of 12%. The dispersive coupling between the qubit and cavity is $\chi/2\pi = -3.2$ MHz. All drives were applied at the input port and the signal from the

output port was amplified by a Josephson Parametric Converter (JPC), a nearly quantum-limited amplifier [Bergeal *et al.*, 2010, Abdo *et al.*, 2013], and later by a high-electron-mobility transistor (HEMT) amplifier, before being demodulated to extract I, Q quadrature measurement outcomes (see Section 4.2).

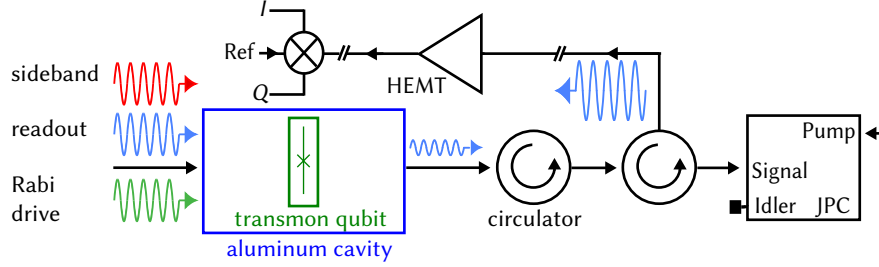


Figure 6.4: Schematic of the experiment setup. A 3D transmon qubit - cavity system is continuously driven by 3 tones termed as sideband (red), readout (blue) and Rabi (green). The readout tone is transmitted through the output port, amplified by a JPC amplifier and demodulated at room temperature to give I, Q signals.

We applied a cavity sideband tone (red) with $\Delta_c/2\pi = 15$ MHz such that the cavity steady state population was $\bar{n}_{sb} = \bar{a}^* \bar{a} = 12$ photons, which set $g_{\text{eff}}/2\pi = \chi|\bar{a}|/4\pi = 5.5$ MHz. The qubit Rabi drive (green) was applied on resonance ($\Delta_q = -\bar{n}_{sb}\chi$), and with varying amplitude Ω_R . These two tones set the effective Hamiltonian, and we also applied a resonant readout tone (blue) on the cavity, to read out the state of the qubit. The readout tone was sent at the cavity resonance frequency ω_c , and with an amplitude such that there were $\bar{n} = 0.9$ photons in the displaced cavity.

6.3.2 Histograms vs. Rabi frequency

The distinct signature of strong dispersive readout is the appearance of two separate Gaussian distributions in I, Q phase space, which correspond to the two qubit states (see Section 4.2). Thus, we applied a continuous readout tone together with our sideband and qubit tones, and demodulated the outgoing readout signal in chunks to obtain a histogram of the equilibrium state of the system.

The histograms in Fig. 6.5 show the I, Q measurement results from a 1 s long readout pulse demodulated every 400 ns. In Fig. 6.5a the Rabi tone was off and our measurement thus projects the system to eigenstates of σ_z , as described in Section 4.2. The top (bottom) distribution correspon-

ding to the $|g\rangle$ ($|e\rangle$) state of the qubit. As we turn up the Rabi tone, our measurement no longer commutes with the system Hamiltonian and a “competition” takes place between the measurement and Rabi drive, sometimes called the quantum Zeno effect [Misra and Sudarshan, 1977, Gambetta *et al.*, 2008]. When the Rabi frequency is below our measurement rate⁵ $\Gamma_m/2\pi = 2.8$ MHz we can still observe two distinct states (Fig. 6.5b), but as it gets much stronger, the measurement can no longer distinguish them (Fig. 6.5c).

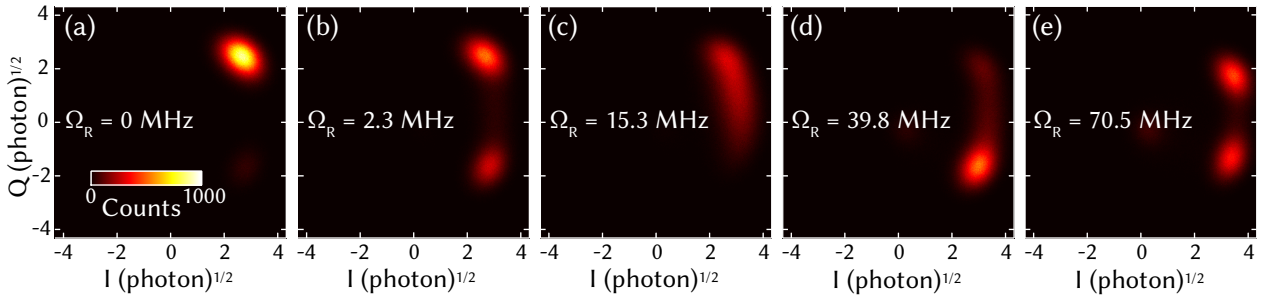


Figure 6.5: Histograms of I, Q measurements in the presence of the readout, sideband and Rabi drives for various indicated values of Ω_R . For each Ω_R , a 1 s continuous trace was recorded and integrated in 400 ns chunks to give an I, Q value, in units of $\sqrt{\text{photon}}$ in the integrated chunk. The sideband and readout drive powers resulted in a steady state population of $\bar{n}_{sb} = 12$ and $\bar{n} = 0.9$ photons in the cavity respectively. The two Gaussian distributions corresponding to the eigenstates of σ_z are visible in (a) and disappear as Ω_R is increased. For large values of Ω_R two new distributions appear, corresponding to the eigenstates of σ_x . The faint distribution near the center in (e) corresponds to the 2nd excited state of the qubit ($|f\rangle$).

However, as the Rabi frequency increases beyond Δ_c , two distinct distributions reappear (Fig. 6.5d and e)! Here we see the remarkable effect the the sideband drive, which creates a Hamiltonian that allows for QND measurement when the Rabi frequency is large. Without this additional drive, the Rabi drive simply washes out the measurement results further as its amplitude increases. This is a strong signature of our desired σ_x measurement.

Fig. 6.5d shows the formation of two distributions, with most of the population in the bottom one and a faint top distribution. As the Rabi frequency increases even further, the bimodality of the histogram becomes more marked and the two sub-populations become more equal (Fig. 6.5e).

⁵The measurement rate is actually exactly the measured-induced dephasing rate of the qubit introduced in Eq. 3.25 for a perfect measurement ($\eta = 1$). Otherwise, the measurement efficiency η (defined in Section 4.2.3) needs to be accounted for. For our measurement chain, $\eta = 0.6$. See Ref. Gambetta *et al.* [2008] for more details.

This can be qualitatively interpreted using the theoretical model in Section 6.1: when the system in Eq. 6.5 is still close to the resonant regime $g_{\text{eff}} \sim |\Omega_R - \Delta_c|$, cavity dissipation cools the system to $|-\rangle$ due to the Purcell effect (Section 6.1.1). Fig. 6.5d shows this effect, with the bottom distribution corresponding to the effective ground state $|-\rangle$ and the faint top distribution corresponding to $|+\rangle$. As the Rabi frequency increases, the coupling becomes more dispersive ($g_{\text{eff}} \ll |\Omega_R - \Delta_c|$) and the cooling effect weakens, as shown by the relative populations in Fig. 6.5e.

The measurements in Fig. 6.5 are only a selection of the measurements taken. The full set of histograms for different values of the Rabi frequency can be seen in the supplementary video to Ref. Vool *et al.* [2016]. The dispersive coupling parameter ζ can be extracted from these histograms by using Eq. 4.4 as ζ is our predicted dispersive shift. Fig. 6.6a shows these extracted ζ values for Rabi frequencies $\Omega_R > 50$ MHz, where we are in the dispersive regime ($g_{\text{eff}} \ll |\Omega_R - \Delta_c|$) and can distinguish two clear blobs in the histogram. The solid red line is the theoretical prediction from Eq. 6.8, and we can see good agreement between the measurement and the theoretical model. Here we can see the importance of adding the contributions of the counter-rotating term to Eq. 6.8, which lead to a correct model.

Notice that as we increased the Rabi frequency, a faint distribution appeared near the center of the figure. This distribution corresponds to the second excited ($|f\rangle$) state of the transmon, which has an 8% population in Fig. 6.5e. In Fig. 6.6b we show the $|f\rangle$ state population for all of our measurements, extracted from the size of its corresponding Gaussian in the histogram. It is reasonable to expect a higher population in the $|f\rangle$ as the Rabi frequency increases, as the drive can overcome the detuning of the $|e\rangle \leftrightarrow |f\rangle$ transition and thus populate the higher excited state. To see if we quantitatively understand this behavior, let us add more terms to the Hamiltonian, to account for the existence of a second excited state:

$$\mathbf{H}_f/\hbar = K|f\rangle\langle f| + \sqrt{2}\Omega_R(|e\rangle\langle f| + |f\rangle\langle e|) + \frac{3\chi}{2}(\bar{a}^*d + \bar{a}d^\dagger + d^\dagger d)|f\rangle\langle f| \quad (6.13)$$

where $K = -200$ MHz is the Kerr non-linearity of the transmon qubit, which is also the detuning of the $|e\rangle \leftrightarrow |f\rangle$ transition from the qubit frequency. The last term shows the dispersive shift due

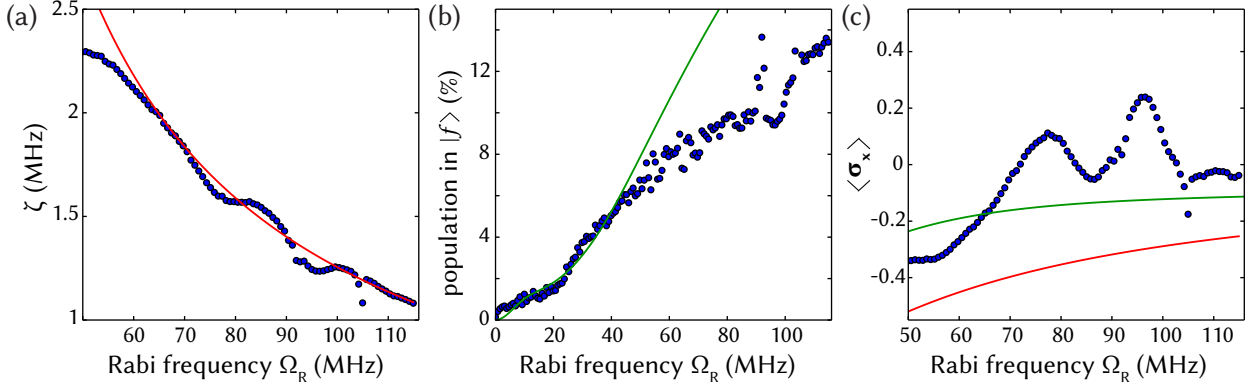


Figure 6.6: Parameters extracted from I, Q histograms for varying Rabi frequency Ω_R . (a) The effective σ_x dispersive shift ζ vs. Ω_R in the dispersive regime $|\Omega_R - \Delta_c| \gg \frac{\chi|\bar{a}|}{2}$. The values were extracted from the I, Q histogram as explained in the text. The theoretical prediction in Eq. 6.8 is shown in red, and there is good agreement between theory and measurement. (b) The population in the 2nd excited state $|f\rangle$ vs. Ω_R . The green line is a numerical master equation simulation containing Hamiltonian $\mathbf{H} + \mathbf{H}_f$ from Eqs. 6.5 and 6.13, and decay operators. At $\Omega_R/2\pi > 50\text{MHz}$ there is a discrepancy between the theory and measurement. (c) The equilibrium expectation value $\langle\sigma_x\rangle$ vs. Ω_R . The red line is a theoretical prediction and the green line is a numerical simulation of a master equation containing the Hamiltonian $\mathbf{H} + \mathbf{H}_f$ from Eqs. 6.5 and 6.13, and decay operators. The equilibrium of the $|+\rangle/|-\rangle$ population does not agree with our predicted models, but exhibits a much more irregular behavior.

to the qubit being in the $|f\rangle$ state. From the first two terms we can see that as the Rabi frequency increases, so does the equilibrium population in $|f\rangle$. The green line in Fig. 6.6b corresponds to a theoretical prediction based on a master-equation simulation including the Hamiltonian $\mathbf{H} + \mathbf{H}_f$ from Eqs. 6.5 and 6.13 as well as decay operations for the cavity and the qubit. While the agreement is good at low Rabi frequencies, for Rabi frequency values $\Omega_R/2\pi > 50\text{ MHz}$ the measured $|f\rangle$ state population is significantly lower than its predicted value.

We verified this effect is not due to even higher excited states by simulating the qubit as 7-level system with fourth order nonlinearity and found similar results. The $|f\rangle$ behavior was unchanged and the third excited state was populated up to 4% for $\Omega_R/2\pi = 100\text{ MHz}$. All higher states were never populated. We currently do not understand the reason for the discrepancy between the measured and predicted population of the $|f\rangle$ for high values of Ω_R .

We also wanted to quantify our statement regarding the equilibrium population of the states

$|-\rangle$ and $|+\rangle$ vs. the Rabi frequency, where we expect the cooling to be less effective as we enter the dispersive regime, and thus obtain populations which are more and more equal. In Fig. 6.6c we show the equilibrium expectation value $\langle \sigma_x \rangle$ extracted from the population in the $|+\rangle$ and $|-\rangle$ distributions of the I, Q histogram, for different values of Ω_R in the dispersive regime. The population fluctuates as a function of the Rabi frequency, sometimes with more population in $|+\rangle$ and sometimes in $|-\rangle$.

To attempt a theoretical analysis of the effective qubit temperature, let us recall that the decay rates Γ_- and Γ_+ which govern it are related to the photon number spectral density, as we have seen in Eqs. 6.11 and 6.12. We can thus express these rates in our case as:

$$\Gamma_- = \frac{\chi^2}{4} S_{nn}^d(\Omega_R) + \frac{1}{2T_2} = \frac{\chi^2 \kappa}{4(\Omega_R - \Delta_c)^2 + \kappa^2} \bar{n}_{sb} + \frac{1}{2T_2} \quad (6.14)$$

$$\Gamma_+ = \frac{\chi^2}{4} S_{nn}^d(-\Omega_R) + \frac{1}{2T_2} = \frac{\chi^2 \kappa}{4(\Omega_R + \Delta_c)^2 + \kappa^2} \bar{n}_{sb} + \frac{1}{2T_2}. \quad (6.15)$$

There is a correction to the equations above due to $\chi \sim \kappa$, where a χ^2 term is added in the denominator as is shown in Eq. 3.26, but we can neglect it in our treatment as the detuning term completely dominates the decay. From these two rates we can obtain the expected population as $\langle \sigma_x \rangle = \frac{\Gamma_+ - \Gamma_-}{\Gamma_+ + \Gamma_-}$.

We can compare this theoretical model to our measurements. For $\Omega_R/2\pi = 70.5$ MHz we can get $1/\Gamma_- = 4 \mu\text{s}$, which agrees with a measurement using quantum jumps that is discussed in Section 6.3.4. However, the theory predicts $1/\Gamma_+ = 9 \mu\text{s}$, while our quantum jumps measurement shows it to be $4 \mu\text{s}$ as well, leading to equal population in $|+\rangle$ and $|-\rangle$. The red line Fig. 6.6c shows our theoretical prediction for $\langle \sigma_x \rangle$ vs. the Rabi frequency, and it deviates significantly from the measurement. This could be a result of the $|f\rangle$ state population, which decays to $|e\rangle$ and thus complicates the equilibrium dynamics. The green line shows the result of a master equation simulation of the Hamiltonian $\mathbf{H} + \mathbf{H}_f$ from Eqs. 6.5 and 6.13 which includes the $|f\rangle$ state, as well as decay operators for the cavity and qubit. The inclusion of the $|f\rangle$ state does predict a higher population in the $|+\rangle$ state as is shown in the figure, but it still does not explain the dynamics of the equilibrium expectation value as a function of the Rabi frequency. The ‘‘peaks’’ around

$\Omega_R = 78, 95$ MHz, where the qubit was more likely to be in the $|+\rangle$ state, are especially confusing. It is possible they are due to specific noise at these frequencies, as note that the inherent dephasing (which contributes to T_2) should also be taken at Ω_R in the presence of the drives. These effects are at present not understood.

The following sections show measurements in which the Rabi drive is chosen to be $\Omega_R/2\pi = 70$ MHz, which is well in the dispersive JC regime, but still with a significant dispersive shift $\zeta = 1.9$ MHz and hopefully below the high drive amplitude where more complicated effects occur.

6.3.3 Measurement characterization

To prove that this measurement projects the qubit to the eigenstates of σ_x , we prepared the system in several well defined states before performing our measurement. We prepared the ground state $|g\rangle$ by standard σ_z dispersive measurement, applied a pulse to prepare a state on the Bloch sphere, and then turned on the Rabi tone with $\Omega_R/2\pi = 70$ MHz and the readout tone (the sideband tone is applied throughout the experiment to maintain the same qubit frame - since the presence of this tone causes a Stark shift of the qubit frequency). In Fig. 6.7a(b), we prepared the system in $|-\rangle$ ($|+\rangle$) and observed 90% (85%) population in the bottom (top) distribution - and so we are indeed measuring the σ_x eigenstates! In Fig. 6.7c and d, we prepared the qubit in $|g\rangle$ and $|i\rangle = (|g\rangle + i|e\rangle)/\sqrt{2}$ respectively, and observed a nearly 50:50 population in both distributions.

To characterize the measurement further, and particularly understand our measurement infidelity, we prepare the qubit along the 3 main axes of the Bloch sphere (Fig. 6.8). For each state we measure the expectation value $\langle\sigma_x\rangle$. The dashed red lines correspond to the expected result of an ideal measurement of $\langle\sigma_x\rangle$. In Fig. 6.8a and b, we observed the expected sinusoidal behavior as we project unto eigenstates of σ_x . Fig. 6.8c shows the axis perpendicular to σ_x and so should have a constant expectation $\langle\sigma_x\rangle = 0$. We observed a 0.2 deviation from this distribution, leaning towards $|-\rangle$ ($|+\rangle$) for negative (positive) angles.

To understand the behavior of the system, we simulated the master equation containing the Hamiltonian $\mathbf{H} + \mathbf{H}_f$ from Eqs. 6.5 and 6.13 and the decay terms κ, T_1 and T_2 . We did not simulate

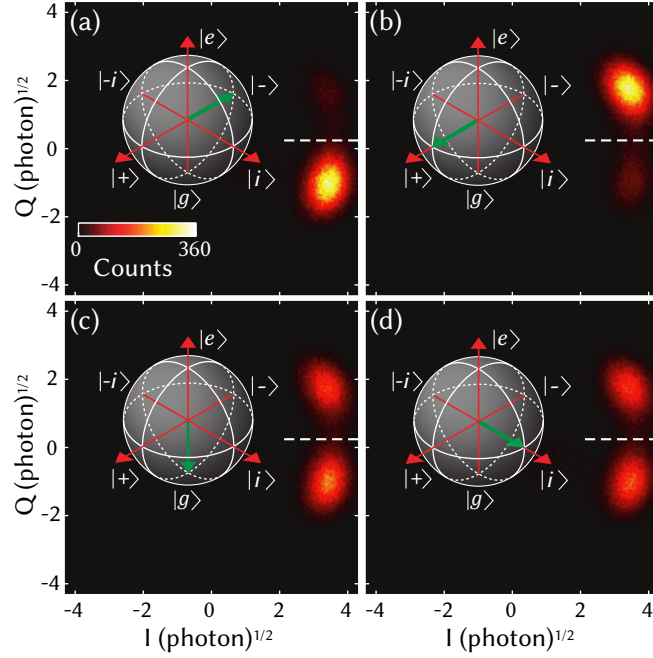


Figure 6.7: The qubit is prepared in $|-\rangle$ (a), $|+\rangle$ (b), $|g\rangle$ (c) and $|i\rangle$ (d) as is shown by the Bloch spheres. We then measure I, Q histograms in the presence of the readout, sideband and Rabi drives ($\Omega_R/2\pi = 70$ MHz). The results for the initializations $|-\rangle$ and $|+\rangle$ show two Gaussian distributions separated by 5.4σ . The initializations $|g\rangle$ and $|i\rangle$ show nearly 50:50 weight in both distributions as expected for $\langle \sigma_x \rangle$. Outcomes above (below) the separatrix (dashed white line) are identified as $|+\rangle$ ($|-\rangle$).

the measurement result, only the state preparation. Thus, in this simulation, the Rabi frequency Ω_R was a time varying term, shaped like a Gaussian with a 4 ns σ width to simulate the physical pulse that we applied. The sideband tone was on during the preparation pulse because the qubit frame needed to be preserved, the tone induces a $\chi \bar{n}_{sb}$ qubit frequency shift, and we need to work in the correct qubit frame. Note that with the sideband tone on and qubit tone off ($\Omega_R = 0$), the sideband-induced lifetime of the qubit is $T_2 = 2 / (\chi^2 S_{nn}^d(\omega = 0)) = 150$ ns (see Eq. 3.22), and so we need to account for this infidelity in our preparation pulses. This agrees with independent T_2 measurements in the presence of the sideband tone but not the qubit tone.

The solid red lines in Fig. 6.8 show the result of this simulation, along with a scaling of 88% and a shift of 2% due to measurement imperfection. Our measurement is imperfect as the qubit state can jump during the measurement ($e^{-T_m \Gamma_-} = 90\%$), or be assigned incorrectly due to overlap

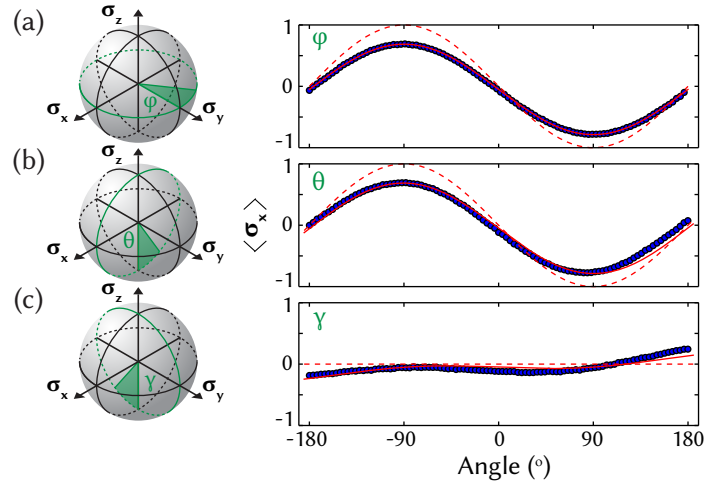


Figure 6.8: The expectation value $\langle \sigma_x \rangle$ is plotted in blue for states prepared on the Bloch sphere surface in the $\sigma_x - \sigma_y$ plane (a), $\sigma_x - \sigma_z$ plane (b) and $\sigma_y - \sigma_z$ plane (c). The dashed red lines in (a)-(c) show the ideal expectation value $\langle \sigma_x \rangle$, while the solid red lines show a theoretical prediction based on a simulation of the cavity-qubit system, including measurement imperfection.

in the Gaussian distributions (1% as they are 5.4σ apart). We can combine these two effects to predict 89% measurement fidelity, while we experimentally obtain 88% by measuring twice in a row and seeing the probability of agreement. There is an additional 2% shift as our measurement slightly prefers the $|-\rangle$ state to the $|+\rangle$ state.

Fig. 6.8a shows good agreement between the data and the theoretical prediction. In Fig. 6.8b and c, the slight discrepancy can be attributed to a slight nonlinearity in the relation between the amplitude of the preparation pulse and the Bloch sphere angle. From these experiments, we conclude that the average fidelity of our σ_x measurement is 88%, which agrees with our theoretical prediction.

The deviation from a straight line in Fig. 6.8c is also captured by our theoretical prediction. It is an artifact of the state preparation, albeit an interesting one as it is also an effect of the σ_x cooling discussed in Section 6.2. During the preparation pulse for states on the $\sigma_y - \sigma_z$ plane, there is a Rabi drive along the σ_x axis, and so with the help of the sideband tone the system is cooled to its lower eigenstate. That is why the system is cooled to opposite states for negative and positive angles, as the sign of the Rabi frequency during the preparation pulse is opposite.

To summarize, we characterize our measurement, and conclude we indeed have a single-shot projective measurement of the σ_x qubit operator with 88% fidelity. In the following section, we discuss the QND nature of our measurement.

6.3.4 Quantum jumps

The appearance of two Gaussian distribution in Fig. 6.5e is already a signature of the QND nature of our readout, as the histogram is taken from a continuous repeated measurement of the system. More direct evidence, however, can be obtained from the time trace of the continuous measurements, where we expect to observe quantum jumps between the eigenstates of our effective Hamiltonian (see Section 4.2.3).

In Fig. 6.9, we show a cut from the 1 s jump trace histogrammed in Fig. 6.5e, where we have defined an angle ψ around the circumcenter of the $|-\rangle$, $|+\rangle$ and $|f\rangle$ distributions (see inset). Jumps between the $|-\rangle$ and $|+\rangle$ states are clearly visible. There are also occasional jumps to the high $|f\rangle$ state which are induced by the strong Rabi drive, as discussed in Section 6.3.2. The dashed orange line corresponds to a two-point filter estimating the state of the qubit⁶.

The average time between jumps from $|+\rangle$ to $|-\rangle$ is $1/\Gamma_- = 4 \mu\text{s}$, which agrees with our theoretical prediction discussed in Section 6.3.2. The average time between $|-\rangle \rightarrow |+\rangle$ jumps is also $1/\Gamma_+ = 4 \mu\text{s}$, which is faster than our prediction, but is consistent with our numerical estimate which includes the effects of the $|f\rangle$ state (see Fig. 6.6c).

Quantum jumps are a result of decay processes which do not commute with the Hamiltonian, and thus their measurement allows us to characterize the dynamics of the decay processes which limit our coherence (see the discussion in Section 4.2.3). The common quantum jumps measure the σ_z qubit operator, and thus give us access to the real-time dynamics of the processes responsible for qubit decay (T_1). The quantum jumps in Fig. 6.9 are of σ_x , and thus give us access to the real-time dynamics of the decoherence processes (T_2) of our physical qubit.

⁶This is a simple “latching” filter in which we declare the qubit to be in its previous state unless it crosses a threshold to another state, usually chosen to be $1 - 2\sigma$ from it. We prefer this filter to a more elaborate and optimal Bayesian filter (for example, see Ref. Gammelmark *et al.* [2014]) when we do not wish to pre-assume a model for the dynamics of the jumps, but study them from the raw data. For more information, see the analysis in Ref. Vool *et al.* [2014], where the quantum jumps are determined to be non-Poissonian.

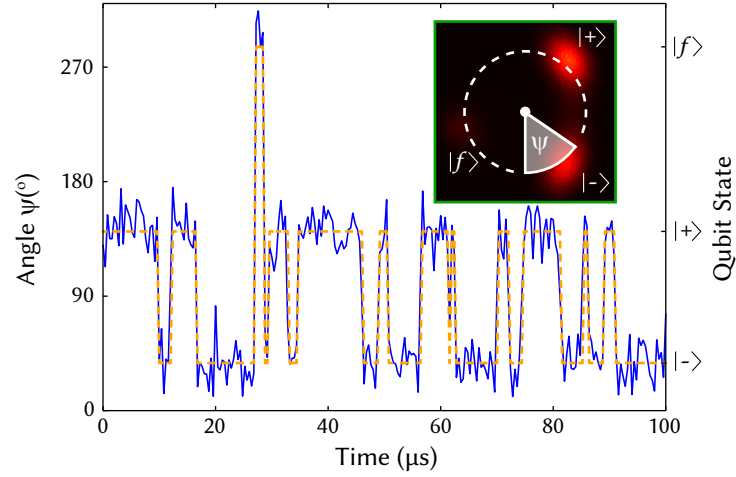


Figure 6.9: A cut of a continuous trace of quantum jumps taken from the measurement histogrammed in Fig. 6.5e. The blue line shows the angle in phase space around the point shown in the inset, and we observe jumps between the eigenstates of σ_x . The dashed orange line is a two-point filter estimate of the state of the qubit. The qubit is sometimes in its second excited state ($|f\rangle$).

There is an important caveat to this claim, as the protocol we use to generate our effective Hamiltonian also induces drive-induced dissipation. In fact, as we saw, the characteristic time between jumps is $1/\Gamma_- = 4 \mu\text{s}$, which is consistent with the dephasing induced by the side-band drive. Thus the dynamics we observe in Fig. 6.9 are due to the sideband drive shot-noise itself. This is not an inherent flaw of the measurement, however, and it can be overcome by using a different parameter regime. Note that the dispersive shift ζ scales like $\frac{\bar{n}_{sb}}{(\Omega_R - \Delta_c)}$ while the dephasing scales like $\frac{\bar{n}_{sb}}{(\Omega_R - \Delta_c)^2}$. This distinction can allow us to increase both the cavity pump power and its detuning, thus keeping the dispersive shift constant while significantly reducing the induced dephasing - allowing us to observe quantum jumps due to the intrinsic qubit dephasing. Measuring the time correlations of these quantum jumps [Vool *et al.*, 2014, Kou *et al.*, 2017] would then give access to the spectral density of qubit dephasing, including both the negative and positive frequency components, and also higher order components of their dynamics. We can also vary the value of Ω_R , and thus probe the real time dynamics of dephasing processes at a particular frequency. This can allow us study to the real-time dynamics of the dephasing noise spectrum [Bylander *et al.*, 2011].

To summarize, we have presented a method to synthesize a tunable effective JC Hamiltonian

between a cavity and an effective qubit, whose eigenstates are transverse superpositions of the bare qubit. We have used this technique in the dispersive regime to observe, for the first time, quantum jumps between the eigenstates of the σ_x qubit operator in the rotating frame.

Above, we discussed a direct application of this technique to study the decoherence processes which limit the coherence of our artificial atoms. Furthermore, our effective JC Hamiltonian is an interesting artificial atom by itself, as it can be tuned to reach the ultra-strong coupling regime ($g_{\text{eff}}/\omega_c^{\text{eff}} \approx 0.1$) and the deep-strong coupling regime ($g_{\text{eff}} > \omega_c^{\text{eff}}, \omega_q^{\text{eff}}$) [Casanova *et al.*, 2010, Yoshihara *et al.*, 2016, Forn-Diaz *et al.*, 2016].

The measurement of eigenstates of σ_x could also be interesting for a fundamental study of competing measurements of non-commuting variables. Recent work [Hacohe-Gourgy *et al.*, 2016] has shown a protocol to measure two non-commuting Pauli operators of a qubit simultaneously⁷. The protocol described here measures the remaining operator, and a combination of both experiments would allow us to measure all 3 Pauli operator of the qubit simultaneously with varying measurement strengths, potentially leading to novel quantum state monitoring [Ruskov *et al.*, 2010].

A potentially even more important aspect of this technique, however, is that it is a proof-of-concept for using drive tones to create effective artificial atoms. The dispersive JC Hamiltonian we are using is one of the most well-studied system in coherent quantum physics, and with the addition of two drive we were able to observe new and unexpected physics. Furthermore, unlike the majority of driven artificial atom operations, there is no resonance condition required for the drives. This suggests that there are many new quantum operations and artificial atoms hiding in plain sight, and are accessible using simple circuits with a clever choice of drive tones. The combination of circuit engineering, which was discussed in the previous chapter, with drive engineering, can capture a large variety of quantum effects, and perhaps allow us to implement an arbitrary quantum system. Such ideas are at the heart of quantum simulation, and necessary for performing quantum error correction and quantum computing using artificial atoms.

⁷The protocol used by UC Berkeley is an interesting and related technique. Their method uses the resonant JC Hamiltonian in Eq. 6.6, with both the red and blue sideband drives on. This implements a process analogous to back-action evading measurement [Clerk *et al.*, 2008]. In a doubly rotating frame, both at the qubit frequency and at the Rabi frequency, this implements a longitudinal measurement of a qubit operator which can be chosen by tuning the amplitudes and phases of the red and blue sideband drives.

Chapter 7

Conclusions and perspectives

In conclusion, the range of quantum operations accessible to us using superconducting artificial atoms, and the variety of quantum systems we can effectively simulate, is rapidly increasing. This thesis reviewed some of the basic concepts in the design of quantum circuits, and the advantages and disadvantages of commonly used circuits. Special attention was spent on the circuit which simulates the JC interaction between a two-level atom and coherent light, a prevalent artificial atom useful for readout, coherent control, and isolation of the quantum system from its environment.

We roughly split the discussion on artificial atom design into two parts. One focused on implementing new artificial atoms by changing the parameters of the different circuit elements, and their arrangement. Although we use only a small selection of circuit elements (a capacitor, an inductor and a Josephson junction), the different combinations and parameter regimes of these allow for a variety of different coherent quantum systems. The second part focused on open quantum systems, in which a circuit is dressed by an external drive, giving rise to a new effective artificial atom with substantially different properties.

We focused on two experiments which explore the design of artificial atoms in these two ways. One focused on the selection rules of artificial atoms, and our ability to break them by using non-linear coupling to drive our atom. We implemented a fluxonium-resonator system at the fluxonium sweet-spot, but were still able to drive forbidden transitions and thus implement a Λ -system. We used this system to manipulate the low-frequency fluxonium states entirely by Raman processes

through the resonator.

The other experiment explored a qubit-cavity system manipulated by two drives. In the presence of these continuous drives, we implemented an effective JC Hamiltonian between an effective qubit in the σ_x quadrature and a displaced cavity. All parameters of the JC Hamiltonian were completely tunable *in situ* by changing the amplitudes and detunings of the drive tones. We used this system in the resonator JC regime to cool the qubit into a superposition of its energy eigenstates. In the dispersive JC regime, we used the system to perform a continuous QND measurement of the σ_x qubit component.

These results are part of a growing push to obtain more interesting and useful artificial atoms, and implement a larger variety of quantum operations. Building on this work and the many other experiments in this growing field, we will soon be able to implement circuits that reach and surpass the complexity of natural atomic systems. We may perhaps approach the goal of a “quantum printer”, the idea that we can take an arbitrary Hamiltonian, and create a physical implementation of it as a quantum circuit.

In the following sections, we discuss possible research ideas which stem from the experiments shown in this thesis. They are listed in ascending order of difficulty, from short-term projects which can be realistically achieved within the next few years, to long-term projects for which significant additional theoretical and experimental understanding is required.

7.1 Integrating the SNAIL

The Snail, discussed in Section 5.2, is a new dipole circuit element with third-order non-linearity. Additionally, there is a parameter choice for the SNAIL in which its fourth-order non-linearity cancels out, and thus it can be approximated as a purely third-order non-linear inductor. The experimental study of the SNAIL, and particularly the characterization of its third-order and fourth-order non-linearity are an on-going research project at Yale during the time of writing of this thesis.

As we better understand the behavior of the SNAIL, we can integrate it into our quantum cir-

circuits to improve their function and allow for new quantum operations. The most direct application of the SNAIL, which has been preliminarily explored in Ref. Frattini *et al.* [2017], is as a quantum-limited amplifier. It can perform three-wave-mixing for phase-preserving amplification, similarly to the JPC, but its dipole (or two-port) nature allows for tessellation of multiple SNAILS together (Fig. 5.3a) to dilute its higher non-linearities for improved bandwidth or dynamic range. It can also be used as a circulator or directional amplifier, based on the JPC design given in Ref. Sliwa *et al.* [2015]. In this context it has the advantage of allowing for multiple pumps, without needing to account for their Stark shifts (as the SNAIL has no Kerr non-linearity), thus making the implementation of this device much simpler. Away from the pure third-order non-linearity regime, the SNAIL can also act as a four-wave-mixing based phase-sensitive amplifier [Vijay, 2008], and both third-wave and four-wave mixing amplification processes can even be performed simultaneously.

The SNAIL can also be integrated as a coupling element and non-linearity source in circuits. This has been shown in Fig. 5.3b, and we have extensively discussed the SNAIL integration into the fluxonium-resonator system to break its selection rules. This implementation has several future directions that will be discussed in the other sections. Here we would like to discuss the integration of the SNAIL with harmonic oscillators as their source of non-linearity, and specifically its integration with a high-Q cavity, which is of growing interest as a quantum system [Vlastakis *et al.*, 2013, Leghtas *et al.*, 2015, Ofek *et al.*, 2016, Wang *et al.*, 2016].

The most obvious implementation of the SNAIL would be as a “Q-switch”. The SNAIL can couple a high-Q memory cavity with a fast readout cavity, and by applying a coherent tone at their frequency difference we create a resonant beam-splitter interaction (see Eq. 5.5) by which the information in the memory cavity can leak through the readout cavity. This is useful as a reset protocol, where the memory cavity remains long-lived, but can be quickly emptied as the drive is turned on [Blumoff *et al.*, 2016]. It is also useful for quantum communication between several memory cavities in a network, by transforming the cavity signal into a traveling wave that can be caught by another distant cavity [Pfaff *et al.*, 2017]. Currently this process is done using two pumps through the four-wave mixing property of a single Josephson junction. The SNAIL can simplify this process to require only a single pump, and without the inherent frequency shifts due

to its Kerr non-linearity.

Non-linearity is also necessary to perform all quantum operations on the high-Q cavity. Currently, these are performed by using the dispersive interaction of the cavity with a transmon qubit, and utilizing its fourth-order non-linearity. This implementation allows for control of the cavity state [Heeres *et al.*, 2017], but with efficiency limited by the transmon coherence time, as it is populated during these gates. The SNAIL may be a better suited coupling element, as its lack of Kerr non-linearity significantly reduces the cavity dependence on the state of the qubit. It also potentially allows for faster gates due to its lower-order non-linearity, but this would require more careful study.

7.2 Raman-controlled qubit

In Section 5.3.5, we discussed the implementation of a Λ -system in a fluxonium-resonator artificial atom, and in Fig. 5.9 we show coherent Rabi oscillations between the ground states of the fluxonium qubit, mediated by a virtual resonator excitation through the Λ -system configuration. Thus we are able to control a transition at 500 MHz, while only applying tones around 7 GHz. This opens the possibility to create a qubit that is manipulated and measured exclusively through the higher energy levels.

The big advantage of this technique is that we can completely filter the qubit environment at its resonance frequency without sacrificing fast control. For the fluxonium design, we can remove the qubit drive pin (see Fig. 4.2b) and further engineer the sample environment so that it is completely impenetrable at the low qubit frequency. Since all control sequences are done at a high frequency which is not filtered, we thus separate the qubit lifetime T_1 from the time it takes to perform qubit operations¹.

It is also possible to perform qubit readout by using high-frequency transitions. Thus we can operate in a regime where the dispersive shift $\chi = 0$, but still measure the state of the qubit -

¹Here we see the advantage of the direct implementation of the drive as opposed to a two-photon process. In our system, we implemented $|g, 0\rangle \leftrightarrow |e, 1\rangle$ directly and can thus perform fast qubit operations even when the direct qubit transition $|g, 0\rangle \leftrightarrow |e, 0\rangle$ is completely inaccessible. The two-photon implementation of $|g, 0\rangle \leftrightarrow |e, 1\rangle$ (as in Ref. Wallraff *et al.* [2007]) relies on the direct qubit transition, and so we cannot filter the qubit while maintaining fast operations on it.

thus separating qubit decoherence (T_2) from the measurement time. For example, this can be done by applying a tone resonant with the $|g, 0\rangle \leftrightarrow |e, 1\rangle$ transition and measuring the signal leaking from the resonator to determine if the qubit is in its ground state. This measurement is not QND, but it can perform fast qubit readout without affecting its dephasing. Such ideas for control and readout through higher states are already used in qubits implemented in ion-traps [Leibfried *et al.*, 2003], nitrogen-vacancy centers [Childress, 2007], and quantum dots [Press *et al.*, 2008].

We can perform QND readout of the qubit by using the back-action evading measurement scheme [Clerk *et al.*, 2008]. By applying both the $|g, 0\rangle \leftrightarrow |e, 1\rangle$ and the $|e, 0\rangle \leftrightarrow |g, 1\rangle$ tones with equal amplitude, we create a Hamiltonian term of the form $\sigma_x(\mathbf{a}_r + \mathbf{a}_r^\dagger)$ in the rotating frame, which allows for QND longitudinal readout of the qubit σ_x operator. This is in fact a separate method to continuously measure σ_x by using the third-order non-linearity of the SNAIL, and can give us access to the dynamics of qubit dephasing at low frequency (as no Rabi frequency Ω_R is applied).

These ideas are useful for the fluxonium artificial atom, whose frequency can be tuned to be < 1 GHz, and whose dispersive shift χ is separately tunable due to higher-energy level dynamics [Zhu *et al.*, 2013, Smith *et al.*, 2016]. There are potentially even more useful for more complex circuits such as the rhombus [Bell *et al.*, 2014], the double-fluxonium [Kou *et al.*, 2016] and the future $\cos 2\varphi$ qubit [Smith *et al.*, 2017]. These circuits have an inherent protection in their lowest eigenstates, which makes them useful as coherent quantum systems, but also makes direct control and readout difficult. Raman-based control through higher excited states may thus be necessary to manipulate these qubits while maintaining their properties.

7.3 Quantum-jump magnetometry

In Section 6.3.4, we discussed the measurement of quantum jumps between the eigenstates of the σ_x qubit. These jumps show us the real-time dynamics of the processes which govern qubit decoherence. This can be useful to study the decoherence effects of the qubit itself. Furthermore, a qubit with high coherence can also serve as a high-sensitivity detector for processes which cause

transitions in the qubit.

Superconducting circuits are commonly used in the sensitive measurement of magnetic field. SQUID loops have been used as magnetometers for several decades [Kleiner *et al.*, 2004], and are continuously improving in their spatial and magnetic field resolution [Finkler *et al.*, 2012, Kirtley *et al.*, 2016]. These systems measure the change in the SQUID inductance due to the presence of DC magnetic flux in the SQUID loop. By building our coherent qubit using a SQUID transmon, we obtain a similar device. Its frequency depends on the DC flux flowing through the SQUID loop, and thus continuous measurement of the frequency allows us to measure the nearby magnetic field. More importantly, the coherence time of the qubit also depends on the magnetic flux, and is potentially much more sensitive, as decoherence due to other sources is suppressed for high-coherence qubits. This idea is inspired by the use of a coherent nitrogen-vacancy center as a magnetometer [Maze *et al.*, 2008].

By implementing our σ_x quantum jump protocol on a flux-sensitive qubit, we would gain access to the real-time dynamics of the AC magnetic field at a tunable frequency (by tuning the value of the Rabi frequency Ω_R). Other methods to obtain the dynamics measure the spectral density of the flux through properly timed echo sequences and spin-locking experiments [Bylander *et al.*, 2011, Yan *et al.*, 2016], but they only give the average value of such a measurement. Using quantum jumps, we basically get the raw data which is used to obtain the spectral density, and thus more information can be extracted from it. For example, we can examine the effective temperature of the system (separate the negative and positive parts of the spectral density) or gain information about higher moments of the dynamics. This can be useful to study chaotic magnetic fields which cannot be easily described by an average measurement. However, it comes at the price of increased complexity, as our scheme requires the use of strong pump tones and single-shot readout.

This measurement can also give us insight into the nature of the flux noise [Koch *et al.*, 1983, Wellstood *et al.*, 1987] which contributes to the coherence of many superconducting artificial atoms.

7.4 Autonomous quantum error correction

Quantum error correction is the idea of encoding of a logical qubit redundantly in a larger Hilbert space, so that decoherence mechanisms can not directly access the encoded information. By using a clever encoding, the information stored in the logical qubit is not erased by a decoherence process, and can be recovered and restored. Even though qubit coherence times are growing, it is established that quantum error correction is crucial for the coherent control of a Hilbert space with many DOF, and thus for the implementation of a quantum computer [Nielsen and Chuang, 2000].

Quantum error correction protocols are usually discussed in a discrete sense, in which syndromes are being repeatedly measured to check for errors, and gates are performed on the system to restore it to its correct state [Gottesman, 1997]. In this convenient framework, the measurements extract entropy from the system and thus reduce the effects of all possible error mechanisms to a limited set of operations, while the encoded information is untouched. If a sufficiently small number of errors has occurred, the original state can be recovered by applying the appropriate gate, and the monitoring of the system continues. This is currently the prevailing method to implement error correction schemes, but the finite time needed for the monitoring and the recovery can limit the error correction efficiency [Kelly *et al.*, 2015, Ofek *et al.*, 2016]. There are alternative ideas to instead perform error correction continuously [Ahn *et al.*, 2002], by continuously performing a weak measurement to detect the error syndromes and continuously correcting by creating a time-dependent feedback Hamiltonian.

An additional improvement may come from a system where continuous error correction is performed autonomously. No feedback or control tones are necessary, but only CW tones and dissipation are used to implement the correction. Such systems have the obvious advantage of avoiding the need for fast control and monitoring, and should in principle require no additional intervention once they are set up. There is a strong connection between such a system and the ideas for effective artificial atoms discussed in this thesis. A system undergoing autonomous error correction can be described as an effective artificial atom which is designed to be protected

from certain noise mechanisms, and thus autonomous error correction is related to the notion of physical or topological protection of quantum information [Douçot and Ioffe, 2012, Kitaev and Laumann, 2009]. Understanding different error correction schemes and incorporating them into our Hamiltonian, which is the essence of autonomous error correction, is actually a good way to design protected artificial atoms.

Ref. Kerckhoff *et al.* [2010] discusses the implementation of the 3-qubit bit-flip (repetition) error correction code autonomously within the framework of cavity QED. This code was later expanded [Kerckhoff *et al.*, 2011] to implement the 9-qubit Bacon-Shor code [Nielsen and Chuang, 2000] which allows for full quantum error correction of an arbitrary single qubit error. The 3-qubit scheme requires three cavity-qubit systems and two control relays. A continuous tone is split and directed to reflect off of the cavities so that the measured error syndromes are encoded onto its phase. Each encoded syndrome is then sent to a control relay, which directs the path of an additional CW tone based on the incoming signal. These additional tones are then used to correct the state of the qubit in case of an error.

The non-standard components required for this scheme are the control relays and the qubits themselves. Both of these components rely on a Λ -type system, and can thus be implemented in cQED using the SNAIL-fluxonium system described in Section 5.3.

The control relay necessary for this scheme is described in Ref. Mabuchi [2009]. The relay itself is also implemented as a qubit-cavity system, and Fig. 7.1a shows the level diagram for the relay qubit, following the notation of the original reference. The Λ structure allows this circuit to act as a switch between the two states $|g\rangle$ and $|h\rangle$. The “set” tone (blue) puts the system in the $|h\rangle$ state via spontaneous Raman scattering (see Section 5.3.4), and similarly the “reset” tone (blue) prepares the $|g\rangle$ state. It is assumed that the tones never appear together. The $|g\rangle \leftrightarrow |e\rangle$ transition is resonant with the cavity. Thus, if the qubit is in the $|g\rangle$ state, the qubit and the cavity are hybridized - which produces a shift of the cavity frequency. A “power” tone (red) sent towards the cavity at the $|g\rangle \leftrightarrow |e\rangle$ frequency will then be reflected back as it is off-resonance. On the other hand, if the qubit is in the $|h\rangle$ state, the “power” tone is resonant with the cavity and will be transmitted. In this way the relay directs the “power” tone, based on the state of the qubit.

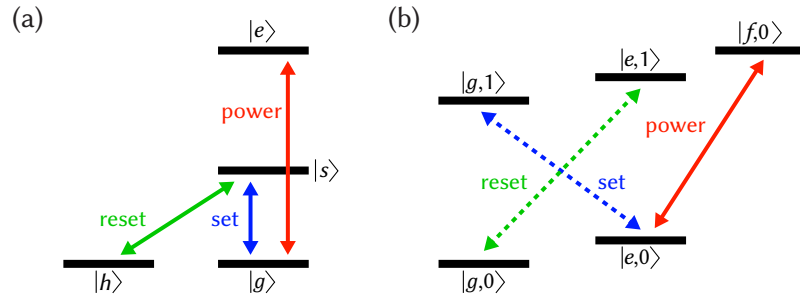


Figure 7.1: (a) Sketch of the control relay level-diagram for a cavity QED atom, given in Ref. Maibuchi [2009]. The “set” and “reset” tones set the system to the $|h\rangle$ and $|g\rangle$ states respectively. The $|g\rangle \leftrightarrow |e\rangle$ transition is resonant with the cavity, and thus the state of the switch directs the output path of a “power” tone sent at the cavity. (b) Level-diagram for the control relay implemented using the SNAIL-fluxonium. The cooling tones from Section 5.3.4 serve as “set” and “reset” tones, and an additional transition, for example the $|e, 0\rangle \leftrightarrow |f, 0\rangle$ fluxonium transition, is chosen for the “power” tone.

In Fig. 7.1b we show a possible SNAIL-fluxonium implementation of the control relay. the “set” and “reset” are performed by the two cooling tones described in Section 5.3.4. The decay of the resonator thus provides the entropy reduction which is necessary for error correction. The cavity is then chosen to be in resonance with another transition, in our case the $|e, 0\rangle \leftrightarrow |f, 0\rangle$ fluxonium transition, but of course other transitions can work just as well. This implements a switch that controls the output port of an incoming drive based on the state of the fluxonium artificial atom. This could be a useful element by itself, in addition to its use for autonomous error correction.

In the original scheme, the two switch states are degenerate, and the “set” and “reset” tones are addressed independently by using different polarizations. For now we do not have that ability by using artificial atoms, and so we address them separately by using two different frequencies. This will require an adjustment to the scheme in Ref. Kerckhoff *et al.* [2010], where the frequency of one of the tones needs to be adjusted prior to entering the relay. This can be done by using three-wave-mixing with a reference signal, by utilizing a JPC or a SNAIL.

The physical qubits in this scheme are only corrected if they receive a signal from both relays. Thus, the correction is done via a stimulated Raman transition that requires two detuned drives to the higher excited state of a Λ -system. This transition has been implemented in Section 5.3.5, and thus a SNAIL-fluxonium can also be used as the physical qubit for this error correction scheme.

The autonomous error correction scheme can thus be fully implemented using the SNAIL-fluxonium. This implementation is only an example, and other artificial atoms are possibly better suited for this experiment. The three-wave-mixing capability of the SNAIL opens up Λ -system interactions for all superconducting circuits, and so it is possible to implement this scheme with a different qubit or with a memory cavity.

Other autonomous error correction schemes are also available in Refs. Kapit *et al.* [2015] and Cohen and Mirrahimi [2014]. The latter implements the 3-qubit bit-flip code for 3 transmon qubits in the strong dispersive JC regime ($\chi \gg \kappa$). By carefully choosing the dispersive shifts of the qubits so they cancel each other, and by applying CW drives and utilizing cavity dissipation, a single qubit bit-flip can be corrected. An extension of this idea to correct for a phase-flip is discussed in Ref. Cohen [2017], which builds on the effective dispersive JC Hamiltonian for the σ_x qubit described in Section 6.3. These ideas can potentially be extended to include a full continuous autonomous quantum error correction of a logical qubit, and even to an autonomous implementation of topological error correction codes [Bardyn and Karzig, 2016].

Bibliography

- Abdo, B., A. Kamal, and M. Devoret (2013), “Nondegenerate three-wave mixing with the Josephson ring modulator,” *Physical Review B* **87** (1), 014508.
- Ahn, C., A. C. Doherty, and A. J. Landahl (2002), “Continuous quantum error correction via quantum feedback control,” *Physical Review A* **65** (4), 042301.
- Allen, L., and J. H. Eberly (1975), *Optical Resonance and Two-level Atoms* (Courier Corporation).
- Ambegaokar, V., and A. Baratoff (1963), “Tunneling Between Superconductors,” *Physical Review Letters* **11** (2), 104–104.
- Arimondo, E., and G. Orriols (1976), “Nonabsorbing atomic coherences by coherent two-photon transitions in a three-level optical pumping,” *Lettere Al Nuovo Cimento* (1971–1985) **17** (10), 333–338.
- Axline, C., M. Reagor, R. Heeres, P. Reinhold, C. Wang, K. Shain, W. Pfaff, Y. Chu, L. Frunzio, and R. J. Schoelkopf (2016), “An architecture for integrating planar and 3d cQED devices,” *Applied Physics Letters* **109** (4), 042601.
- Bardyn, C.-E., and T. Karzig (2016), “Exponential lifetime improvement in topological quantum memories,” *Physical Review B* **94** (9), 094303.
- Baur, M., S. Filipp, R. Bianchetti, J. M. Fink, M. Göppl, L. Steffen, P. J. Leek, A. Blais, and A. Wallraff (2009), “Measurement of Autler-Townes and Mollow Transitions in a Strongly Driven Superconducting Qubit,” *Physical Review Letters* **102** (24), 243602.
- Bell, M. T., J. Paramanandam, L. B. Ioffe, and M. E. Gershenson (2014), “Protected Josephson Rhombus Chains,” *Physical Review Letters* **112** (16), 167001.
- Bergeal, N., F. Schackert, M. Metcalfe, R. Vijay, V. E. Manucharyan, L. Frunzio, D. E. Prober, R. J. Schoelkopf, S. M. Girvin, and M. H. Devoret (2010), “Phase-preserving amplification near the quantum limit with a Josephson ring modulator,” *Nature* **465** (7294), 64–U70.
- Bergmann, K., H. Theuer, and B. W. Shore (1998), “Coherent population transfer among quantum states of atoms and molecules,” *Reviews of Modern Physics* **70** (3), 1003–1025.
- Bergquist, J. C., R. G. Hulet, W. M. Itano, and D. J. Wineland (1986), “Observation of Quantum Jumps in a Single Atom,” *Phys. Rev. Lett.* **57** (14), 1699–1702.

- Bertet, P., I. Chiorescu, G. Burkard, K. Semba, C. J. P. M. Harmans, D. P. DiVincenzo, and J. E. Mooij (2005a), “Dephasing of a Superconducting Qubit Induced by Photon Noise,” *Physical Review Letters* **95** (25), 257002.
- Bertet, P., I. Chiorescu, C. J. P. M. Harmans, and J. E. Mooij (2005b), “Dephasing of a flux-qubit coupled to a harmonic oscillator,” arXiv:cond-mat/0507290 .
- Blais, A., J. Gambetta, A. Wallraff, D. I. Schuster, S. M. Girvin, M. H. Devoret, and R. J. Schoelkopf (2007), “Quantum-information processing with circuit quantum electrodynamics,” *Physical Review A* **75** (3), 032329.
- Blais, A., R. S. Huang, A. Wallraff, S. M. Girvin, and R. J. Schoelkopf (2004), “Cavity quantum electrodynamics for superconducting electrical circuits: An architecture for quantum computation,” *Physical Review A* **69** (6), 062320.
- Blumoff, J., K. Chou, C. Shen, M. Reagor, C. Axline, R. Brierley, M. Silveri, C. Wang, B. Vlastakis, S. Nigg, L. Frunzio, M. Devoret, L. Jiang, S. Girvin, and R. Schoelkopf (2016), “Implementing and Characterizing Precise Multiqubit Measurements,” *Physical Review X* **6** (3), 031041.
- Boissonneault, M., J. M. Gambetta, and A. Blais (2009), “Dispersive regime of circuit QED: Photon-dependent qubit dephasing and relaxation rates,” *Physical Review A* **79** (1), 013819.
- Bouchiat, V., D. Vion, P. Joyez, D. Esteve, and M. H. Devoret (1998), “Quantum coherence with a single Cooper pair,” *Physica Scripta* **1998** (T76), 165.
- Braginsky, V. B., Y. I. Vorontsov, and K. S. Thorne (1980), “Quantum Nondemolition Measurements,” *Science* **209** (4456), 547–557.
- Brecht, T., Y. Chu, C. Axline, W. Pfaff, J. Blumoff, K. Chou, L. Krayzman, L. Frunzio, and R. Schoelkopf (2017), “Micromachined Integrated Quantum Circuit Containing a Superconducting Qubit,” *Physical Review Applied* **7** (4), 044018.
- Brethau, L., . . . Girit, H. Pothier, D. Esteve, and C. Urbina (2013), “Exciting Andreev pairs in a superconducting atomic contact,” *Nature* **499** (7458), 312–315.
- Breuer, H.-P., and F. Petruccione (2002), *The Theory of Open Quantum Systems* (Oxford University Press).
- Brooks, P., A. Kitaev, and J. Preskill (2013), “Protected gates for superconducting qubits,” *Phys. Rev. A* **87** (5), 052306.
- Bruus, H., and K. Flensberg (2004), *Many-Body Quantum Theory in Condensed Matter Physics: An Introduction* (OUP Oxford).
- Bylander, J., S. Gustavsson, F. Yan, F. Yoshihara, K. Harrabi, G. Fitch, D. G. Cory, Y. Nakamura, J.-S. Tsai, and W. D. Oliver (2011), “Noise spectroscopy through dynamical decoupling with a superconducting flux qubit,” *Nat Phys* **7** (7), 565–570.
- Callen, H. B., and T. A. Welton (1951), “Irreversibility and Generalized Noise,” *Physical Review* **83** (1), 34–40.

- Casanova, J., G. Romero, I. Lizuain, J. J. García-Ripoll, and E. Solano (2010), “Deep Strong Coupling Regime of the Jaynes-Cummings Model,” *Phys. Rev. Lett.* **105** (26), 263603.
- Castellanos-Beltran, M. A., K. D. Irwin, G. C. Hilton, L. R. Vale, and K. W. Lehnert (2008), “Amplification and squeezing of quantum noise with a tunable Josephson metamaterial,” *Nature Physics* **4** (12), 929–931.
- Chan, J., T. P. M. Alegre, A. H. Safavi-Naeini, J. T. Hill, A. Krause, S. Gröblacher, M. Aspelmeyer, and O. Painter (2011), “Laser cooling of a nanomechanical oscillator into its quantum ground state,” *Nature* **478** (7367), 89–92.
- Childress, L. (2007), *Coherent manipulation of single quantum systems in the solid state*, Ph.D. thesis (Harvard University).
- Childress, L., M. V. G. Dutt, J. M. Taylor, A. S. Zibrov, F. Jelezko, J. Wrachtrup, P. R. Hemmer, and M. D. Lukin (2006), “Coherent Dynamics of Coupled Electron and Nuclear Spin Qubits in Diamond,” *Science* **314** (5797), 281–285.
- Chiorescu, I., P. Bertet, K. Semba, Y. Nakamura, C. J. P. M. Harmans, and J. E. Mooij (2004), “Coherent dynamics of a flux qubit coupled to a harmonic oscillator,” *Nature* **431** (7005), 159–162.
- Chiorescu, I., Y. Nakamura, C. J. P. M. Harmans, and J. E. Mooij (2003), “Coherent Quantum Dynamics of a Superconducting Flux Qubit,” *Science* **299** (5614), 1869–1871.
- Cirac, J. I., and P. Zoller (1995), “Quantum Computations with Cold Trapped Ions,” *Physical Review Letters* **74** (20), 4091–4094.
- Clarke, J. (1966), “A superconducting galvanometer employing Josephson tunnelling,” *Philosophical Magazine* **13** (121), 115–127.
- Clarke, J., and A. I. Braginski (2006), *The SQUID Handbook: Fundamentals and Technology of SQUIDs and SQUID Systems* (John Wiley & Sons).
- Clarke, J., and F. K. Wilhelm (2008), “Superconducting quantum bits,” *Nature* **453** (7198), 1031–1042.
- Clerk, A. A., M. H. Devoret, S. M. Girvin, F. Marquardt, and R. J. Schoelkopf (2010), “Introduction to quantum noise, measurement, and amplification,” *Rev. Mod. Phys.* **82** (2), 1155–1208.
- Clerk, A. A., F. Marquardt, and K. Jacobs (2008), “Back-action evasion and squeezing of a mechanical resonator using a cavity detector,” *New Journal of Physics* **10** (9), 095010.
- Clerk, A. A., and D. W. Utami (2007), “Using a qubit to measure photon-number statistics of a driven thermal oscillator,” *Physical Review A* **75** (4), 042302.
- Cohen, J. (2017), *Autonomous quantum error correction with superconducting qubit*, Ph.D. thesis (ENS).
- Cohen, J., and M. Mirrahimi (2014), “Dissipation-induced continuous quantum error correction for superconducting circuits,” *Physical Review A* **90** (6), 062344.

- De Gennes, P. G. (1999), *Superconductivity of Metals and Alloys* (Westview Press).
- Devoret, M. H. (1997), in *"Quantum Fluctuations" (Les Houches Session LXIII)* (Elsevier, Amsterdam).
- Devoret, M. H., and R. J. Schoelkopf (2013), "Superconducting Circuits for Quantum Information: An Outlook," *Science* **339** (6124), 1169–1174.
- Diedrich, F., J. C. Bergquist, W. M. Itano, and D. J. Wineland (1989), "Laser Cooling to the Zero-Point Energy of Motion," *Phys. Rev. Lett.* **62** (4), 403–406.
- Dirac, P. A. M. (1967), *The Principles of Quantum Mechanics* (Oxford University Press, O).
- Dolan, G. J. (1977), "Offset masks for liftoff photoprocessing," *Applied Physics Letters* **31** (5), 337–339.
- Douçot, B., and L. B. Ioffe (2012), "Physical implementation of protected qubits," *Reports on Progress in Physics* **75** (7), 072001.
- Douçot, B., and J. Vidal (2002), "Pairing of Cooper Pairs in a Fully Frustrated Josephson-Junction Chain," *Physical Review Letters* **88** (22), 227005.
- Duan, L.-M., M. D. Lukin, J. I. Cirac, and P. Zoller (2001), "Long-distance quantum communication with atomic ensembles and linear optics," *Nature* **414** (6862), 413–418.
- Earnest, N., S. Chakram, Y. Lu, N. Irons, R. K. Naik, N. Leung, J. Lawrence, J. Koch, and D. I. Schuster (2017), "Realization of a Λ system with metastable states of a capacitively-shunted fluxonium," arXiv:1707.00656 .
- Feynman, R. P., R. B. Leighton, and M. L. Sands (1963), *The Feynman lectures on physics* (Addison-Wesley Pub. Co., Reading, Mass.).
- Finkler, A., D. Vasyukov, Y. Segev, L. Neeman, Y. Anahory, Y. Myasoedov, M. L. Rappaport, M. E. Huber, J. Martin, A. Yacoby, and E. Zeldov (2012), "Nano sized SQUID-on-tip for scanning probe microscopy," *Journal of Physics: Conference Series* **400** (5), 052004.
- Forn-Diaz, P., J. J. Garcia-Ripoll, B. Peropadre, M. A. Yurtalan, J. L. Orgiazzi, R. Belyansky, C. M. Wilson, and A. Lupascu (2016), "Ultrastrong coupling of a single artificial atom to an electromagnetic continuum," arXiv:1602.00416 .
- Foster, R. M. (1924), "A Reactance Theorem," *Bell System Technical Journal* **3** (2), 259–267.
- Frattini, N. E., U. Vool, S. Shankar, A. Narla, K. M. Sliwa, and M. H. Devoret (2017), "3-wave mixing Josephson dipole element," *Applied Physics Letters* **110** (22), 222603.
- Gambetta, J., A. Blais, M. Boissonneault, A. A. Houck, D. I. Schuster, and S. M. Girvin (2008), "Quantum trajectory approach to circuit QED: Quantum jumps and the Zeno effect," *Phys. Rev. A* **77** (1), 012112.
- Gambetta, J., A. Blais, D. I. Schuster, A. Wallraff, L. Frunzio, J. Majer, M. H. Devoret, S. M. Girvin, and R. J. Schoelkopf (2006), "Qubit-photon interactions in a cavity: Measurement-induced dephasing and number splitting," *Phys. Rev. A* **74** (4), 042318.

- Gammelmark, S., K. Mølmer, W. Alt, T. Kampschulte, and D. Meschede (2014), “Hidden Markov model of atomic quantum jump dynamics in an optically probed cavity,” *Physical Review A* **89** (4), 043839.
- Gardiner, C., and P. Zoller (2004), *Quantum Noise* (Springer-Verlag Berlin Heidelberg).
- Geerlings, K. (2013), *Improving Coherence in Superconducting Qubits and Resonators*, Ph.D. thesis (Yale University).
- Geerlings, K., Z. Leghtas, I. M. Pop, S. Shankar, L. Frunzio, R. J. Schoelkopf, M. Mirrahimi, and M. H. Devoret (2013), “Demonstrating a Driven Reset Protocol for a Superconducting Qubit,” *Physical Review Letters* **110** (12), 120501.
- Girvin, S. M. (2011), *Circuit QED: Superconducting Qubits Coupled to Microwave Photons*, Les Houches Summer school lecture notes, available online at <https://sites.google.com/site/stevenmgirvin/girvin-les-houches-lecture-notes-drafts>.
- Gottesman, D. (1997), *Stabilizer Codes and Quantum Error Correction*, Ph.D. thesis (California Institute of Technology).
- Grajcar, M., S. H. W. van der Ploeg, A. Izmailkov, E. Il'ichev, H.-G. Meyer, A. Fedorov, A. Shnirman, and G. Schön (2008), “Sisyphus cooling and amplification by a superconducting qubit,” *Nature Physics* **4** (8), 612–616.
- Gray, H. R., R. M. Whitley, and C. R. Stroud (1978), “Coherent trapping of atomic populations,” *Optics Letters* **3** (6), 218–220.
- Hacohen-Gourgy, S., L. S. Martin, E. Flurin, V. V. Ramasesh, K. B. Whaley, and I. Siddiqi (2016), “Quantum dynamics of simultaneously measured non-commuting observables,” *Nature* **538** (7626), 491–494.
- Hamann, S. E., D. L. Haycock, G. Klose, P. H. Pax, I. H. Deutsch, and P. S. Jessen (1998), “Resolved-Sideband Raman Cooling to the Ground State of an Optical Lattice,” *Phys. Rev. Lett.* **80** (19), 4149–4152.
- Hanson, R., L. P. Kouwenhoven, J. R. Petta, S. Tarucha, and L. M. K. Vandersypen (2007), “Spins in few-electron quantum dots,” *Reviews of Modern Physics* **79** (4), 1217–1265.
- Haroche, S., and J.-M. Raimond (2006), *Exploring the Quantum: Atoms, Cavities and Photons* (Oxford University Press, Oxford).
- Harris, D. C., and M. D. Bertolucci (1978), *Symmetry and Spectroscopy: An Introduction to Vibrational and Electronic Spectroscopy* (Courier Corporation).
- Hatridge, M., S. Shankar, M. Mirrahimi, F. Schackert, K. Geerlings, T. Brecht, K. M. Sliwa, B. Abdo, L. Frunzio, S. M. Girvin, R. J. Schoelkopf, and M. H. Devoret (2013), “Quantum Back-Action of an Individual Variable-Strength Measurement,” *Science* **339** (6116), 178–181.
- Hatridge, M., R. Vijay, D. H. Slichter, J. Clarke, and I. Siddiqi (2011), “Dispersive magnetometry with a quantum limited SQUID parametric amplifier,” *Physical Review B* **83** (13), 134501.

- Heeres, R. W., P. Reinhold, N. Ofek, L. Frunzio, L. Jiang, M. H. Devoret, and R. J. Schoelkopf (2017), “Implementing a universal gate set on a logical qubit encoded in an oscillator,” *Nature Communications* **8** (1), 94.
- Houck, A. A., J. A. Schreier, B. R. Johnson, J. M. Chow, J. Koch, J. M. Gambetta, D. I. Schuster, L. Frunzio, M. H. Devoret, S. M. Girvin, and R. J. Schoelkopf (2008), “Controlling the Spontaneous Emission of a Superconducting Transmon Qubit,” *Phys. Rev. Lett.* **101** (8), 080502.
- Hover, D., Y.-F. Chen, G. J. Ribeill, S. Zhu, S. Sendelbach, and R. McDermott (2012), “Superconducting low-inductance undulatory galvanometer microwave amplifier,” *Applied Physics Letters* **100** (6), 063503.
- Inomata, K., K. Koshino, Z. Lin, W. Oliver, J. Tsai, Y. Nakamura, and T. Yamamoto (2014), “Microwave Down-Conversion with an Impedance-Matched Λ System in Driven Circuit QED,” *Physical Review Letters* **113** (6), 063604.
- Ithier, G. (2005), *Manipulation, readout and analysis of the decoherence of a superconducting quantum bit*, Ph.D. thesis (CEA-Saclay).
- Ithier, G., E. Collin, P. Joyez, P. J. Meeson, D. Vion, D. Esteve, F. Chiarello, A. Shnirman, Y. Makhlin, J. Schrieffer, and G. Schön (2005), “Decoherence in a superconducting quantum bit circuit,” *Physical Review B* **72** (13), 134519.
- Jaksch, D., J. I. Cirac, P. Zoller, S. L. Rolston, R. Côté, and M. D. Lukin (2000), “Fast Quantum Gates for Neutral Atoms,” *Physical Review Letters* **85** (10), 2208–2211.
- Janvier, C., L. Tosi, L. Bretheau, Ç. Ö. Girit, M. Stern, P. Bertet, P. Joyez, D. Vion, D. Esteve, M. F. Goffman, H. Pothier, and C. Urbina (2015), “Coherent manipulation of Andreev states in superconducting atomic contacts,” *Science* **349** (6253), 1199–1202.
- Jaynes, E. T., and F. W. Cummings (1963), “Comparison of Quantum and Semiclassical Radiation Theories With Application To Beam Maser,” *Proceedings of the Ieee* **51** (1), 89–&.
- Jelezko, F., T. Gaebel, I. Popa, A. Gruber, and J. Wrachtrup (2004), “Observation of Coherent Oscillations in a Single Electron Spin,” *Physical Review Letters* **92** (7), 076401.
- Johansson, J. R., P. D. Nation, and F. Nori (2012), “QuTiP: An open-source Python framework for the dynamics of open quantum systems,” *Computer Physics Communications* **183** (8), 1760 – 1772.
- Johansson, J. R., P. D. Nation, and F. Nori (2013), “QuTiP 2: A Python framework for the dynamics of open quantum systems,” *Computer Physics Communications* **184** (4), 1234–1240.
- Josephson, B. (1962), “Possible new effects in superconductive tunnelling,” *Physics Letters* **1** (7), 251–253.
- Kapit, E., J. T. Chalker, and S. H. Simon (2015), “Passive correction of quantum logical errors in a driven, dissipative system: A blueprint for an analog quantum code fabric,” *Physical Review A* **91** (6), 062324.

- Kelly, J., R. Barends, A. G. Fowler, A. Megrant, E. Jeffrey, T. C. White, D. Sank, J. Y. Mutus, B. Campbell, Y. Chen, Z. Chen, B. Chiaro, A. Dunsworth, I. C. Hoi, C. Neill, P. J. J. O'Malley, C. Quintana, P. Roushan, A. Vainsencher, J. Wenner, A. N. Cleland, and J. M. Martinis (2015), "State preservation by repetitive error detection in a superconducting quantum circuit," *Nature* **519** (7541), 66–69.
- Kelly, W. R., Z. Dutton, J. Schlafer, B. Mookerji, T. A. Ohki, J. S. Kline, and D. P. Pappas (2010), "Direct Observation of Coherent Population Trapping in a Superconducting Artificial Atom," *Physical Review Letters* **104** (16), 163601.
- Kerckhoff, J., H. I. Nurdin, D. S. Pavlichin, and H. Mabuchi (2010), "Designing Quantum Memories with Embedded Control: Photonic Circuits for Autonomous Quantum Error Correction," *Physical Review Letters* **105** (4), 040502.
- Kerckhoff, J., D. S. Pavlichin, H. Chalabi, and H. Mabuchi (2011), "Design of nanophotonic circuits for autonomous subsystem quantum error correction," *New Journal of Physics* **13** (5), 055022.
- Kirtley, J. R., L. Paulius, A. J. Rosenberg, J. C. Palmstrom, C. M. Holland, E. M. Spanton, D. Schiessl, C. L. Jermain, J. Gibbons, Y.-K.-K. Fung, M. E. Huber, D. C. Ralph, M. B. Ketchen, G. W. Gibson, and K. A. Moler (2016), "Scanning SQUID susceptometers with sub-micron spatial resolution," *Review of Scientific Instruments* **87** (9), 093702.
- Kitaev, A., and C. Laumann (2009), "Topological phases and quantum computation," arXiv:0904.2771 [cond-mat, physics:quant-ph] ArXiv: 0904.2771.
- Kitagawa, T., E. Berg, M. Rudner, and E. Demler (2010), "Topological characterization of periodically driven quantum systems," *Physical Review B* **82** (23), 235114.
- Kleiner, R., D. Koelle, F. Ludwig, and J. Clarke (2004), "Superconducting quantum interference devices: State of the art and applications," *Proceedings of the IEEE* **92** (10), 1534–1548.
- Koch, J., V. Manucharyan, M. H. Devoret, and L. I. Glazman (2009), "Charging Effects in the Inductively Shunted Josephson Junction," *Phys. Rev. Lett.* **103** (21), 217004.
- Koch, J., T. M. Yu, J. Gambetta, A. A. Houck, D. I. Schuster, J. Majer, A. Blais, M. H. Devoret, S. M. Girvin, and R. J. Schoelkopf (2007), "Charge-insensitive qubit design derived from the Cooper pair box," *Phys. Rev. A* **76** (4), 042319.
- Koch, R., J. Clarke, J. Martinis, W. Goubau, C. Pegrum, and D. Harlingen (1983), "Investigation of 1/f noise in tunnel junction DC SQUIDS," *IEEE Transactions on Magnetics* **19** (3), 449–452.
- Kou, A., W. C. Smith, U. Vool, R. T. Brierley, H. Meier, L. Frunzio, S. M. Girvin, L. I. Glazman, and M. H. Devoret (2016), "A fluxonium-based artificial molecule with a tunable magnetic moment," arXiv:1610.01094 .
- Kou, A., W. C. Smith, U. Vool, I. M. Pop, K. M. Sliwa, M. H. Hatridge, L. Frunzio, and M. H. Devoret (2017), "Simultaneous monitoring of fluxonium qubits in a waveguide," arXiv:1705.05712 .
- Krogstrup, P., N. L. B. Ziino, W. Chang, S. M. Albrecht, M. H. Madsen, E. Johnson, J. Nygård, C. M. Marcus, and T. S. Jespersen (2015), "Epitaxy of semiconductor–superconductor nanowires," *Nature Materials* **14** (4), 400–406.

- Laporte, O., and W. F. Meggers (1925), “Some Rules of Spectral Structure*,” *JOSA* **11** (5), 459–463.
- Larsen, T., K. Petersson, F. Kuemmeth, T. Jespersen, P. Krogstrup, J. Nygård, and C. Marcus (2015), “Semiconductor-Nanowire-Based Superconducting Qubit,” *Physical Review Letters* **115** (12), 127001.
- Laucht, A., R. Kalra, S. Simmons, J. P. Dehollain, J. T. Muhonen, F. A. Mohiyaddin, S. Freer, F. E. Hudson, K. M. Itoh, D. N. Jamieson, J. C. McCallum, A. S. Dzurak, and A. Morello (2017), “A dressed spin qubit in silicon,” *Nature Nanotechnology* **12** (1), 61–66.
- Lecocq, F., I. M. Pop, Z. Peng, I. Matei, T. Crozes, T. Fournier, Cécile Naud, W. Guichard, and O. Buisson (2011), “Junction fabrication by shadow evaporation without a suspended bridge,” *Nanotechnology* **22** (31), 315302.
- Leggett, A. J. (1980), “Macroscopic Quantum Systems and the Quantum Theory of Measurement,” *Progress of Theoretical Physics Supplement* **69**, 80–100.
- Leggett, A. J. (1987), *Quantum mechanics at the macroscopic level*, in “*Chance and Matter*”, edited by J. Souletie, J. Vanniménus, and R. Stora (North Holland).
- Leghtas, Z., S. Touzard, I. M. Pop, A. Kou, B. Vlastakis, A. Petrenko, K. M. Sliwa, A. Narla, S. Shankar, M. J. Hatridge, M. Reagor, L. Frunzio, R. J. Schoelkopf, M. Mirrahimi, and M. H. Devoret (2015), “Confining the state of light to a quantum manifold by engineered two-photon loss,” *Science* **347** (6224), 853–857.
- Leghtas, Z., U. Vool, S. Shankar, M. Hatridge, S. M. Girvin, M. H. Devoret, and M. Mirrahimi (2013), “Stabilizing a Bell state of two superconducting qubits by dissipation engineering,” *Physical Review A* **88** (2), 023849.
- Leibfried, D., R. Blatt, C. Monroe, and D. Wineland (2003), “Quantum dynamics of single trapped ions,” *Reviews of Modern Physics* **75** (1), 281–324.
- Lin, Y.-H., L. B. Nguyen, N. Grabon, J. S. Miguel, N. Pankratova, and V. E. Manucharyan (2017), “Protecting a superconducting qubit from energy decay by selection rule engineering,” arXiv:1705.07873 .
- Lindner, N. H., G. Refael, and V. Galitski (2011), “Floquet topological insulator in semiconductor quantum wells,” *Nature Physics* **7** (6), 490–495.
- Liu, Y. (2016), *Quantum Feedback Control of Multiple Superconducting Qubits*, Ph.D. thesis (Yale University).
- Liu, Y.-x., L. F. Wei, J. S. Tsai, and F. Nori (2006), “Controllable Coupling between Flux Qubits,” *Physical Review Letters* **96** (6), 067003.
- Liu, Y.-x., J. Q. You, L. F. Wei, C. P. Sun, and F. Nori (2005), “Optical Selection Rules and Phase-Dependent Adiabatic State Control in a Superconducting Quantum Circuit,” *Physical Review Letters* **95** (8), 087001.
- Lloyd, S. (1992), “Any nonlinear gate, with linear gates, suffices for computation,” *Physics Letters A* **167** (3), 255–260.

- London, P., J. Scheuer, J.-M. Cai, I. Schwarz, A. Retzker, M. B. Plenio, M. Katagiri, T. Teraji, S. Koizumi, J. Isoya, R. Fischer, L. P. McGuinness, B. Naydenov, and F. Jelezko (2013), “Detecting and Polarizing Nuclear Spins with Double Resonance on a Single Electron Spin,” *Physical Review Letters* **111** (6), 067601.
- Loss, D., and D. P. DiVincenzo (1998), “Quantum computation with quantum dots,” *Physical Review A* **57** (1), 120–126.
- Ludlow, A. D., M. M. Boyd, J. Ye, E. Peik, and P. Schmidt (2015), “Optical atomic clocks,” *Reviews of Modern Physics* **87** (2), 637–701.
- Mabuchi, H. (2009), “Cavity-QED models of switches for attojoule-scale nanophotonic logic,” *Physical Review A* **80** (4), 045802.
- Manucharyan, V. E. (2011), *Superinductance*, Ph.D. thesis (Yale University).
- Manucharyan, V. E., E. Boaknin, M. Metcalfe, R. Vijay, I. Siddiqi, and M. Devoret (2007), “Microwave bifurcation of a Josephson junction: Embedding-circuit requirements,” *Physical Review B* **76** (1), 014524.
- Manucharyan, V. E., J. Koch, L. I. Glazman, and M. H. Devoret (2009), “Fluxonium: Single cooper-pair circuit free of charge offsets,” *Science* **326** (5949), 113–116.
- Masluk, N. A., I. M. Pop, A. Kamal, Z. K. Mineev, and M. H. Devoret (2012), “Microwave Characterization of Josephson Junction Arrays: Implementing a Low Loss Superinductance,” *Physical Review Letters* **109** (13), 137002.
- Matveev, K. A., A. I. Larkin, and L. I. Glazman (2002), “Persistent Current in Superconducting Nanorings,” *Phys. Rev. Lett.* **89** (9), 096802.
- Maze, J. R., P. L. Stanwix, J. S. Hodges, S. Hong, J. M. Taylor, P. Cappellaro, L. Jiang, M. V. G. Dutt, E. Togan, A. S. Zibrov, A. Yacoby, R. L. Walsworth, and M. D. Lukin (2008), “Nanoscale magnetic sensing with an individual electronic spin in diamond,” *Nature* **455** (7213), 644–647.
- Miller, R., T. E. Northup, K. M. Birnbaum, A. Boca, A. D. Boozer, and H. J. Kimble (2005), “Trapped atoms in cavity QED: coupling quantized light and matter,” *Journal of Physics B: Atomic, Molecular and Optical Physics* **38** (9), S551.
- Mirrahimi, M., Z. Leghtas, V. V. Albert, S. Touzard, R. J. Schoelkopf, L. Jiang, and M. H. Devoret (2014), “Dynamically protected cat-qubits: a new paradigm for universal quantum computation,” *New Journal of Physics* **16**, 045014.
- Misra, B., and E. C. G. Sudarshan (1977), “The Zeno’s paradox in quantum theory,” *Journal of Mathematical Physics* **18** (4), 756–763.
- Mollow, B. R. (1969), “Power Spectrum of Light Scattered by Two-Level Systems,” *Physical Review* **188** (5), 1969–1975.
- Monroe, C., D. M. Meekhof, B. E. King, W. M. Itano, and D. J. Wineland (1995), “Demonstration of a Fundamental Quantum Logic Gate,” *Physical Review Letters* **75** (25), 4714–4717.

- Mooij, J. E., T. P. Orlando, L. Levitov, L. Tian, C. H. v. d. Wal, and S. Lloyd (1999), “Josephson Persistent-Current Qubit,” *Science* **285** (5430), 1036–1039.
- Murali, K. V. R. M., Z. Dutton, W. D. Oliver, D. S. Crankshaw, and T. P. Orlando (2004), “Probing Decoherence with Electromagnetically Induced Transparency in Superconductive Quantum Circuits,” *Physical Review Letters* **93** (8), 087003.
- Murch, K. W., U. Vool, D. Zhou, S. J. Weber, S. M. Girvin, and I. Siddiqi (2012), “Cavity-Assisted Quantum Bath Engineering,” *Physical Review Letters* **109** (18), 183602.
- Nagourney, W., J. Sandberg, and H. Dehmelt (1986), “Shelved optical electron amplifier: Observation of quantum jumps,” *Physical Review Letters* **56** (26), 2797–2799.
- Nakamura, Y., Y. A. Pashkin, and J. S. Tsai (1999), “Coherent control of macroscopic quantum states in a single-Cooper-pair box,” *Nature* **398** (6730), 786–788.
- Nielsen, M. A., and I. L. Chuang (2000), *Quantum Computation and Quantum Information* (Cambridge University Press, Cambridge).
- Nigg, S. E., H. Paik, B. Vlastakis, G. Kirchmair, S. Shankar, L. Frunzio, M. H. Devoret, R. J. Schoelkopf, and S. M. Girvin (2012), “Black-Box Superconducting Circuit Quantization,” *Physical Review Letters* **108** (24), 240502.
- Novikov, S., T. Sweeney, J. E. Robinson, S. P. Premaratne, B. Suri, F. C. Wellstood, and B. S. Palmer (2016), “Raman coherence in a circuit quantum electrodynamics lambda system,” *Nature Physics* **12** (1), 75–79.
- Nowack, K. C., F. H. L. Koppens, Y. V. Nazarov, and L. M. K. Vandersypen (2007), “Coherent Control of a Single Electron Spin with Electric Fields,” *Science* **318** (5855), 1430–1433.
- Ofek, N., A. Petrenko, R. Heeres, P. Reinhold, Z. Leghtas, B. Vlastakis, Y. Liu, L. Frunzio, S. M. Girvin, L. Jiang, M. Mirrahimi, M. H. Devoret, and R. J. Schoelkopf (2016), “Extending the lifetime of a quantum bit with error correction in superconducting circuits,” *Nature* **536** (7617), 441–445.
- Paik, H., D. I. Schuster, L. S. Bishop, G. Kirchmair, G. Catelani, A. P. Sears, B. R. Johnson, M. J. Reagor, L. Frunzio, L. I. Glazman, S. M. Girvin, M. H. Devoret, and R. J. Schoelkopf (2011), “Observation of High Coherence in Josephson Junction Qubits Measured in a Three-Dimensional Circuit QED Architecture,” *Physical Review Letters* **107** (24), 240501.
- Petrenko, A. (2016), *Enhancing the Lifetime of Quantum Information with Cat States in Superconducting Cavities*, Ph.D. thesis (Yale University).
- Pfaff, W., C. J. Axline, L. D. Burkhardt, U. Vool, P. Reinhold, L. Frunzio, L. Jiang, M. H. Devoret, and R. J. Schoelkopf (2017), “Controlled release of multiphoton quantum states from a microwave cavity memory,” *Nature Physics* 10.1038/nphys4143.
- Pfaff, W., B. Hensen, H. Bernien, S. B. v. Dam, M. S. Blok, T. H. Taminiau, M. J. Tiggelman, R. N. Schouten, M. Markham, D. J. Twitchen, and R. Hanson (2014), “Unconditional quantum teleportation between distant solid-state quantum bits,” *Science* **345**, 1253512.

- Pop, I. M., T. Fournier, T. Crozes, F. Lecocq, I. Matei, B. Pannetier, O. Buisson, and W. Guichard (2012), "Fabrication of stable and reproducible submicron tunnel junctions," *Journal of Vacuum Science & Technology B, Nanotechnology and Microelectronics: Materials, Processing, Measurement, and Phenomena* **30** (1), 010607.
- Pop, I. M., K. Geerlings, G. Catelani, R. J. Schoelkopf, L. I. Glazman, and M. H. Devoret (2014), "Coherent suppression of electromagnetic dissipation due to superconducting quasiparticles," *Nature* **508** (7496), 369–372.
- Pozar, D. M. (2011), *Microwave Engineering*, 4th ed. (Wiley, Hoboken, NJ).
- Press, D., T. D. Ladd, B. Zhang, and Y. Yamamoto (2008), "Complete quantum control of a single quantum dot spin using ultrafast optical pulses," *Nature* **456** (7219), 218–221.
- Purcell, E. M. (1946), "Spontaneous Emission Probabilities at Radio Frequencies," *Phys. Rev.* **69** (11-12), 681.
- Reagor, M., H. Paik, G. Catelani, L. Sun, C. Axline, E. Holland, I. M. Pop, N. A. Masluk, T. Brecht, L. Frunzio, M. H. Devoret, L. Glazman, and R. J. Schoelkopf (2013), "Reaching 10 ms single photon lifetimes for superconducting aluminum cavities," *Applied Physics Letters* **102** (19), 192604.
- Reagor, M., W. Pfaff, C. Axline, R. W. Heeres, N. Ofek, K. Sliwa, E. Holland, C. Wang, J. Blumoff, K. Chou, M. J. Hatridge, L. Frunzio, M. H. Devoret, L. Jiang, and R. J. Schoelkopf (2016), "Quantum memory with millisecond coherence in circuit QED," *Physical Review B* **94** (1), 014506.
- Rouchon, P., and M. Mirrahimi (2010), "Modeling and Control of Quantum systems," Available at "<http://cas.ensmp.fr/~rouchon/QuantumSyst/>".
- Ruskov, R., A. N. Korotkov, and K. Mølmer (2010), "Qubit State Monitoring by Measurement of Three Complementary Observables," *Phys. Rev. Lett.* **105** (10), 100506.
- Saffman, M., T. G. Walker, and K. Mølmer (2010), "Quantum information with Rydberg atoms," *Reviews of Modern Physics* **82** (3), 2313–2363.
- Sauter, T., W. Neuhauser, R. Blatt, and P. E. Toschek (1986), "Observation of Quantum Jumps," *Phys. Rev. Lett.* **57** (14), 1696–1698.
- Schackert, F. (2013), *A Practical Quantum-Limited Parametric Amplifier Based on the Josephson Ring Modulator*, Ph.D. thesis (Yale University).
- Schrieffer, J. R., and P. A. Wolff (1966), "Relation between the Anderson and Kondo Hamiltonians," *Phys. Rev.* **149** (2), 491–492.
- Schuster, D. I., A. Wallraff, A. Blais, L. Frunzio, R.-S. Huang, J. Majer, S. M. Girvin, and R. J. Schoelkopf (2005), "ac Stark Shift and Dephasing of a Superconducting Qubit Strongly Coupled to a Cavity Field," *Physical Review Letters* **94** (12), 123602.
- Sears, A. P., A. Petrenko, G. Catelani, L. Sun, H. Paik, G. Kirchmair, L. Frunzio, L. I. Glazman, S. M. Girvin, and R. J. Schoelkopf (2012), "Photon shot noise dephasing in the strong-dispersive limit of circuit QED," *Physical Review B* **86** (18), 180504.

- Shankar, S., M. Hatridge, Z. Leghtas, K. M. Sliwa, A. Narla, U. Vool, S. M. Girvin, L. Frunzio, M. Mirrahimi, and M. H. Devoret (2013), “Autonomously stabilized entanglement between two superconducting quantum bits,” *Nature* **504** (7480), 419–422.
- Slichter, C. P. (1990), *Principles of Magnetic Resonance* (Springer-Verlag, New York).
- Slichter, D. H., R. Vijay, S. J. Weber, S. Boutin, M. Boissonneault, J. M. Gambetta, A. Blais, and I. Siddiqi (2012), “Measurement-Induced Qubit State Mixing in Circuit QED from Up-Converted Dephasing Noise,” *Physical Review Letters* **109** (15), 153601.
- Sliwa, K. (2016), *Improving the Quality of Heisenberg Back-Action of Qubit Measurements made with Parametric Amplifiers*, Ph.D. thesis (Yale University).
- Sliwa, K., M. Hatridge, A. Narla, S. Shankar, L. Frunzio, R. Schoelkopf, and M. Devoret (2015), “Reconfigurable Josephson Circulator/Directional Amplifier,” *Physical Review X* **5** (4), 041020.
- Smith, W. C., A. Kou, U. Vool, and M. H. Devoret (2017), In preparation.
- Smith, W. C., A. Kou, U. Vool, I. M. Pop, L. Frunzio, R. J. Schoelkopf, and M. H. Devoret (2016), “Quantization of inductively shunted superconducting circuits,” *Physical Review B* **94** (14), 144507.
- Solgun, F., D. W. Abraham, and D. P. DiVincenzo (2014), “Blackbox quantization of superconducting circuits using exact impedance synthesis,” *Physical Review B* **90** (13), 134504.
- Solgun, F., and D. P. DiVincenzo (2015), “Multiport Impedance Quantization,” arXiv:1505.04116 .
- Steck, D. A. (2007), *Quantum and Atom Optics*, available online at <http://steck.us/teaching>.
- Teufel, J. D., T. Donner, D. Li, J. W. Harlow, M. S. Allman, K. Cicak, A. J. Sirois, J. D. Whittaker, K. W. Lehnert, and R. W. Simmonds (2011), “Sideband cooling of micromechanical motion to the quantum ground state,” *Nature* **475** (7356), 359–363.
- Tinkham, M. (2004), *Introduction to Superconductivity: Second Edition*, 2nd ed. (Dover Publications).
- Valenzuela, S. O., W. D. Oliver, D. M. Berns, K. K. Berggren, L. S. Levitov, and T. P. Orlando (2006), “Microwave-Induced Cooling of a Superconducting Qubit,” *Science* **314** (5805), 1589–1592.
- Vijay, R. (2008), *Josephson Bifurcation Amplifier: Amplifying quantum signals using a dynamical bifurcation*, Ph.D. thesis (Yale University).
- Vijay, R., C. Macklin, D. H. Slichter, S. J. Weber, K. W. Murch, R. Naik, A. N. Korotkov, and I. Siddiqi (2012), “Stabilizing Rabi oscillations in a superconducting qubit using quantum feedback,” *Nature* **490** (7418), 77–80.
- Vijay, R., D. H. Slichter, and I. Siddiqi (2011), “Observation of Quantum Jumps in a Superconducting Artificial Atom,” *Physical Review Letters* **106** (11), 110502.
- Vitanov, N. V., A. A. Rangelov, B. W. Shore, and K. Bergmann (2017), “Stimulated Raman adiabatic passage in physics, chemistry, and beyond,” *Reviews of Modern Physics* **89** (1), 015006.

- Vlastakis, B., G. Kirchmair, Z. Leghtas, S. E. Nigg, L. Frunzio, S. M. Girvin, M. Mirrahimi, M. H. Devoret, and R. J. Schoelkopf (2013), “Deterministically Encoding Quantum Information Using 100-Photon Schrödinger Cat States,” *Science* **342** (6158), 607–610.
- Vool, U., and M. Devoret (2017), “Introduction to quantum electromagnetic circuits,” *International Journal of Circuit Theory and Applications* 10.1002/cta.2359.
- Vool, U., I. M. Pop, K. Sliwa, B. Abdo, C. Wang, T. Brecht, Y. Y. Gao, S. Shankar, M. Hatridge, G. Catelani, M. Mirrahimi, L. Frunzio, R. J. Schoelkopf, L. I. Glazman, and M. H. Devoret (2014), “Non-Poissonian Quantum Jumps of a Fluxonium Qubit due to Quasiparticle Excitations,” *Phys. Rev. Lett.* **113** (24), 247001.
- Vool, U., S. Shankar, S. Mundhada, N. Ofek, A. Narla, K. Sliwa, E. Zaly-Geller, Y. Liu, L. Frunzio, R. Schoelkopf, S. Girvin, and M. Devoret (2016), “Continuous Quantum Nondemolition Measurement of the Transverse Component of a Qubit,” *Physical Review Letters* **117** (13), 133601.
- Wal, C. H. v. d., A. C. J. t. Haar, F. K. Wilhelm, R. N. Schouten, C. J. P. M. Harmans, T. P. Orlando, S. Lloyd, and J. E. Mooij (2000), “Quantum Superposition of Macroscopic Persistent-Current States,” *Science* **290** (5492), 773–777.
- Wallraff, A., D. I. Schuster, A. Blais, J. M. Gambetta, J. Schreier, L. Frunzio, M. H. Devoret, S. M. Girvin, and R. J. Schoelkopf (2007), “Sideband Transitions and Two-Tone Spectroscopy of a Superconducting Qubit Strongly Coupled to an On-Chip Cavity,” *Physical Review Letters* **99** (5), 050501.
- Walls, D. F., and G. J. Milburn (2008), *Quantum Optics* (Springer Science & Business Media).
- Wang, C., Y. Y. Gao, P. Reinhold, R. W. Heeres, N. Ofek, K. Chou, C. Axline, M. Reagor, J. Blumoff, K. M. Sliwa, L. Frunzio, S. M. Girvin, L. Jiang, M. Mirrahimi, M. H. Devoret, and R. J. Schoelkopf (2016), “A Schrödinger cat living in two boxes,” *Science* **352** (6289), 1087–1091.
- Weber, J. R., W. F. Koehl, J. B. Varley, A. Janotti, B. B. Buckley, C. G. V. d. Walle, and D. D. Awschalom (2010), “Quantum computing with defects,” *Proceedings of the National Academy of Sciences* **107** (19), 8513–8518.
- Weedbrook, C., S. Pirandola, R. García-Patrón, N. J. Cerf, T. C. Ralph, J. H. Shapiro, and S. Lloyd (2012), “Gaussian quantum information,” *Reviews of Modern Physics* **84** (2), 621–669.
- Wellstood, F. C., C. Urbina, and J. Clarke (1987), “Low frequency noise in dc superconducting quantum interference devices below 1 K,” *Applied Physics Letters* **50** (12), 772–774.
- Wineland, D. J., C. Monroe, W. M. Itano, D. Leibfried, B. E. King, and D. M. Meekhof (1998), “Experimental Issues in Coherent Quantum-State Manipulation of Trapped Atomic Ions,” *Journal of Research of the National Institute of Standards and Technology* **103** (3), 259–328.
- Xu, H. K., C. Song, W. Y. Liu, G. M. Xue, F. F. Su, H. Deng, Y. Tian, D. N. Zheng, S. Han, Y. P. Zhong, H. Wang, Y.-x. Liu, and S. P. Zhao (2016), “Coherent population transfer between uncoupled or weakly coupled states in ladder-type superconducting qutrits,” *Nature Communications* **7**, 11018.

- Xu, X., B. Sun, P. R. Berman, D. G. Steel, A. S. Bracker, D. Gammon, and L. J. Sham (2007), “Coherent Optical Spectroscopy of a Strongly Driven Quantum Dot,” *Science* **317** (5840), 929–932.
- Yan, F., S. Gustavsson, J. Bylander, X. Jin, F. Yoshihara, D. G. Cory, Y. Nakamura, T. P. Orlando, and W. D. Oliver (2013), “Rotating-frame relaxation as a noise spectrum analyser of a superconducting qubit undergoing driven evolution,” *Nature Communications* **4**, 2337.
- Yan, F., S. Gustavsson, A. Kamal, J. Birenbaum, A. P. Sears, D. Hover, T. J. Gudmundsen, D. Rosenberg, G. Samach, S. Weber, J. L. Yoder, T. P. Orlando, J. Clarke, A. J. Kerman, and W. D. Oliver (2016), “The flux qubit revisited to enhance coherence and reproducibility,” *Nature Communications* **7**, 12964.
- Yang, C.-P., S.-I. Chu, and S. Han (2004), “Quantum Information Transfer and Entanglement with SQUID Qubits in Cavity QED: A Dark-State Scheme with Tolerance for Nonuniform Device Parameter,” *Physical Review Letters* **92** (11), 117902.
- Yoshihara, F., T. Fuse, S. Ashhab, K. Kakuyanagi, S. Saito, and K. Semba (2016), “Superconducting qubit-oscillator circuit beyond the ultrastrong-coupling regime,” arXiv:1602.00415 .
- You, J. Q., X. Hu, S. Ashhab, and F. Nori (2007), “Low-decoherence flux qubit,” *Phys. Rev. B* **75** (14), 140515.
- You, J. Q., and F. Nori (2011), “Atomic physics and quantum optics using superconducting circuits,” *Nature* **474** (7353), 589–597.
- Zhu, G., D. G. Ferguson, V. E. Manucharyan, and J. Koch (2013), “Circuit QED with fluxonium qubits: Theory of the dispersive regime,” *Physical Review B* **87** (2), 024510.
- Zimmerman, J. E., and A. H. Silver (1966), “Macroscopic Quantum Interference Effects through Superconducting Point Contacts,” *Physical Review* **141** (1), 367–375.
- Zorin, A. (2016), “Josephson Traveling-Wave Parametric Amplifier with Three-Wave Mixing,” *Physical Review Applied* **6** (3), 034006.
- Zorin, A. B., M. Khabipov, J. Dietel, and R. Dolata (2017), “Traveling-wave parametric amplifier based on three-wave mixing in a Josephson metamaterial,” arXiv:1705.02859 .